

Diss. ETH No. 23653

# BROADBAND MID-INFRARED QUANTUM CASCADE LASERS FOR SPECTROSCOPIC APPLICATIONS IN EXTERNAL CAVITY

A thesis submitted to attain the degree of  
DOCTOR OF SCIENCES of ETH Zurich  
(Dr. sc. ETH Zurich)

presented by  
SABINE SARAH RIEDI  
MSc ETH Physics, ETH Zurich

born on January 15<sup>th</sup>, 1986

citizen of Chur, Switzerland

accepted on the recommendation of  
Prof. Dr. Jérôme Faist, examiner  
Prof. Dr. Karl Unterrainer, co-examiner  
Prof. Dr. Joachim Wagner, co-examiner

2016



# Contents

<b>Contents</b>	<b>i</b>
<b>Abstract</b>	<b>v</b>
<b>Zusammenfassung</b>	<b>vii</b>
<b>1 Introduction</b>	<b>1</b>
1.1 The mid-infrared wavelength range and spectroscopy . . .	1
1.2 Dielectric coatings for mid-IR QCLs . . . . .	12
1.3 Motivation and organization of the work . . . . .	12
<b>2 Quantum Cascade Lasers</b>	<b>15</b>
2.1 Historic overview . . . . .	15
2.2 Fundamentals . . . . .	17
2.2.1 Rate equations . . . . .	18
2.2.2 Broadband active region design . . . . .	20
2.3 Fabrication of devices . . . . .	24
2.3.1 Growth and processing . . . . .	24
2.3.2 Device mounting . . . . .	27
2.4 Optical and electrical characterization . . . . .	27
2.4.1 Light-current-voltage characteristic . . . . .	28
2.4.2 Spectral measurements . . . . .	30

2.5	Loss measurements . . . . .	31
2.5.1	Mirror losses and reflectivities . . . . .	32
2.5.2	Waveguide losses . . . . .	33
<b>3</b>	<b>Dielectric coatings: Materials and Fabrication</b>	<b>35</b>
3.1	Introduction . . . . .	35
3.2	Materials . . . . .	37
3.2.1	$\text{Al}_2\text{O}_3$ . . . . .	38
3.2.2	$\text{YF}_3$ . . . . .	38
3.2.3	Germanium . . . . .	40
3.2.4	Silicon . . . . .	40
3.2.5	Other materials . . . . .	40
3.2.6	Tooling factor . . . . .	42
3.3	Fabrication . . . . .	43
3.3.1	Deposition technique . . . . .	43
3.3.2	Adhesion promoters and surface preparation . . . .	45
<b>4</b>	<b>Dielectric AR and HR coatings in the mid-infrared</b>	<b>49</b>
4.1	Introduction . . . . .	49
4.2	Theory . . . . .	50
4.2.1	High-reflection coatings . . . . .	52
4.2.2	Anti-reflection coatings . . . . .	54
4.2.3	Dispersion compensation with Gires -Tournois - inter-ferometer mirrors . . . . .	55
4.2.4	Graded index - Interface free coatings . . . . .	57
4.3	Measurement setup . . . . .	57
4.3.1	Transmission measurement . . . . .	58
4.3.2	Reflection measurement . . . . .	58
4.4	Results . . . . .	59
4.4.1	High-reflection coatings . . . . .	59
4.4.2	Anti-reflection coatings . . . . .	61
4.4.3	Coatings for mode selection . . . . .	66
4.4.4	Fabry-Pérot cavity . . . . .	67
4.4.5	Dispersion compensation coatings . . . . .	68
<b>5</b>	<b>External Cavity and experimental setup</b>	<b>71</b>



5.1	Experimental setup . . . . .	72
5.1.1	External cavity configuration . . . . .	73
5.1.2	Measurement setup . . . . .	75
5.2	Theory . . . . .	76
5.2.1	Rate equations . . . . .	76
5.2.2	Tuning range . . . . .	78
<b>6</b>	<b>Broadband QCL in the 3 - 4 <math>\mu\text{m}</math> range</b>	<b>83</b>
6.1	Introduction . . . . .	83
6.2	Material systems . . . . .	84
6.3	EC tuning around 3.3 $\mu\text{m}$ wavelength . . . . .	88
6.4	Active region design at 3.7 $\mu\text{m}$ wavelength . . . . .	89
6.5	Heterogeneous active region design from 3 to 4 $\mu\text{m}$ wave- length . . . . .	92
6.6	EC tuning from 3 to 4 $\mu\text{m}$ wavelength . . . . .	93
<b>7</b>	<b>Broadband QCLs in the 5 - 10 <math>\mu\text{m}</math> range</b>	<b>97</b>
7.1	EC tuning around 5.7 $\mu\text{m}$ . . . . .	97
7.2	EC tuning around 8 $\mu\text{m}$ . . . . .	99
7.3	EC tuning of heterogeneous cascade designs with three and five colors . . . . .	101
<b>8</b>	<b>Superluminescence and amplifiers</b>	<b>105</b>
8.1	Introduction . . . . .	105
8.2	Theory . . . . .	106
8.2.1	Fabry-Pérot cavity fringes . . . . .	107
8.2.2	Hakki-Paoli . . . . .	109
8.2.3	Optical power . . . . .	110
8.3	Experimental setup and measurements . . . . .	113
8.3.1	QC-SLED . . . . .	113
8.3.2	Light-Current-Voltage characteristics of a superlumi- nescent QC-SLED . . . . .	114
8.3.3	Subthreshold luminescence spectral measurements .	116
8.3.4	Gain evaluation . . . . .	117
8.3.5	Modulation of the QC-SLED . . . . .	119
8.4	QCL amplifiers . . . . .	119

<b>9 Summary and outlook</b>	<b>121</b>
<b>Literature</b>	<b>123</b>

## Abstract

In recent years, the prevalence of lasers in electronic devices has skyrocketed. Everything from a computer mouse to data communications to spectroscopy applications is based on the ability to coherently control the emission of light. Quantum cascade lasers are unique semiconductor devices based on intersubband transitions that allow for lasing from the mid-infrared to the terahertz regime. This property, termed wavelength agility, can be achieved because the laser emission frequency is determined by a sequence of quantum wells and barriers; vastly different emission energies can be accessed by changing the number, thickness, and order of the semiconductor layers. Additionally, the lasers can be designed with a broadband gain structure. When such lasers are operated in a grating tuned external cavity, the single mode laser output can be tuned over several hundred wavenumbers.

These features of the quantum cascade laser, together with their small size ( $\sim$ mm), make it ideal for spectroscopy in the mid-infrared regime. Between  $\lambda = 3 - 12 \mu\text{m}$  there are two atmospherically transparent regions, termed the first and second atmospheric windows, where many small molecules have characteristic absorption features. Some prominent examples are greenhouse gases including  $\text{CO}_2$ ,  $\text{CO}$ ,  $\text{N}_2\text{O}$ , and  $\text{CH}_4$ . The ability to tune the emission of a quantum cascade laser makes it possible to simultaneously detect different molecules in compound liquids and gases.

Accessing the full gain bandwidth of the quantum cascade laser makes it a versatile source for spectroscopic applications. Applying anti-reflection and high-reflectivity coatings to the laser facets will modify both its electrical and optical behavior, improving its wavelength agility. Anti-reflection coatings with reflectivities  $\leq 1\%$  over bandwidths of several hundred wavenumbers are designed and fabricated, as well as dielectric reflective coatings ranging from partial coatings ( $R = 65\%$ ) to nearly perfect mirrors ( $R = 98\%$ ).

Quantum cascade lasers also have several features that allow the design of very broad gain bandwidth laser structures. These features are discussed and implemented in a new design for the wavelength range spanning  $3 - 4\ \mu\text{m}$ . When combined with the anti- and high-reflection coatings discussed above, such devices in an external cavity featured tuning ranges of over  $500\ \text{cm}^{-1}$  in pulsed mode.

Finally, the superluminescent behavior of quantum cascade lasers is studied. When a quantum cascade laser is prevented from reaching its lasing threshold by high cavity mirror losses, the device emits superluminescent light with a high degree of spatial coherence (due to the device's waveguide geometry), while maintaining low temporal coherence (characteristic of amplified spontaneous emission). Peak powers of  $38\ \mu\text{W}$  at  $10\%$  duty cycle were achieved, which is three orders of magnitude higher than the blackbody radiation of a globar of comparable size, temperature, and spectral range. The combination of these features make quantum cascade superluminescent diodes very attractive for optical coherence tomography and mid-infrared microscopy.

Such devices, fabricated with anti-reflection coatings on both cavity mirrors, can also serve as amplifiers for frequency combs.

## Zusammenfassung

In den letzten Jahren hat die Verbreitung von Lasern in elektronischen Geräten stark zugenommen. Alles von einer Computermouse über Datenkommunikation bis hin zu spektroskopischen Anwendungen basiert auf der Fähigkeit, kohärentes Licht zu erzeugen. Quantenkaskadenlaser sind einzigartige Halbleiterbauelemente, die auf Intersubbandübergängen basieren und den Spektralbereich vom mittleren Infrarot- bis in den Terahertz-Bereich abdecken. Diese Eigenschaft, Wellenlängenagilität genannt, wird dadurch ermöglicht, dass die Laseremissionsfrequenz durch eine Folge von Quantentöpfen und -barrieren bestimmt wird; durch Änderung der Anzahl, Dicke und Anordnung der Halbleiterschichten können sehr unterschiedliche Emissionsenergien erreicht werden. Zusätzlich können die Laser mit einer breitbandigen Verstärkung entworfen und als Verstärkungselement in einer externen Kavität betrieben werden. Dies ermöglicht eine breitbandig abstimmbare, einmodige Emission über mehrere hundert Wellenzahlen.

Diese Merkmale der Quantenkaskadenlaser, zusammen mit der geringen Grösse, machen sie zur idealen Lichtquelle für kompakte Spektroskopiesysteme. Zwischen  $\lambda = 3 - 12 \mu\text{m}$  gibt es zwei atmosphärisch transparente Bereiche, in denen viele kleine Moleküle charakteristische Absorptionslinien aufweisen. Einige prominente Beispiele sind Treibhausgase, einschliesslich  $\text{CO}_2$ ,  $\text{CO}$ ,  $\text{N}_2\text{O}$ , and  $\text{CH}_4$ . Die Fähigkeit, die Emissi-

onswellenlänge der Laser über einen weiten Wellenlängenbereich abstimmen zu können, ermöglicht die gleichzeitige Erkennung und Messung mehrerer Moleküle einer Gas- oder Flüssigkeitsmischung. Auf die volle Verstärkungsbandbreite des Lasers zugreifen zu können, ermöglicht eine vielseitige Anwendung von Quantenkaskadenlasern. Hierzu wird die Laserkavität, und somit das optische und elektrische Verhalten, mittels Spiegel- und Entspiegelungsbeschichtungen verändert. Sowohl Entspiegelungsbeschichtungen, mit Reflektivitäten von weniger als  $R = 1\%$  über eine Bandbreite von mehreren hundert Wellenzahlen, als auch dielektrische Spiegel, mit Reflektivitäten von  $R = 65\% - 98\%$ , wurden hergestellt.

Quantenkaskadenlaser haben einige Eigenschaften, die die Herstellung von Laser mit breitbandigem Verstärkungsbereich ermöglichen. Diese Eigenschaften werden anhand einer Struktur im Wellenlängenbereich von 3 bis 4  $\mu\text{m}$  besprochen. Laser, die auf dieser Struktur basieren, wurden in einer externen Kavität betrieben und konnten im gepulsten Betrieb über einen Bereich von mehr als  $500\text{ cm}^{-1}$  einmodig abgestimmt werden.

Schlussendlich wird auch das superlumin eszente Verhalten von Quantenkaskadenlasern untersucht. Wenn ein Quantenkaskadenlaser mit Hilfe von Entspiegelungsbeschichtungen vom Erreichen der Laserschwelle gehindert wird, emittiert Dieser superlumineszentes Licht, welches einen hohen Grad räumlicher Kohärenz (aufgrund der Geometrie des Wellenleiters), und eine niedrige zeitliche Kohärenz (charakteristisch für verstärkte spontane Emission) zeigt. Optische Leistungen von 38  $\mu\text{W}$  wurden gemessen. Diese Leistung ist drei Größenordnungen höher, als diejenige der Schwarzkörperstrahlung eines thermischen Strahlers von vergleichbarer Grösse, Temperatur und vergleichbarem Spektralbereich. Die Kombination dieser Eigenschaften machen solche Quantenkaskaden-Superlumineszenz-Dioden attraktive Quellen für Kohärenztomographie und Mikroskopie im mittleren Infrarotbereich. Solche Quantenkaskadenlaser mit Entspiegelungsbeschichtungen können auch als Verstärker für Frequenzkämme dienen.

## Chapter 1

# Introduction

### 1.1 The mid-infrared wavelength range and spectroscopy

The mid-infrared (mid-IR) spectral region, and especially the first and second atmospheric windows, at  $3 - 5 \mu\text{m}$  and  $8 - 12 \mu\text{m}$ , respectively, cf. Fig. 1.1 a), are of importance since fundamental ro-vibrational stretching modes of many molecules, including C-H, N-H and O-H, have strong resonances in this region [1, 2]. The absorption strength of light molecules is generally stronger (up to several orders of magnitude) than in the near-IR as is illustrated in Fig. 1.1 b) for the example of nitric oxide. Thus higher sensitivity, up to parts per trillion (ppt  $10^{-12}$ ) [3, 4, 5, 6] can be expected

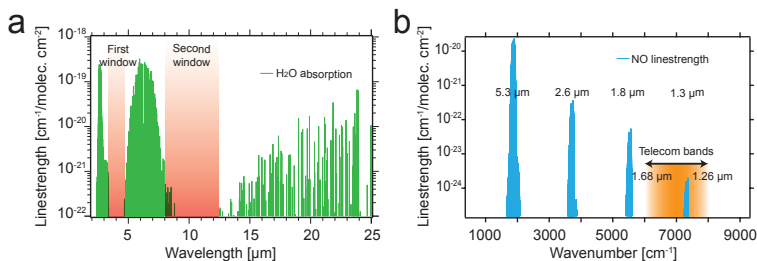


**Figure 1.1:** SOURCE: HITRAN 2008. **a)** Water absorption in the mid-IR wavelength range with the two transmission windows from 3 - 5  $\mu\text{m}$  and 8 - 12  $\mu\text{m}$  wavelength. **b)** Comparison of the line strength of nitric oxide from the near-IR to the mid-IR. The absorption strength of the bands are orders of magnitude stronger in the mid-IR than in the near-IR region, thus allowing to detect lower concentrations.

in the mid-IR, making this region attractive for chemical sensing. This therefore opens up the way for many applications in different fields such as environmental monitoring, medicine, security and explosive detection [7].

There are many different established methods to measure concentrations in the atmosphere and in samples [8] and especially spectroscopic techniques are of great interest for gas and air sensing due to their non-intrusive way of detecting multi-component gases [9]. For example, Fourier transform infrared (FTIR) spectrometers are widely used and well established [10, 11]. However, they are generally bulky and have a limited resolution as well as a slow acquisition time. In addition, the light sources used are generally relatively weak, making sensing of thick or strongly absorbing samples very challenging. And even though small FTIRs exist, for example based on MEMS, they still suffer from a limited resolution [12].

Shown in Fig. 1.2 is the schematic diagram of a laser based spectroscopy setup. A collimated laser beam is passed through a sample cell and the light measured with a detector. From the resulting wavelength dependent absorption profile, a qualitative as well as quantitative composition of the sample can be calculated. A major application in the mid-IR range is gas sensing, using the basic principle of the Tunable Laser Absorption Spectroscopy (TLAS, cf. Fig. 1.2) [13, 14] where a single mode laser is scanned over a rotational-vibrational absorption line of a specific gas molecule [15, 16]. TLAS can equally well be applied to liquid phase probes or even solid samples. Such laser based spectroscopy enables a sensing technique with high sensitivity and specificity, multi-component capability and high resolution [17, 18, 3, 4, 5, 6]. It also requires minimal sample preparation and is versatile as well as reliable and robust, i.e. can endure harsh environmental conditions [3].

These promising features are exploited and investigated for example for medical applications such as disease detection in breath and/or bodily fluids. In some cases patients might not be able to give a blood or urine sample which makes a breath analysis favorable due to the simplicity of the sample collection process. It is known that certain diseases have specific biomarkers that are present in the patient's breath and therefore



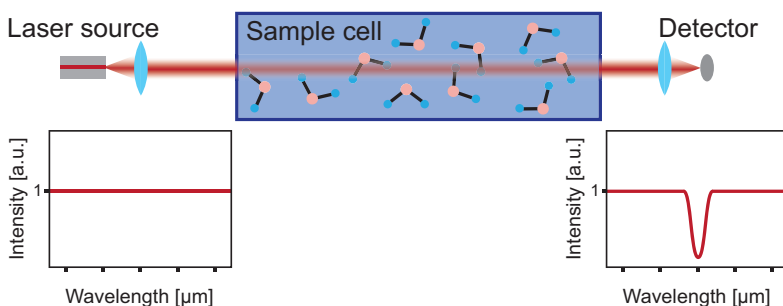


**Figure 1.2:** Schematic view of a tunable laser absorption spectroscopy setup. The incident laser has a known spectrum with known intensities at different wavelengths. The absorption of the sample inside the sample cell can be determined by measuring the laser spectrum after passing the cell. Comparison with databases can determine the mixture of the sample.

can be used to detect asthma, diabetes, lung, liver and dental diseases, some types of cancer and bacterial infections. The respiratory tract is a complex system with an intricate gas exchange through the aveolar-blood capillary membrane as well as mucous membranes and depends on the vapor pressure of the gas. Thus the molecular profile of breath will be a composition of the inspiratory air, volatile molecules that are in the blood and molecules expired through mucous membranes. The bulk matrix of breath is a mixture of nitrogen, oxygen, carbon dioxide, water vapor and inert gases. The remainder of the breath is a mixture of as many as 3000 different volatile organic compounds (VOCs). Thus the detection relies on the accurate sensing of the bulk matrix as well as the specific biomarkers which laser spectroscopy provides. Due to the large number of significant marks for each individual disease it is important to have broadband, tunable laser sources that are able to capture a full frequency range necessary to determine all compounds [19]. Chapter 5 will explain how this is achieved with quantum cascade lasers [20] in external cavities. [21, 22, 23, 24, 25, 26]

While breath analysis in the medical sector is still in its infancy, in the security sector it is a routine test for ethanol detection. The police uses hand held modules to quantitatively determine a person's ethanol level. Since not only alcohol but also drugs can impair a persons judgment the demand for a hand held testing module for hard drugs, such as cocaine

and heroine, increased. It is nearly impossible to detect cocaine in breath but it is possible to detect it in saliva. But for cocaine the number of masking agents is very large, making a simple quantitative test very difficult. However, cocaine has one specific and unique absorption line in the mid-IR. This opens up the possibility for a laser absorption sensing application which has been successfully achieved by Hans *et al.* [27, 28]. Other areas in which laser sensing systems play an important role are remote sensing, chemical sensing, environmental monitoring, free-space communication and many more [29, 30, 31, 32, 33, 34, 19, 35, 36, 37].

An aspect that all of these applications have in common is the necessity to detect multiple absorption lines simultaneously. For very specific applications it might be enough to have a single-wavelength laser source that emits at precisely the absorption wavelength under investigation. However, for both optical communication systems and spectroscopy a continuously tunable single mode laser source is required.

There are several important requirements that laser sources suited for TLAS have to fulfil. As mentioned above, high power is needed to reach high resolutions and thus detect also small quantities of components in a mixture. Another vital requirement is the tunability of the laser source. Most applications mentioned above rely on the detection of a set of several components simultaneously and/or on the resolution of broad background features. To be able to resolve such absorption structures the source has to be tunable over a wide wavelength range in single mode operation.

In the mid-IR range there are mostly three competing semiconductor laser sources that fulfill these requirements, i.e. diode, interband cascade and quantum cascade lasers (DLs, ICLs and QCLs), all three of which are based on a double heterostructure design. The basic idea of this is to clad the photon generating active region between confinement layers that ideally exhibit different refractive indices in order to act as a waveguide. The photon generating structure of the three types of lasers are schematically shown in Fig. 1.3 a). Low-dimensional structures like quantum wells (QWs) and quantum dots (QDs) additionally exploit the quantization effects to provide even higher carrier densities at respective laser levels.

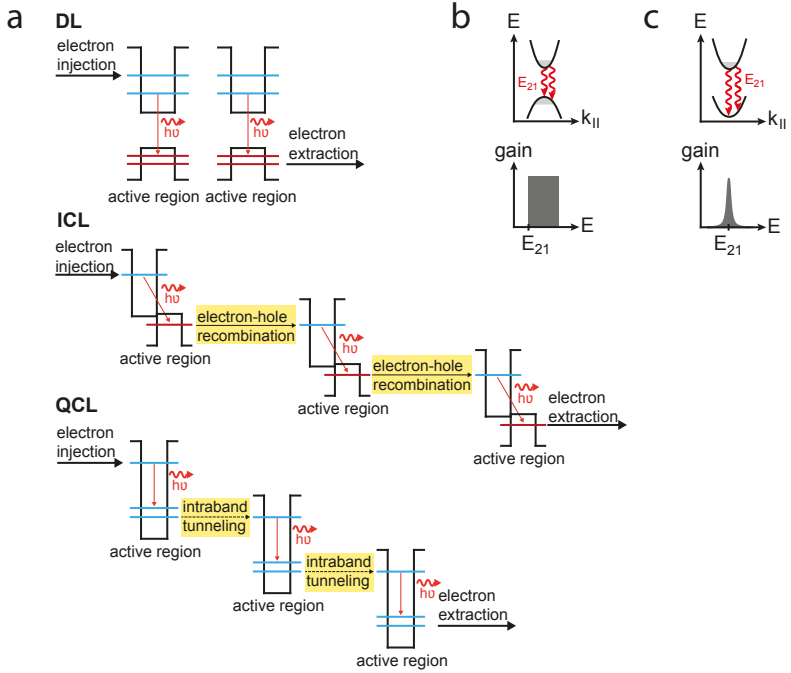


**Figure 1.3:** **a)** The three main semiconductor laser sources are diode lasers (DL), interband cascade lasers (ICL) and quantum cascade lasers (QCL). The schematic working principle is shown for each of the laser types. **b)** Dispersion bands with opposite curvature resulting in a gain with a lower energy boundary for interband transitions (ICL and DL). **c)** Atomic like density of states due to the intersubband transition in QCLs.

Fig. 1.4 (taken from A. Bauer *et al.* [2]) shows the sandwiching due to materials with differing energetic band alignments at the example of a GaSb based DL. The lower part shows the change in refractive index and the resulting confinement of the optical mode. DLs use carrier inversion as their photon generation method [38, 39, 40]. Sufficiently high pumping currents are applied until the quasi Fermi levels of electrons and holes reach the energy separation of the desired emission wavelength. It is possible to use a series of several QWs to increase the modal gain of a device, every electron-hole pair can ever only generate one photon each. This inherently limits the quantum efficiency of the device.

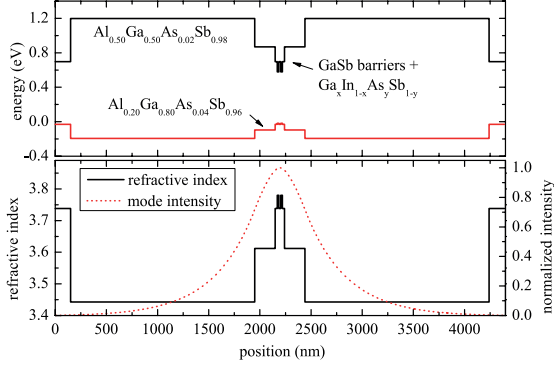


**Figure 1.4:** SOURCE: Bauer *et al.* [2]. Upper part: energy bands in a diode laser based on GaSb material system. Lower part: corresponding refractive index profile (solid) and resulting optical mode distribution (dashed).

However, as QWs are pumped in parallel, only low bias voltages are required for laser operation [41], rendering DLs efficient in converting electrical power into optical power [42]. However, DLs suffer from non-radiative losses due to Auger recombination with increasing wavelengths [43, 44, 45]. Nonetheless, DLs such as bars, broad area single emitters, vertical cavity surface emitting lasers (VCSELs) [46] and vertical external cavity surface emitting lasers (VECSELs) are established sources in the data and telecom wavelength range (800 - 1500 nm). They are used as high power fiber pump lasers for terrestrial and submarine fibers and have output powers of several tens of Watts. Another field of employment are data centers where high data rates and good signal strengths are required. High-power DLs are bar lasers with output powers larger than 100 W.

Interband cascade lasers (ICLs) also present good sources for the short wavelength region due to low threshold current densities and high output power [47]. However, since they are based on less prevalent material systems, i.e. including Sb, the growth is more difficult and the required precision on the atomic level can only be provided by molecular beam epitaxy (MBE) [47] whereas DLs and QCLs both can be grown by metal-organic chemical vapor deposition (MOCVD) providing higher throughput and thus better cost efficiency [48]. An important difference between

interband and intersubband optical transitions lies in their joint density of states. While interband transitions are determined by the distribution of electrons and holes in the conduction and valence band, resulting in a broadening of the spectrum for shorter wavelengths (cf. Fig. 1.3 b)), the intersubband transitions have an atomic-like joint density of states which give rise to a narrow gain linewidth. As can be seen in Fig. 1.3 c) this is due to the same curvature of the initial and final subbands in  $k$ -space (neglecting non-parabolicity). It is this specific shape of the gain that limits interband lasers to homogeneous active region designs. Since there is only a lower limit to the transition energy, all higher energies can be re-absorbed, preventing the combination of several active regions within one device and thus limiting the accessible gain. For intersubband lasers on the other hand, heterostructures are a real possibility since the problem of cross absorption in the active region can be addressed by a careful design of the multicolor stacks. Such structures are mainly used to create broad gain structures as will be discussed in more detail in chapter 2.

Quantum cascade lasers (QCLs) have the unique possibility to tailor the emission frequency [20, 49, 50] and thus are very versatile lasers. In recent years single mode QCLs lasing in pulsed and continuous wave mode close to  $3\text{ }\mu\text{m}$  have been presented [51, 52, 53, 54]. Room temperature output powers as high as 900 mW in pulsed and 500 mW in continuous wave were reported [53, 54]. Due to the unique properties of the QCL including large wavelength tunability covering the two atmospheric windows in the mid-IR range, the remainder of this work will focus on QCLs and only mention other laser sources where it helps as comparison.

Wavelength agility of QCLs can be achieved in several different ways. The most mature technique for semiconductor lasers is the use of distributed feedback (DFB) [57, 55, 58]. A diffraction grating is used to periodically structure the active region and build a one-dimensional interface grating that provides optical feedback for certain wavelengths. In the case of QCLs, the grating is etched into the active region on the interface to the waveguide as can be seen in Fig. 1.5 a). Due to the fact that the refractive index changes with temperature, the DFB grating will change its duty cycle and thus change the selected wavelength feedback. This gives rise to a limited tuning ability (typically  $0.2 - 0.3\%$  tuning of the center

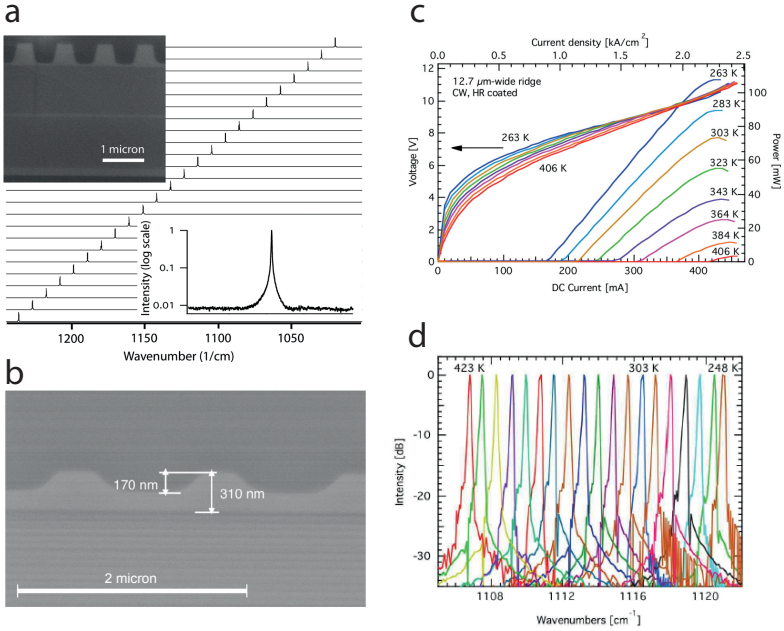


**Figure 1.5:** **a)** SOURCE: Lee *et al.* [55]. DFB array: Spectra of 24 single-mode DFB lasers in the array. Laser frequencies are spaced  $\sim 9.5 \text{ cm}^{-1}$  apart and span a range of  $\sim 220 \text{ cm}^{-1}$ . (Inset, top left) Scanning electron micrograph showing a cross-section of the device, which has been cut along the laser ridge. The grating corrugation can be seen as the rectangular wave near the top of the image, and the two active regions are below, with a thin InGaAs spacer between them. (Inset, bottom right) Spectrum of a representative laser in the array on a log scale, showing sidemode suppression  $\geq 20 \text{ dB}$ . **b)** SOURCE: Wittmann *et al.* [56]. Scanning electron micrograph of a DFB grating on top of an active region after regrowth was performed. **c)** LIV characteristics of a single-mode DFB QCL processed as buried heterostructure with a buried grating. **d)** Temperature tuning of a buried grating device operated above room temperature.

wavelength [59, 9]) of DFB lasers with temperature as shown in Fig. 1.5 d). Increasing this tuning range can be achieved by operating several DFB devices with different wavelength selection in conjunction. The more elegant solution is to process monolithic DFB arrays, either in the edge emitting [60] or surface emitting configuration [61, 62]. Fig. 1.5 a) shows one example of such an etch emitting DFB array. Nevertheless, the large number of output beams can be a major limitation on the optical coupling capability of such a system.

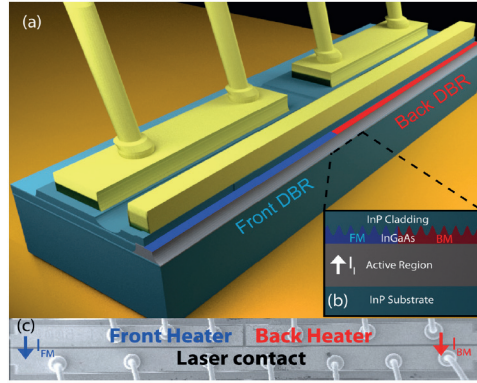


**Figure 1.6:** SOURCE: Bidaux *et al.* [63]. **a)** Schematic view of a cut along the ridge of a device showing the individual heater sections for the front and back DBRs. **b)** Magnified view of the active region and the gratings of the front and back DBRs. **c)** Scanning electron microscopic top view of a processed laser.

One way to overcome this limitation is to include sampled gratings distributed Bragg reflectors (DBRs) inside the ridge and tune the emission frequency using the Vernier effect [64]. This approach has been applied to QCLs [65, 66, 67, 68] and combined into one optical cavity [63]. Fig. 1.6 shows a schematic view of a device with two DBR sections and individual heaters alongside each section to finely tune each laser section individually. The result is a widely tunable, mode-hop free monolithic laser with an output power of more than 100 mW [63].

Another way to spectrally access a broad spectrum is based on frequency combs [69]. Dual comb spectroscopy [70] is based on the heterodyne beating of two frequency combs with a slightly different mode spacing. If the difference of the comb line spacings is chosen properly, a one-to-one mapping between the combs and their radio frequency (RF) domain counterpart can be established [71]. One comb can act as the sample beam and passes through an absorption gas cell whereas the second comb acts as the reference beam. The absorption information in the sample comb is translated into the RF domain. Fig. 1.7 a) and b) show a schematic view of a typical QCL based dual comb spectroscopy setup.

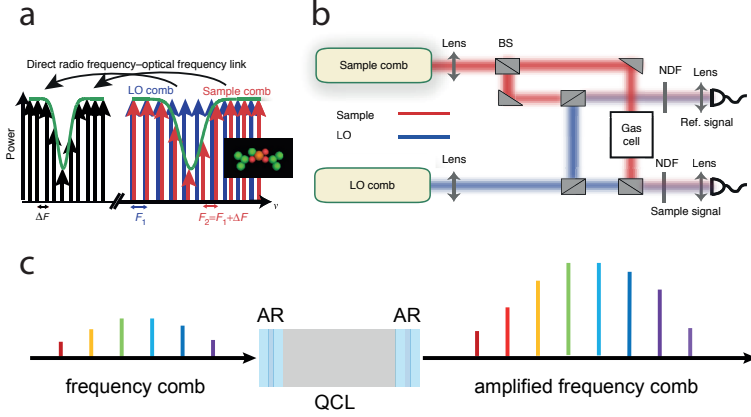


**Figure 1.7:** Frequency combs; dual-comb spectroscopy: **a)** SOURCE: Villares *et al.* [72]; multi-heterodyne beating of two frequency combs with slightly different mode spacings generate a link between the optical and RF domain. The sample comb carries the absorption information into the RF domain. **b)** SOURCE: Villares *et al.* [72]; schematic view of a dual comb spectroscopy setup based on QCL combs. NDF: neutral density filter; BS: 50/50 beam splitter. **c)** Schematic drawing of a QC gain slab with AR coatings on the front and back facet, used as a QCL frequency comb amplifier.

So far, however, the broadest tuning of QCLs in the mid-IR has been achieved with grating tuned external cavity setups [73, 74, 75, 76]. The first external cavity setup was shown by Littman in 1978 for a grazing-incidence pulsed dye laser [77] and soon applied to other types of lasers, especially semiconductor lasers [78, 79, 80]. The Littrow configuration, where the grating is rotated, rather than the mirror in the Littman configuration, has been applied shortly afterwards [81, 82].

The success of this type of broadband tuning for DLs in the visible and near-infrared (NIR), with commercially available tuning ranges of over  $200 \text{ cm}^{-1}$  [83] spurred the development of this technique in the MIR for QCLs. Fig. 1.8 shows the Littrow configuration setup alongside the free-running and EC lasing spectra of the first attempt of applying the EC to QCLs [84]. This led to the exploration of the MIR wavelength range with broadband active region designs and broad tuning ranges [85, 86, 87, 76]. The topic of external cavities will be discussed in more detail in chapter 5.



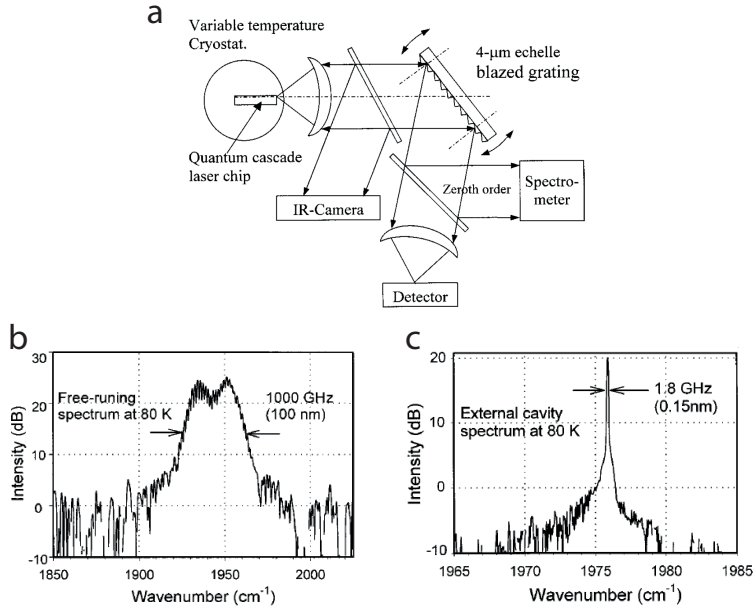


**Figure 1.8:** SOURCE: LUO *et al.* [84]. a) Schematic drawing of a Littrow external cavity setup where the grating is turned. b) Free running and c) external cavity lasing of a QCL centered around 5.1  $\mu\text{m}$  wavelength.

Apart from the need for spectroscopic applications in the MIR, broadband gain devices can have different uses. A double side AR coated device can be used as an amplifier for frequency combs as illustrated in Fig. 1.7 c). Below threshold, QCLs exhibit amplified emission, i.e. amplified spontaneous emission (ASE). This light has very low temporal but high spatial coherence and a high efficiency due to the cascaded active region design. Additionally, a broad internal gain can be designed easily. These properties make QCLs good superluminescent light source with the ability to reduce speckles in laser based imaging applications [88, 89, 90]. Superluminescent sources are the core of optical coherence tomography (OCT) [91], where coherence lengths below 15-30  $\mu\text{m}$  and irradiances above 100  $\mu\text{W}$  are required [92]. Other potential approaches use rapid swept-source mid-infrared lasers [93].

### 1.2 Dielectric coatings for mid-IR QCLs

For most of the aforementioned applications, QCL facets have to be treated with coatings to obtain some of the desired features. Thus for applications such as EC, superluminescence or twin DFB lasers [94], it is desirable to modify the mirror losses, i.e. the mirror reflectivities. For example, for most QCLs the back facet is not directly used for experiments and to prevent the loss of the light, high-reflection (HR) coatings can be applied to the back facets. For QCLs used as frequency combs, this back-facet coating can be adapted to include some wavelength specific dispersive layers to increase the current range in which the laser works in the comb regime (cf. chapter 4.4.5).

Apart from back facet coatings, also front facet coatings are of great importance. Operating a QCL in an EC setup, the laser cavity is constituted by the laser back facet and the grating. Applying a front facet anti-reflection coating removes unwanted reflections and thus increases the wavelength feedback by the grating. This will be discussed in more detail in chapter 5. For such anti-reflection (AR) coatings a set of dielectric materials was selected and used in single- and multi-layer coatings to either minimize the reflectivities over a required wavelength range or to change the facet reflectivity to a specific value, thus creating a partial HR or AR coating. Results for HR and AR coatings are shown in chapter 4.

### 1.3 Motivation and organization of the work

This thesis describes the work that has been conducted by the author at the ETH Zurich under the supervision of Prof. Jérôme Faist on broadband quantum cascade lasers in external cavity for spectroscopic applications. This first introductory chapter shall give an overview on the mid-infrared wavelength range and the spectroscopic applications in that area. It will also provide a short historical overview on what has been done in that field and where this work stands in comparison.

The second chapter will give a basic introduction into the working principle of quantum cascade lasers, the active region design, gain and loss considerations as well as basic characterization techniques.

In the third chapter the fabrication of dielectric high- and anti-reflection coatings will be discussed alongside the optical materials that were used for coatings in this work. Different material qualities and behaviors will be mentioned and the selection criteria highlighted that led to a set of materials used in this thesis. In addition, the calibration process and measurement setup will be described.

The fourth chapter will then describe the theory of thin films acting as coatings and outline the simulation tool to find the optimal coating as well as actual coatings that have been realized and tested. It shows how accurate coatings can be tailored to certain needs and where the challenges lie.

Chapter five gives a detailed overview on QCLs operated in external cavity, the main setup used in this work, including the components and the improvements made on it. It shows the strength and weaknesses of such a setup.

In chapter six, a detailed view of the design of an active region centered around  $3.8 \mu\text{m}$  is given. The design is based on the short wavelength structure presented by Bismuto *et al.* [51].

Chapter seven describes the long wavelength range from  $5 - 10 \mu\text{m}$  where mostly tuning results on lasers designed by Andreas Hugi, Alfredo Bismuto and Stéphane Blaser, are shown.

Chapter eight finally shows an alternative use for QCLs, specifically as superluminescent light sources. The low temporal coherence and high brilliance of QCL superluminescent light sources are highlighted in this chapter.



## Chapter 2

---

# Quantum Cascade Lasers

This chapter will give a short overview on quantum cascade lasers, their physical characteristics and some design considerations. Active region designs for different wavelengths will be discussed in the corresponding chapters 6 and 7. For a more detailed description the reader is referred to [95]. The objective of this chapter is to cover the characteristics that are important for this work, namely broadband gain structures for applications in external cavity and as superluminescent diodes. Of course, broadband active regions are also of strong interest for frequency combs which will not be discussed here. But the interested reader is referred to [96].

### 2.1 Historic overview

QCLs are unipolar semiconductor lasers based on the quantum mechanical mechanisms of tunneling and quantum confinement [49]. The optical transition takes place within the conduction band and therefore only involves electrons. In 1970, Esaki and Tsu [97] proposed a superlattice structure to create minibands and minigaps, enabling Bloch oscillations. Coupled quantum wells (QWs) induce a splitting of the energy levels (Fig. 2.1 a) and b)). Thus a superlattice, formed by many coupled QWs, Fig. 2.1 c), introduces a continuum of allowed energy states, forming so called minibands and corresponding minigaps as depicted in Fig. 2.1 d), which shows the computed minibands and -gaps for a superlattice with 100 Å wide InGaAs wells and 30 Å wide AlInAs barriers. Fig. 2.1 e) shows the

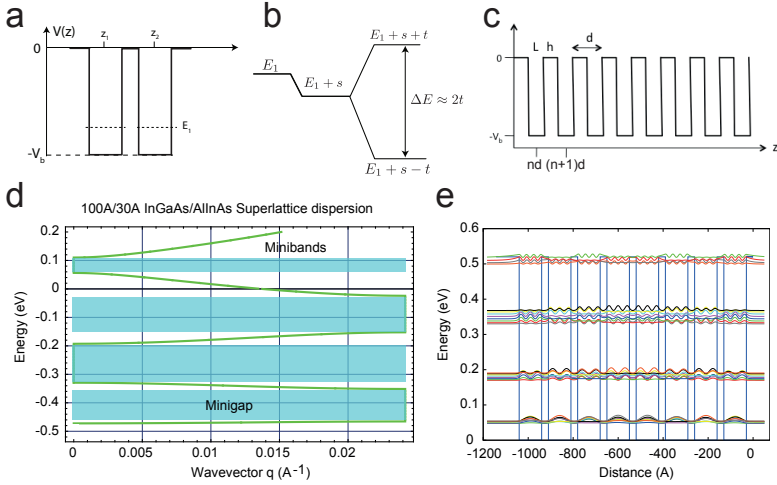


**Figure 2.1:** SOURCE: Faist [95]. **a)** Coupled quantum well and **b)** corresponding energy splitting. **c)** Symbolized superlattice structure. **d)** Computed minibands and -gaps for a superlattice with 100 Å wide InGaAs wells and 30 Å wide AlInAs barriers. **e)** Moduli square of the electron states for the same structure as in d).

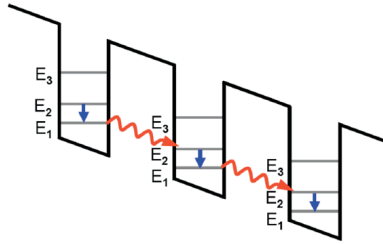


**Figure 2.2:** SOURCE: Kazarinov and Suris [50]. Intersubband laser structure as proposed by Kazarinov and Suris.

corresponding computed moduli square of the electron states. Shortly after Esaki and Tsu [97], Kazarinov and Suris suggested to use high electric fields and photon-assisted electron tunneling in the conduction band for light-amplification [50]. They proposed a structure, shown in Fig. 2.2, which did not lase but spurred the development of superlattice semiconductor lasers which finally lead to the first demonstration of a QCL in 1994 by Faist *et al.* [49]. However, the development of the QCL could not

have happened without the emergence of molecular beam epitaxy in the early 1970s [98, 99].

After the first demonstration of a QCL by Faist *et al.* in 1994 [49] the field developed in many directions such as continuous wave (cw) operation in the MIR at room temperature (RT) [100] or exploration of short wavelength devices [51] and long wavelengths, i.e. the THz region [101]. Output powers of several Watts and wallplug efficiencies above 25 % have been reported [102, 103] as well as devices with dissipation below 250 mW [104]. Distributed feedback lasers [57, 55, 56] as well as broadband lasers for broad tuning in external cavity [105, 76] have been developed. Frequency combs in the MIR as well as THz region have been demonstrated [106, 107] and used for dual-comb spectroscopy [72]. To optimize the current range in which QCLs can be operated as frequency combs, dispersion engineering has to be included in the active region design process. Another approach is to include wavelength dependent dispersive coatings, as will be discussed in section 4.2 of chapter 4.

## 2.2 Fundamentals

Quantum cascade lasers are unipolar semiconductor lasers based on the quantum mechanical mechanisms of tunneling and quantum confinement [49]. The optical transition occurs between quantum confined states inside the conduction band of a semiconductor heterostructure. While the original proposal was based on a superlattice structure, the modern QCL has an active region which consists of a periodic sequence of unit cells. These unit cells consist of a gain region and an injection region as shown schematically in Fig. 2.3. The gain- or active-region part of the unit cell creates and maintains the population inversion through an approximate three level system, or continuum of states. The injection- or relaxation-region extracts the electrons as efficiently as possible from the lower laser state and funnels them towards the next gain region to be injected into the next period. The doping of the structure is usually positioned in the injector region to maintain a high electron count.

The unit cell as shown in Fig. 2.3 a) is then cascaded, with typically  $N_p = 20 - 50$  repetitions. This allows for every electron to emit up to that

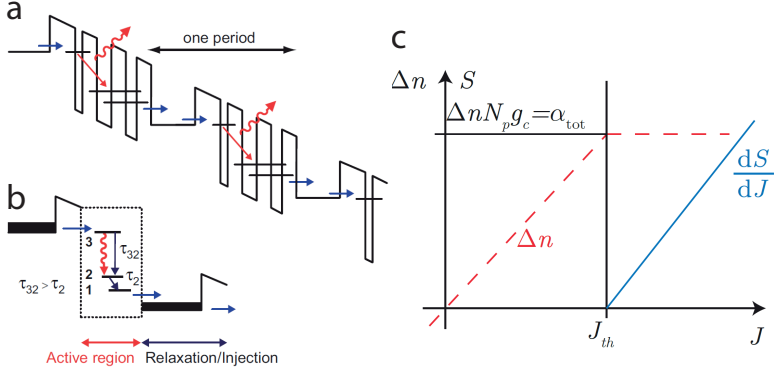


**Figure 2.3:** **a)** SOURCE: Faist [95]. Periodic structure of a QCL. The red, straight arrow indicates the optical transition and the red undulated arrow the emitted photon of this transition. **b)** SOURCE: Faist [95]. Illustration of the division of one period into the injector and the active region. The active region shows a three level structure with the upper laser level 3 and the lower level 2.  $\tau$  indicate the lifetimes of the two laser levels and the transition. **c)** SOURCE: Hugi [96]. Schematic illustration of the behavior of the population inversion as a function of the injection current density  $J$  and gain clamping above threshold.

number of photons. In such a structure, lower operating currents come at the cost of larger operating voltages. This separation of the original superlattice proposal into unit cells with two separate parts made the laser electrically stable.

### 2.2.1 Rate equations

Some important design parameters of QCLs can be highlighted by considering a simplified model where the gain region consists of three states as schematically shown in Fig. 2.3 b). The rate equations for a single stack then are [95]

$$\frac{dn_3}{dt} = \frac{J}{e} - \frac{n_3}{\tau_3} - S g_c (n_3 - n_2) \quad (2.1)$$

$$\frac{dn_2}{dt} = \frac{n_3}{\tau_{32}} - \frac{n_2 - n_2^{\text{therm}}}{\tau_2} + S g_c (n_3 - n_2) \quad (2.2)$$

$$\frac{dS}{dt} = \frac{c}{n_{\text{refr}}} \left( [N_p g_c (n_3 - n_2) - \alpha_{\text{tot}}] S + \beta \frac{n_3}{\tau_{\text{sp}}} \right) \quad (2.3)$$



where  $S$  is the photon flux per unit active region width ( $\text{cm}^{-1}\text{s}^{-1}$ ),  $n_i$  are the sheet densities of level  $i$  per period ( $\text{cm}^{-2}$ ),  $\tau_i$  are the total lifetimes of the states,  $n_2^{\text{therm}}$  is the thermal population of level 2,  $\tau_{32}$  is the nonradiative relaxation time from the upper to the lower laser level and  $\tau_{\text{sp}}$  is the spontaneous emission lifetime.  $\beta$  is the fraction of spontaneous light emitted into the lasing mode,  $J$  is the injection current density,  $\alpha_{\text{tot}}$  are the total chip losses, consisting of mirror losses and waveguide losses,  $n_{\text{refr}}$  is the refractive index of the mode, and  $c$  and  $e$  are the speed of light and elementary charge, respectively. In this description, the gain cross section

$$g_c = \frac{\Gamma}{N_p} \frac{4\pi e^2}{\varepsilon_0 n_{\text{refr}} \lambda} \frac{z_{32}^2}{2\gamma_{32} L_p} \quad (2.4)$$

is defined per period since the rate equations 2.3 are formulated to describe only one period of the active region.  $\Gamma$  is the modal overlap of the lasing mode with the active region,  $N_p$  the number of periods,  $L_p$  the length of one period,  $\lambda$  the wavelength,  $\varepsilon_0$  the vacuum permittivity and  $n_{\text{refr}}$  the refractive index of the active region.  $z_{32}$  and  $\gamma_{32}$  are the dipole matrix element and the transition broadening, respectively.

The gain cross section as a function of the wavelength can be written using a line shape function  $L_G$ :

$$g_c(\lambda) = \frac{\Gamma}{N_p} \frac{4\pi e^2}{\varepsilon_0 n_{\text{refr}} \lambda} \frac{z_{32}^2}{2\gamma_{32} L_p} L_G(\lambda_{\text{peak}} - \lambda). \quad (2.5)$$

The total modal gain of the structure at wavelength  $\lambda$  is then given by

$$G_M(\lambda) = N_p g_c(\lambda) \Delta n \quad (2.6)$$

with the population inversion

$$\Delta n = n_3 - n_2 = \frac{J\tau_3}{e} \left(1 - \frac{\tau_2}{\tau_{32}}\right) - n_2^{\text{therm}} = \frac{J\tau_{\text{eff}}}{e} - n_2^{\text{therm}}. \quad (2.7)$$

The effective lifetime  $\tau_{\text{eff}} = \tau_3(1 - \tau_2/\tau_{32})$  relates the population inversion to the electrical pumping through the upper state lifetime:  $J\tau_3/e$ . At the threshold condition of a QCL, the modal gain  $G_M$  compensates and overcomes the total device losses  $\alpha_{\text{tot}}$  and the threshold current density can thus be written as

$$J_{\text{th}} = e \frac{\alpha_{\text{tot}}/g_c + n_2^{\text{therm}}}{\tau_{\text{eff}}} \quad (2.8)$$

or with the explicitly written gain cross section

$$J_{\text{th}} = \frac{1}{\tau_{\text{eff}}} \left[ \frac{\epsilon_0 n_{\text{refr}} L_p \lambda^2 \gamma_{32}}{4\pi e \Gamma z_{32}^2} \alpha_{\text{tot}} + e n_2^{\text{therm}} \right]. \quad (2.9)$$

Fig. 2.3 c) shows the gain clamping above threshold and the corresponding linear increase of the photon flux.

Another important characteristic of the QCL is the slope efficiency for the whole active region, which can be written as

$$\frac{dP}{dI} = N_p h \nu \alpha_{m,1} \frac{dS}{dJ} = \frac{N_p h \nu}{e} \frac{\alpha_{m,1}}{\alpha_{\text{tot}}} \frac{\tau_{\text{eff}}}{\tau_{\text{eff}} + \tau_2} \quad (2.10)$$

with  $\nu$  the emission frequency and  $\alpha_{m,1}$  the front facet mirror losses. The mirror losses are a function of the front and back facet reflectivities  $R_1$  and  $R_2$  and the length of the final device  $l$  and are given by

$$\alpha_m = \frac{1}{2l} \ln \left( \frac{1}{R_1 R_2} \right). \quad (2.11)$$

### 2.2.2 Broadband active region design

Since broadband laser sources are central to spectroscopic applications, broadband gain engineering is a crucial element to achieve the required tuning results. For QCLs, the operation characteristics and the gain can be maximized by engineering the lifetime and oscillator strength. Broadband gain active regions can be achieved with two compatible design approaches. The straightforward approach is an intrinsically broadband gain structure. Additionally, cascading dissimilar active region stacks further broadens the overall modal gain.

To maintain low threshold current densities and high slope efficiencies in such structures, equations 2.9 and 2.10 show that the following criteria have to be met:

- A long effective lifetime  $\tau_{\text{eff}} = \tau_3(1 - \tau_2/\tau_{32})$ ,
- a long upper state lifetime  $\tau_3$ ,
- low waveguide losses  $\alpha_w$ .

These design criteria can be implemented in a multitude of active region designs that have been demonstrated over the years. For the MIR wavelength range, however, only a small number of designs have established

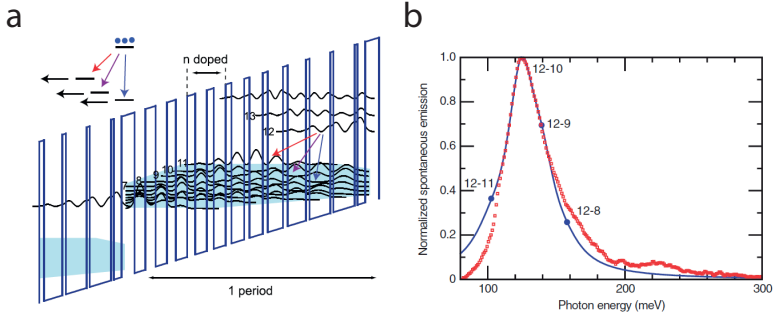


**Figure 2.4:** SOURCE: Hugi *et al.* [73]. **a)** Typical bound-to-continuum active region design with a center frequency of  $9.75 \mu\text{m}$  under an electric field of  $35 \text{ kV/cm}^{-1}$ . **b)** Measured luminescence (solid line) and sum of the computed oscillator strengths (dashed line) of the transitions from the upper laser state (level 12) into the levels 8 - 11.

themselves. Namely, the bound-to-continuum design [108] and the two-phonon resonance design [109] have improved the performance of QCLs, especially regarding high output powers, compared with earlier designs [110]. For QCLs around  $4.3 \mu\text{m}$  [111, 112, 113] as well as in the  $7 - 10 \mu\text{m}$  wavelength range [114, 115], designs based on the two-phonon resonance are still popular and widely used. QCLs based on the bound-to-continuum design show broadband gain as well as good performance and have been successfully applied for broadband tuning in external cavity setups [85, 73, 76].

### Bound-to-continuum active region design

One difficulty in designing QCLs is the lack of a natural population inversion due to the intersubband nature of the optical transition. That implies that lifetimes have to be specifically engineered to create a population inversion. Superlattices feature a large oscillator strength as well as a large ratio of the upper to lower state lifetimes at the minigap edge. However, these lifetimes depend on the existence of minibands and minigaps to prevent the escape of the electrons via tunneling into the next well. Under strong electric fields, as are used in QCL operation, the minibands and minigaps break up into localized states, destroying the feature maintaining the lifetimes. A first approach was to homogeneously dope the su-

perlattice active region to screen the field. However, this led to a broader transition linewidth and additional losses due to ionized carriers, severely limiting operation at room temperature. One way to overcome this problem was presented by Tredicucci *et al.* [116] and consists in a chirped superlattice. The widths of the quantum wells and barriers are gradually changed to keep the energy of the miniband edges constant under applied electric field and thus compensate it.

A typical conduction band diagram of a bound-to-continuum design is shown in Fig. 2.4 a) as presented by Hugi *et al.* [73]. The optical transition occurs between the single localized upper laser state (12) and the set of delocalized lower laser levels (8-11) forming a quasi-miniband. This miniband is created by gradually changing the thicknesses of the quantum wells and barriers, a so called chirped superlattice as can be observed in Fig. 2.4 a). Since the lower laser state is not a localized state but a quasi-continuum, the intrinsic gain shows a broad gain bandwidth. Fig. 2.4 b) shows the simulation and measurement of the luminescence corresponding to the design shown in Fig. 2.4 a). The lineshape of the simulation is obtained by summing up the oscillator strengths of the various transitions under the assumption of Lorentzian broadening. The simulation in Fig. 2.4 b) shows a smooth lineshape which illustrates the significant broadening of the individual transitions. The states are individually indistinguishable and form a continuum, giving its name to the structure.

Even though equation 2.9 shows that the threshold current density  $J_{\text{th}}$  is linearly proportional to the transition linewidth  $\gamma_{32}$ , i.e. suffers under the broadening in the bound-to-continuum design, devices based on such a design still show similarly low thresholds as devices based on two-phonon resonance designs [117]. This is due to the larger dipole matrix elements  $z_{32}$  in bound-to-continuum structures, which can compensate for the broader transitions. Additionally, the lifetime of the lower laser level is small as the electron emits a LO phonon due to a momentum exchange with the lattice. This phonon extraction is very efficient and maintains the necessary population inversion.

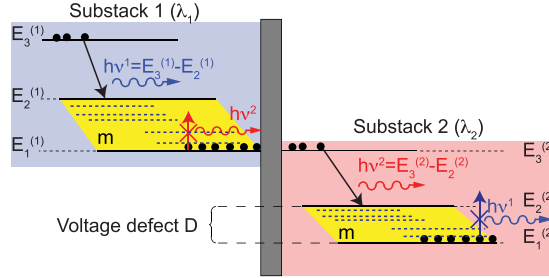


**Figure 2.5:** SOURCE: Hugi *et al.* [96]. Schematic of two active regions, simplified as three level transitions, at different wavelengths. The transparency on both sides of the center frequency allows to build heterogeneous active regions by cascading dissimilar gain regions. The emitted photons from one stack can't be reabsorbed by the other stack due to the energy mismatch of the miniband voltage defects.

### Heterogeneous cascade design

Since even intrinsically broadband gain structures are limited, the idea of cascading dissimilar active regions was presented in 2001 by Gmachl *et al.* [118, 119]. The atomic-like joint density of states of the QCL's intersubband transition peaks around a center frequency  $E_{21}$  and is transparent on both sides of the transition energy, as opposed to IBLs which are transparent only on the long wavelength side and highly absorbing on the short wavelength side. This feature reduces the risk of cross absorption between the different stacks. Additionally, the unipolar nature of the laser and the following cascading principle make QCLs especially appropriate for heterogeneous active region designs. Fig. 2.5 illustrates these advantages on the schematic conduction band diagram of two gain regions at two different wavelengths  $\lambda_1$  and  $\lambda_2$ . The transparency on both sides of the transition energy and careful engineering prohibits cross absorption between the stacks due to a lack of available states.

To the overlap factor  $\Gamma$ , the stacks with different colors are not stacked in sequence but the shortest wavelength stack is sandwiched between increasingly longer wavelength stacks, as illustrated in Fig. 2.6 b). Fig. 2.6 a) shows an example presented by Hugi *et al.* [105] with a heterogeneous design based on five different gain regions centered around 7.3, 8.5, 9.4, 10.4 and 11.5  $\mu\text{m}$  wavelength. The solid line shows the total modal gain

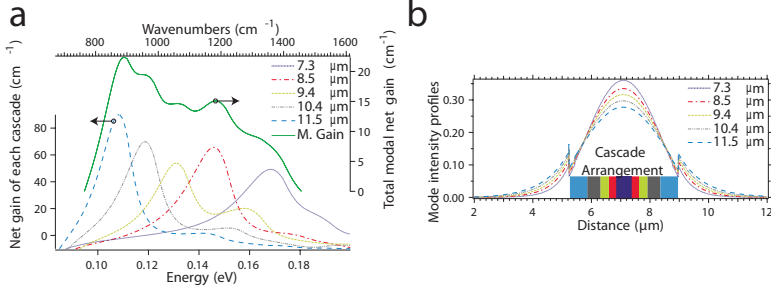


**Figure 2.6:** SOURCE: Hugi *et al.* [105]. Heterogeneous active region design. **a)** Gain simulation of five individual gain regions centered around 7.3, 8.5, 9.4, 10.4 and 11.5 μm (dashed lines) and the total modal gain for the combined active region (bold line). **b)** Symmetrically cascaded arrangement of the five active region stacks.

of the combined active regions with a FWHM of  $\geq 400 \text{ cm}^{-1}$ .

The heterogeneous active region design can suffer from a reduction in the overlap factor  $\Gamma$  as well as from the inhomogeneous total modal gain shape. The gain shape can mainly influence the behavior of the device in external cavity, as discussed in chapter 5.

### 2.3 Fabrication of devices

This section gives an overview on the principles of the growth and processing steps as well as the mounting techniques of buried-heterostructure QCLs to achieve high-performance operation. As mentioned previously, the active region design plays an important role in the device performance. Nonetheless, ever since Beck *et al.* demonstrated the first room temperature mid-IR QCL [120] it has been apparent that the device operation is also strongly influenced by the thermal properties and optical losses introduced by the fabrication process.

#### 2.3.1 Growth and processing

The QCLs presented in this work have been grown by two epitaxial methods, i.e. molecular beam epitaxy (MBE, [121]) and metal organic vapor phase epitaxy (MOVPE). If not mentioned otherwise, the growth and processing of the samples have been done in the shared cleanroom facility

FIRST Center for Micro- and Nanotechnology of the Swiss Federal Institute of Technology (ETH) in Zurich, located on the campus Honggerberg. The growth of the active regions was carried out by Dr. Mattias Beck on a solid-state MBE (V80H, VG Semicon) and the MOVPE growth was done by Dr. Emilio Gini from the cleanroom facility at ETH (FIRST).

The first mid-IR QCLs [49] were processed using the traditional ridge process and claddings made of the ternary material system InGaAs/-InAlAs. InAlAs, however, is a poor thermal conductor and consequently these first QCLs suffered from low thermal conductance and high optical losses. This limited their use for high-power and/or continuous-wave operation. In 2000 and 2002 Beck *et al.* demonstrated room-temperature and continuous wave operation of QCLs devices processed as buried-heterostructures [120, 100]. The buried-heterostructure incorporates a waveguide with a large optical cavity design and a thick confinement layer to minimize the penetration of the optical mode into the cladding layers [122]. This process was a great success but had the disadvantage of being more complicated than the ridge process. Bismuto *et al.* greatly optimized this process, the so called inverted buried-heterostructure design [123]. The steps of this process are described here and illustrated in Fig. 2.7 **a-m**

- a** The active region is grown by MBE on a 2-inch wafer of low n-doped InP ( $1 - 3 \times 10^{17} \text{ cm}^{-3}$ ).
- b** A SiO<sub>2</sub> layer ( $\approx 300 \text{ nm}$ ), deposited by plasma enhanced chemical vapor deposition (PECVD), acts as a hard mask layer for the wet etching (f). A thin layer of photoresist is spun onto the SiO<sub>2</sub> layer.
- c** The waveguide patterning in the resist is defined by UV photolithography.
- d** Using Ar/CHF<sub>3</sub> chemistry, the pattern is transferred to the SiO<sub>2</sub> layer by reactive ion etching (RIE).
- e** The resist layer is stripped away and in order to remove residual polymers, the sample is subjected to an O<sub>2</sub> plasma process and subsequent acetone bath.
- f** The active region is etched using an isotropic HBr:HNO<sub>3</sub>:H<sub>2</sub>O solution.

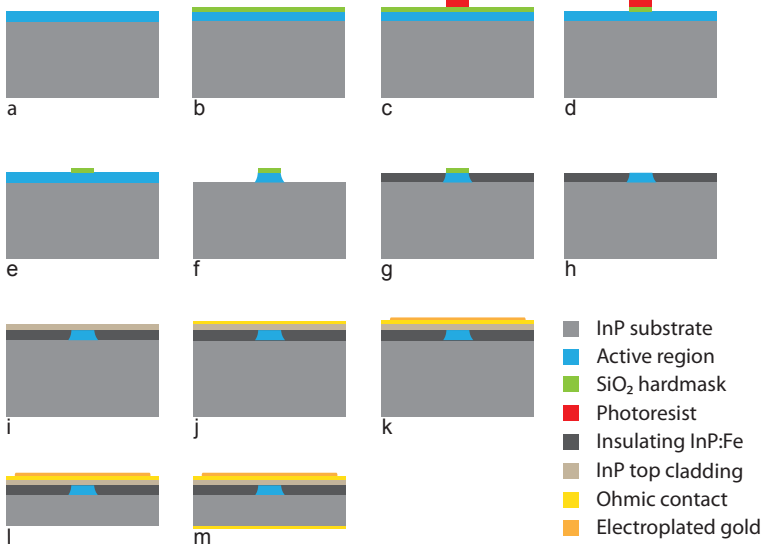


**Figure 2.7:** Processing steps for a buried-heterostructure.

- g** The lateral planarization regrowth with insulating iron doped InP (InP:Fe) is done by MOVPE. The SiO<sub>2</sub> patterning also acts as a mask for the selective regrowth.
- h** The SiO<sub>2</sub> hard mask is removed by hydrofluoric acid (HF).
- i** A n-doped InP top cladding layer is grown by MOVPE over the entire structure.
- j** The Ti/Pt/Au top ohmic contact (5 nm/ 40 nm/ 150 nm) is deposited by e-beam evaporation (MEB550SL, Plassys) over the whole surface.
- k** Contact pads are defined by photolithography and ~ 3 μm of electroplated gold is deposited in the openings above the waveguides.
- l** The substrate is thinned down to ~ 180 μm by mechanical polishing in order to reduce thermal resistance.
- m** The back ohmic contacts are a layer sequence of Ge/Au/Ni/Au (18 nm/ 48 nm/ 10 nm/ 150 nm) deposited by e-beam evaporation.



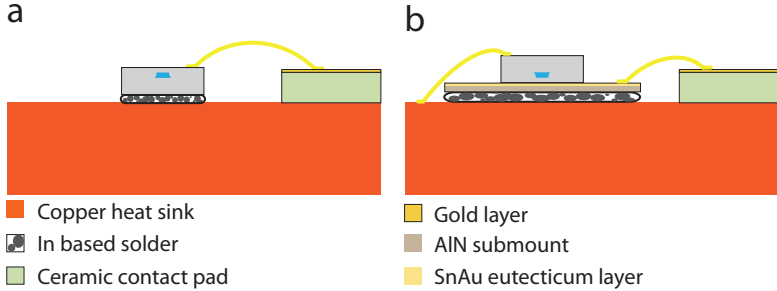


**Figure 2.8:** Mounting and wire bonding of individually cleaved lasers. **a)** Epi-up mounting: the device is soldered onto the oxygen-free copper heat sink with Indium paste. **b)** The device is soldered epi-down onto a Sn/Au coated AlN submount which is then soldered onto the heat sink with In paste.

In general, the structures were grown by MBE on two inch InP wafers and processed in quarters.

### 2.3.2 Device mounting

After the process is finished, the material is cleaved into individual devices of 3 - 6 mm length and by default mounted epi-structure up onto copper mounts of different shapes depending on the intended use of the device. The devices are soldered onto the copper with Indium paste. The Indium paste had to be kept as thin as possible to minimize the fillet height. To further improve the thermal behavior of the devices and therefore increase their performance, e.g. achieve continuous wave operation or high output powers, devices can be mounted epi-side down onto AlN submounts covered with a thin layer ( $\sim 5 \mu\text{m}$ ) of a Sn/Au alloy. The AlN submount is then soldered onto a copper mount with Indium paste, cf. Fig. 2.8.

## 2.4 Optical and electrical characterization

Due to the epitaxial growth and fabrication of QCLs, it is difficult to characterize every individual processing step. The epitaxial layers are characterized by the standard techniques such as high-resolution X-ray diffraction (HRXRD), tunneling electron microscopy (TEM) and scanning electron microscopy (SEM). Light microscopy is used for optical inspection of

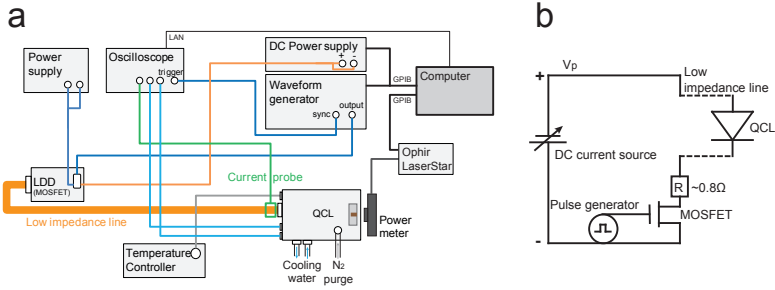


**Figure 2.9:** LIV characterization setup. **a)** Schematic view of the setup for pulsed operation using a power MOSFET. **b)** Electrical circuit of the pulsed operation setup.

different processing steps. Nevertheless, the devices are not fully characterized until they are individually mounted on heat sinks. Thus, there is a great need for very careful characterization of the electrical and optical properties of the final device. This section will give a short overview on the standard characterization techniques used in this work. For a more detailed discussion, the reader is referred to [95].

### 2.4.1 Light-current-voltage characteristic

The most basic and most important, characterization is the measurement of the light-voltage-current, or short LIV, curve of a QCL. First measurements are generally conducted at a low response duty cycle of a few percent with short electrical pulses (100 - 200 ns) to keep the self heating at a minimum. These measurements are repeated at different temperatures to deduce the thermal behavior of the device. Fig. 2.9 shows an overview on the characterization setup (a) and the corresponding electric circuit (b). The optical power was measured with a calibrated thermopile detector power meter (Ophir Laser Measurement Group, model 3A-SH-ROHS), which was positioned directly in front of the laser, as can be seen from the schematic overview in Fig. 2.9 a). In a circuit as shown in Fig. 2.9, the DC current (DC power supply, Agilent E3645A) is switched by a MOSFET (LDD 100, Alpes Lasers SA) with the modulation given by a function generator (80 MHz function generator, Agilent 33250A). These current pulses are fed onto the QCL via a low impedance line. The average current is

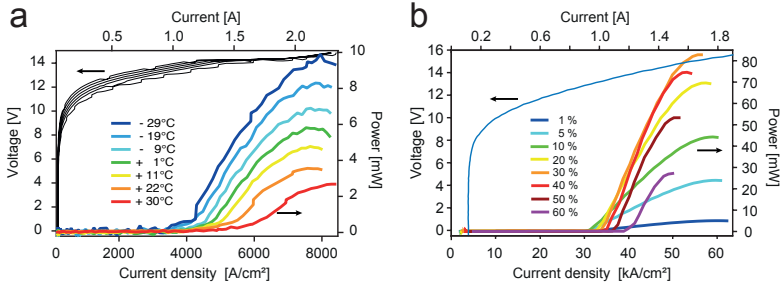


**Figure 2.10:** EV1790. **a)** Typical LIV characterization of a QCL at different temperatures below and above room temperature. For increasing temperature, the threshold current density increases while the output power decreases. The device was run in pulsed operation mode at 1 % duty cycle (100 ns pulse length, 100 kHz repetition rate). **b)** LIV characteristics with varying duty cycles from 1 % up to 60 %. Up to 30 % duty cycle, the output power increases and then decreases with increasing duty cycle, thus no cw operation can be expected of this device.

then measured using a current probe. The bias voltage can be measured as the voltage drop over the laser, that is, the potential difference between the two electrodes of the QCL are measured using a high impedance, DC coupled voltage probe.

Fig. 2.10 a) shows a typical characterization of a QCL (EV1790,  $3.7 \mu\text{m}$  design) at different temperatures. The device was operated in pulsed mode with pulse lengths of 100 ns and a repetition rate of 100 kHz, corresponding to a duty cycle of 1 %. The current-voltage (IV) characteristics show the initial increase of the applied bias voltage without any current flowing through the quantum well structure of the active region. At a voltage of  $\sim 10$  V, the first electrons pass through the structure and at around 13 V the structure is fully aligned and the QCL starts lasing. As expected, with increasing temperature, the threshold current density increases, while the output power decreases. The curves show nicely that the threshold increases while the rollover current stays approximately constant, reducing the dynamic range,  $(J_{\text{max}} - J_{\text{th}})/J_{\text{max}}$ , of the QCL.

Fig. 2.10 b) shows LIV curves with varying duty cycles. The curve at 1 % (100 ns, 100 kHz) shows an output power of 5 mW and increasing the duty cycle in steps to 5 % (100 ns, 500 kHz) and 10 % (100 ns, 1 MHz), the power scales linearly with the increase in duty cycle. Going to 20 % duty cycle (200 ns, 1 MHz), the power shows a sublinear behavior, showing the

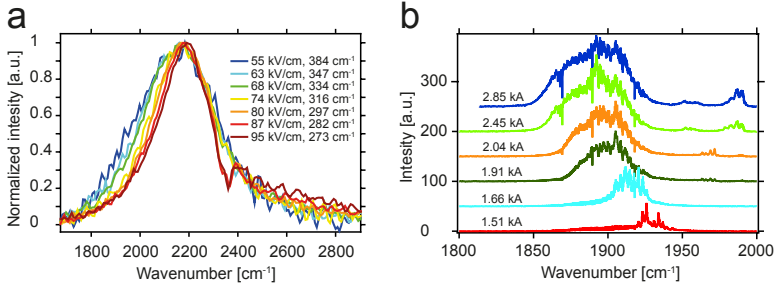


**Figure 2.11:** **a)** Normalized luminescence spectra at 293 K at different applied fields. The curves narrow with increasing field. **b)** Laser spectra at currents from threshold to roll-over. The spectra broaden with increasing current (offset introduced per step).

influence of heating on the output power. At 30 % (200 ns, 1.5 MHz), the maximum output power is reached, and for higher duty cycles, the power and the dynamic range decreases rapidly. The duty cycle, at which the power starts decreasing is also an indication whether the QCL could be operated in continuous-wave (cw) operation. As a rule of thumb, if the power increases up to 50 % duty cycle, it is very likely that it will lase in cw. If it starts decreasing earlier, as does the QCL shown in Fig. 2.10 b), the dynamic range will be zero before cw operation has been achieved. [95]

The electrical behavior of a QCL can hold information on the quality of the active region and of the process. Low voltage can be an indication for leakage current inside the device while infant fails can be caused by a high defect density along the laser ridge.

### 2.4.2 Spectral measurements

The optical characterization is equally important, especially if QCLs have to be selected for broadband performance. In devices with a good population inversion, the shape of the electroluminescence resembles closely the true gain shape. Thus, electroluminescence is a central part in assessing the gain shape and bandwidth of an active region. It is important to avoid amplification of the emission in order to prevent optical gain to distort the true gain shape. A common approach to avoid a multi-pass through the

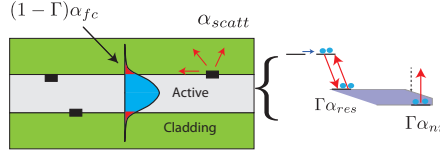


**Figure 2.12:** SOURCE: Faist [95]. Schematic overview on the different loss mechanism in a QCL.

device is extracting the light through a  $45^\circ$  wedge of mesa structures, or through the side of a QCL ridge.

Due to the low radiative efficiency ( $\sim 10^{-6}$ ), the intensity of electroluminescent light is very low and a sensitive collection apparatus has to be employed. Very good results are achieved with Fourier Transform InfraRed spectrometers (FTIRs) in step scan mode and a liquid Nitrogen cooled mercury-cadmium-telluride (MCT) detector. With a resolution of  $16 \text{ cm}^{-1}$ , spectra with a high SNR can be obtained within 10-30 min. Fig. 2.11 a) shows electroluminescence spectra at different electric fields. The narrowing of the curves with increasing current can be nicely observed.

In contrast, laser spectra do not suffer from signal-over-noise limitations due to their high output powers. Thus laser spectra can be measured in rapid scan mode of the FTIR and in general, a room temperature thermal detector, such as a deuterated triglycine sulfate detector (DTGS), and achieve the requirements of measurement speed as well as spectral accuracy and signal-to-noise ratios.

## 2.5 Loss measurements

To further characterize and improve active regions, it is very important to be able to determine the losses as well as the gain. The electrical and optical behavior of a QCL device will be influenced by different types of losses. There are, of course, the mirror losses that come from the facet reflectivities and can be modified by applying appropriate coatings on the facets. But especially the values of the waveguide losses are important, as they limit both the threshold current density and the slope efficiency.

### 2.5.1 Mirror losses and reflectivities

The laser cavity of a QCL is provided by the cleaved facets which have an as-cleaved mirror reflectivity that can be calculated as

$$R = \left( \frac{n_{\text{sub}} - n_{\text{air}}}{n_{\text{sub}} + n_{\text{air}}} \right)^2 = 0.287 \quad (2.12)$$

where  $n_{\text{sub}} = 3.31$  is the average refractive index of the QCL active region and  $n_{\text{air}} = 1$  is the refractive index of air. Increasing the back facet mirror reflectivity close to 1, the power collected through the front facet should nearly double. To achieve such high mirror reflectivities, a metallic high-reflection (HR) coating is applied to the back facet. The details of such coatings is discussed in detail in chapter 4.

Let us consider the simplest expression for the threshold condition in a QCL

$$g\Gamma J_{\text{th}} = \alpha_m + \alpha_{\text{wg}}, \quad (2.13)$$

where  $g$  is the differential gain,  $\Gamma$  the modal overlap factor of the optical light with the active region and

$$\alpha_m = -\frac{1}{l} \ln R_1 R_2 \quad (2.14)$$

the mirror losses, with  $R_1$  and  $R_2$  the front and back mirror reflectivities, respectively, and  $l$  the QCL chip length. When a laser facet is coated with a high- or anti-reflection coating, the change in threshold current density allows us to calculate the effective mirror reflectivities of the laser. This holds for any set of coated or uncoated facets as long as the threshold current density in both situations are known. The ratio of both threshold current densities can be written as

$$\rho \doteq \frac{J_{\text{th},2}}{J_{\text{th},1}} = \frac{\alpha_{\text{wg}} - \frac{1}{2l} \ln(R_1 \cdot R_2)}{\alpha_{\text{wg}} - \frac{1}{2l} \ln(R_1^2)} \quad (2.15)$$

and solving for  $R_2$  recovers the back facet reflectivity  $R_2$

$$R_2 = R_1^{(2\rho-1)} \cdot e^{-2l(\rho-1)\alpha_{\text{wg}}} \quad (2.16)$$

This technique to recover the facet reflectivities from the change of threshold can be used to verify the reflectivities of coatings that were applied to the facets, as will be described in chapter 4.

### 2.5.2 Waveguide losses

Waveguide losses comprise different loss mechanisms which are schematically shown in Fig. 2.12. Firstly, there are the cladding losses  $((1 - \Gamma)\alpha_{fc})$ , which mostly originate from the free carrier absorption  $\alpha_{fc}$ . Secondly, the scattering losses which are directly related to the processing, since they arise from defects along the active region, i.e. the sidewall roughness. Thirdly, the non-resonant losses, which are related to all the other transitions in the active region. And finally, the resonant losses  $(\Gamma\alpha_{res})$ . The resonant absorption  $\alpha_{res} = g_c n_2^{\text{therm}}$  arises when electrons are thermally excited to the lower laser state, reducing the population inversion  $\Delta N$ . This effect, however, only affects the threshold current density and not the slope efficiency. Thus the total losses can be written as

$$\alpha_{\text{tot}}^{\text{wg}} = (1 - \Gamma)\alpha_{fc} + \alpha_{\text{scatt}} + \Gamma\alpha_{nr}, \quad (2.17)$$

where  $\Gamma$  is the overlap factor of the optical mode with the active region. The waveguide losses of a device depend on many different intrinsic parameters such as free carrier absorption, scattering losses and intersubband losses in the active region. Having an estimate of the waveguide losses of a process helps understanding the LIV characteristics and finding the problematic parts of a laser.

There are different ways of calculating the waveguide losses based on experimental data. We briefly present two calculation approaches and compare them in terms of their reliability.

#### Threshold-ratio method

As mentioned above, the mirror reflectivities can be calculated according to equation 2.16. When applying a coating to a laser facet and determining the threshold current density before and after the coating process, the waveguide losses can be calculated by solving equation 2.15 for  $\alpha_{\text{wg}}$ :

$$\alpha_{\text{wg}} = \frac{1}{2l(1 - \rho)} \cdot \ln \left( \frac{R_{\text{HR}}}{R_{\text{f}}^{(2\rho-1)}} \right). \quad (2.18)$$

The losses (and the gain) are given per length in units of  $\text{cm}^{-1}$ .

### Inverse-length method

From

$$g\Gamma J_{\text{th}} = \alpha_{\text{tot}} \quad (2.19)$$

and

$$\alpha_{\text{tot}} = \alpha_{\text{wg}} + \alpha_{\text{m}} = \alpha_{\text{wg}} + \frac{1}{2l} \ln \frac{1}{R_1 R_2}, \quad (2.20)$$

we observe that the threshold current density depends only on the waveguide losses and the inverse length of the chip.  $l$  and  $J_{\text{th}}$  can be measured leaving us with  $\alpha_{\text{wg}}$  as the only unknown parameter. The following linear relation between the chip length and threshold current density can be deduced

$$J_{\text{th}} = \underbrace{\frac{\alpha_{\text{wg}}}{g\Gamma}}_a - \frac{1}{l} \underbrace{\frac{\ln R_f}{g\Gamma}}_m, \quad (2.21)$$

with  $a$  the y-axis intercept and  $m$  being the slope. We then estimate the parameters  $a$  and  $m$  with a linear fit to the measured data for  $J_{\text{th}}$  and  $1/l$ , and finally obtain  $\alpha_{\text{wg}}$  as

$$\alpha_{\text{wg}} = \frac{a}{m} \ln R_f. \quad (2.22)$$



---

# Dielectric coatings: Materials and Fabrication

This chapter reviews the requirements and properties of materials used for dielectric coatings and the fabrication of such. The optical as well as mechanical properties of semiconductors and dielectric materials have to be considered to achieve good coatings. A selection of materials and their respective fabrication technique will be discussed.

### 3.1 Introduction

The materials used to achieve high-quality coatings have to fulfil the refractive index requirement stated in Eq. 4.17. Additional to the appropriate refractive index and absorption coefficient, mechanical properties and evaporation behavior have to be considered to find a suitable material. The refractive index and the absorption coefficient have to be known for a large wavelength range. Ideally, the material exhibits a flat dependence of the refractive index and absorption coefficient with wavelength.

Keeping the lattice mismatch between the substrate and coating material minimal will reduce the strain on the layer and thus reduce the risk of dislocations or peeling. Another mechanical consideration is the porosity of materials. Porous materials can absorb air humidity, leading to unwanted absorption features and to a reduction of the durability of coatings. Some dielectric materials are known to have poor adhesion to

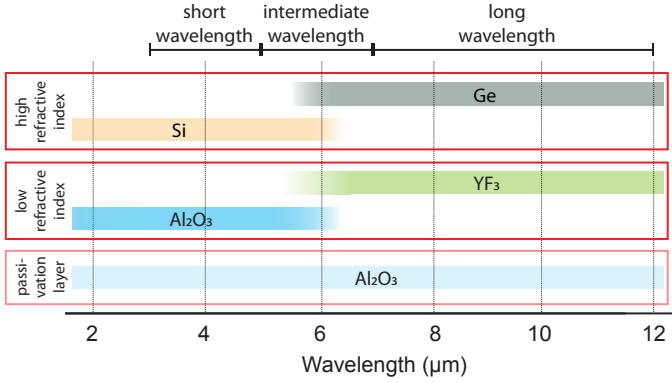


**Figure 3.1:** Materials used in this work and wavelength ranges they were used for. In the intermediate wavelength range around  $6\ \mu\text{m}$  it could be beneficiary to use either material of both the high and low refractive index category due to individual considerations for each case.  $\text{Al}_2\text{O}_3$  was always used as a passivation layer since no other material with the same environmental robustness was at hand. Therefore the absorption was neglected due to the thin layer thicknesses for passivation layers.

certain other material compounds. To prevent the layers from peeling off, adhesion promoters in form of thin intermediate layers can be applied. Those materials should not impact the optical properties of the coating and can be used wherever needed, with some limitations.

Finally, the behavior of the material under different evaporation techniques has to be considered. Some materials are readily deposited by thermal evaporation while they evaporate poorly by electron-beam. Others can be evaporated by both methods but show different layer qualities depending on the evaporation parameters. Thus great care has to be taken fine tuning these parameters.

In this work several materials were investigated and the selection was narrowed down to four materials that were used for the majority of the coatings. Si and Ge were used as high-index materials and  $\text{YF}_3$  and  $\text{Al}_2\text{O}_3$  as low-index materials. Fig. 3.1 shows the wavelength ranges for which the different materials were used. Fig. 3.2 shows the refractive index  $n$  and absorption coefficients  $k$  used in this work. The range of deposition techniques is very wide but due to the limited technical possibilities this work focuses on coatings realized by electron-beam evaporation.

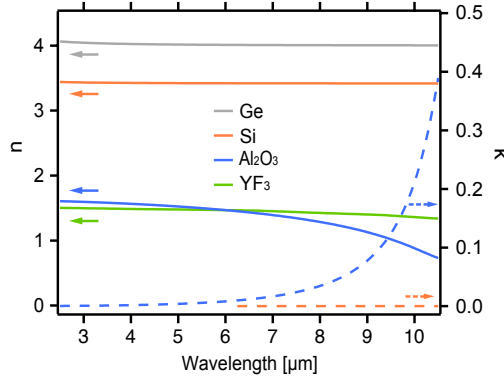


**Figure 3.2:** Refractive indices for the coating materials used for a majority of coatings presented in this work. DATA SOURCE: [124, 125].

### 3.2 Materials

This section summarizes some specific properties of the four main materials used in this work.

For the mid-infrared wavelength region from 3 to 5.5  $\mu\text{m}$ ,  $\text{Al}_2\text{O}_3$  is used as low-index material. For wavelengths longer than 5.5  $\mu\text{m}$ , the absorption increases, see Fig. 3.2, which limits its utility to the shorter wavelength regime. As high-index material both Ge and Si can be used throughout the mid-IR, although Ge would seem preferable due to the higher refractive index.

For wavelengths from 3 – 4.5  $\mu\text{m}$  Si shows excellent long term stability and low diffusion into the low-index materials. On the other hand, in the range from 4.5 to 5.5  $\mu\text{m}$  Ge proved to be the better choice due to the higher refractive index and thus smaller total layer thicknesses. If the lattice constant mismatch of materials is high, small individual layer thicknesses prevent a build up of excessive strain. Thus thinner layers have to be traded with more repetitions to achieve the same reflectivity. Using a material with a higher refractive index, such as Ge can help alleviate the problem for longer wavelengths.

Therefore, the high-index material used for the long wavelength region (6 – 11  $\mu\text{m}$ ) is Ge. Since the absorption coefficient of  $\text{Al}_2\text{O}_3$  prevents its use

in this wavelength region,  $\text{YF}_3$  is used instead. It only shows significant absorption for wavelengths  $\geq 10 \mu\text{m}$ . The material itself, however, has its challenges due to its porous structure which is prone to absorb air humidity.

#### 3.2.1 $\text{Al}_2\text{O}_3$

$\text{Al}_2\text{O}_3$  is a well known low-index material for the near-IR. This material is primarily used from 3 to  $5.5 \mu\text{m}$  wavelength (cf. Fig. 3.1) due to its transparency. Fig. 3.2 shows that for this short wavelength part of the mid-IR range  $\text{Al}_2\text{O}_3$  has a near to constant refractive index and negligible absorption. It is easily evaporated by electron beam and forms hard and durable layers which adhere well to InP. It withstands thermal cycling and humidity without cracking or peeling off. For wavelengths  $\geq 6 \mu\text{m}$ , however, the absorption increases significantly and consequently the energy density inside the coating would lead to immediate catastrophic mirror damage. Due to  $\text{Al}_2\text{O}_3$ 's excellent mechanical properties it is a favorable material for protective layers, i.e. passivation layers to prevent oxidation or absorption of humidity by the top coating layer. The thickness of such a passivation layer has to be chosen carefully to ensure full coverage of the top layer, but keep the absorption inside the  $\text{Al}_2\text{O}_3$  minimal. For e-beam evaporators the shape of the vapor cloud strongly depends on the surface morphology of the material inside the crucible. Thus, reproducibly uniform coating runs require packing the material tightly inside the crucible to form a homogenous and flat surface.

#### 3.2.2 $\text{YF}_3$

$\text{YF}_3$  is another low-index material for the mid-IR with a refractive index around 1.4 over a range from 3 –  $10 \mu\text{m}$  wavelength and negligible absorption (Fig. 3.2). Such a constant refractive index reduces the dependence of the final layer reflectance on the material thickness. Any deviation in layer thickness influences the reflectivity linearly. The material is also known to behave well under e-beam evaporation. First tests with  $\text{YF}_3$  layer thicknesses up to several hundred nanometers were promising when considering durability. However, depositing thicker layers revealed

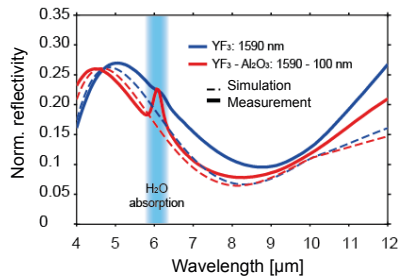


**Figure 3.3:** Simulation (dashed line) and measurement (straight line) of a single  $\text{YF}_3$  layer (not optimized for reflectivity) with (blue) and without (red) a 100 nm  $\text{Al}_2\text{O}_3$  passivation layer. The passivation layer prevents the  $\text{YF}_3$  layer from absorbing  $\text{H}_2\text{O}$  from air humidity.

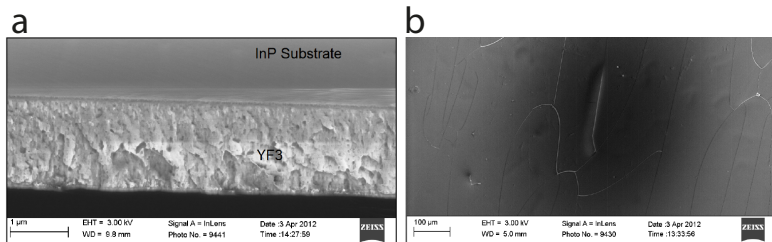


**Figure 3.4:** a) Cross section of a 1.5  $\mu\text{m}$  thick  $\text{YF}_3$  layer showing the porosity of the material. b) A relaxed 1.5  $\mu\text{m}$  thick  $\text{YF}_3$  layer shows the difficulty of depositing thick layers for long wavelengths applications.

a tendency of  $\text{YF}_3$  to crack, as evidenced by Fig. 3.4 b). Further investigations showed that  $\text{YF}_3$  absorbs air humidity, reducing the durability of the layers due to cracking and peeling within days. We attributed this to the porosity of the  $\text{YF}_3$  layer absorbing air humidity. Adding a passivation layer of 50 - 100 nm  $\text{Al}_2\text{O}_3$  increased the lifetime of the coatings from days to weeks without significantly changing the optical properties of the coatings. Fig. 3.3 shows a 1.59  $\mu\text{m}$  thick  $\text{YF}_3$  layer with a strong water absorption around 6  $\mu\text{m}$ . In a second deposition a 1.59  $\mu\text{m}$  thick  $\text{YF}_3$  was capped with 100 nm of  $\text{Al}_2\text{O}_3$ , significantly reducing the strength of the water absorption. It is to be noted, that this solution has to be used carefully, as the absorption of the  $\text{Al}_2\text{O}_3$  should be included in the simulation of the coating reflectivity.

#### 3.2.3 Germanium

Germanium is a high-index material with good behavior under e-beam evaporation. It has a refractive index above 4 over the whole mid-IR range and a negligible absorption coefficient (see Fig. 3.2) and is a good candidate for the whole MIR wavelength range. Ge is a skin-forming material, see section 3.3.1, which has to be heated up carefully, but can be evaporated at high rates and it forms uniform layers.

#### 3.2.4 Silicon

Si is similar to germanium, but with a slightly lower refractive index. It is a good candidate as high-index material over the whole mid-IR range. Depositing Si by e-beam creates an amorphous layer which can have reduced long term stability compared to crystalline layers. Si has to be deposited at high deposition rates to form uniform layers and requires a minimal thickness of approximately 50 nm to form a continuous layer. It has been reported that Si can diffuse into other semiconductor materials such as GaAs. This can change the doping profile of the quantum wells and ultimately lead to a catastrophic mirror failure.

#### 3.2.5 Other materials

Apart from the aforementioned low-index materials, there is a selection of alternative candidates that also find wide applications in the MIR in industry. Here, ZnSe and SiO will be discussed shortly as alternatives.

**ZnSe** is a material with a relatively constant refractive index of  $2.43 \geq n_{\text{ZnSe}} \geq 2.4$  from  $3 \mu\text{m}$  to  $11 \mu\text{m}$  and a negligible absorption coefficient over the whole infrared range. It exhibits excellent behavior under e-beam evaporation and results in homogenous layers that have good adhesion properties on InP based semiconductor materials. However, adhesion problems on GaAs based systems have been reported. As can be seen from Fig. 3.5, ZnSe has a rather high refractive index for a low-index material, which will increase the layer thickness for  $\lambda/4$  layers. To keep the layer thickness to a minimum, it should be paired with a material with a very high refractive index, such as Ge, see Fig. 3.2. [126, 127] However, contact with skin and breathing of ZnSe dust has to be avoided. These health

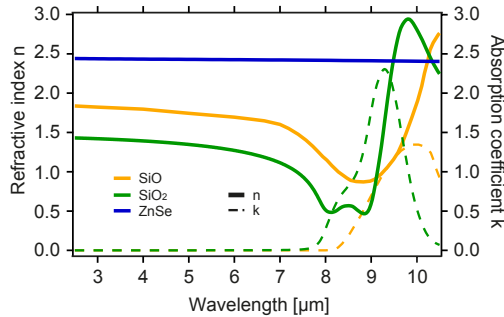


**Figure 3.5:** Refractive indices of ZnSe, SiO and SiO<sub>2</sub> for the mid-IR range. SiO and SiO<sub>2</sub> exhibit strong absorption peaks above 8 μm wavelength, limiting their use to shorter wavelengths. ZnSe, although having a high refractive index, does not have any absorption and a constant refractive index. DATA SOURCE: [126, 127, 128, 129]

considerations were the main reason this material could not be used in the ETH clean room facilities. Therefore, this material, even though having excellent qualities for our purposes, was not in the selection of materials considered for our coatings.

**SiO** is another material that is widely used in industry. It exhibits excellent adhesion properties and does not pose any health threats. SiO has an absorption peak above 7.5 μm that limits the use of it to wavelengths below that. However, it has to be evaporated either thermally, or indirectly by e-beam. As soon as the material heats up, the SiO granulate will start to spit and it is impossible to evaporate from open boats or crucibles. For both techniques the crucible or the boat needs a lid that will prevent the material from spitting. For thermal evaporation tungsten (W) baffled box boats are commercially available in a variety of sizes. E-beam crucibles have to be fitted with a tungsten lid. This lid needs to be permanently fixed and have an opening for refilling the SiO. Covered tungsten crucibles are available for big industrial sized evaporator systems but not for the small crucible size of the machine used here. Thus we had to refrain from testing SiO further for our purposes. [128]

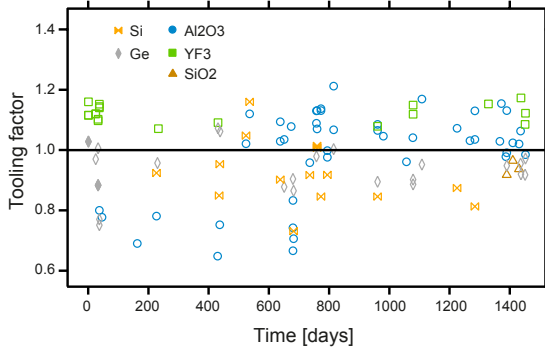


Figure 3.6: Evolution of the geometric tooling factor over time.

### 3.2.6 Tooling factor

Depositing the correct layer thickness is crucial to produce reliable and reproducible coatings. Therefore, the deposition rate and layer thickness is measured by two quartz crystal monitors mounted close to the sample position. The quartz crystals measure the change in their eigenfrequency during the deposition. With the knowledge of the acoustic impedance and the material density, an effective thickness can be calculated. Due to the inhomogeneous distribution within the material vapor cloud and the position offset between the crystal and sample, the thickness measurement by the crystal will differ from the real layer thickness. To account for this difference a geometric correction factor, called tooling factor, has to be taken into account when calculating deposition times. Since the shape of the material vapor cone depends on the surface of the material and the heating sequence of the material, the tooling factor can vary over time. Thus a calibration deposition for every material was done before every real coating run.

To determine the individual tooling factors, pieces of GaAs wafer were coated with single layers of each material at a known and fixed deposition rate. The nominal thickness, the thickness measured by the crystal monitors, was compared to the real thickness on the sample, measured with a surface profiler (Dektak). The ratio of the two numbers yields the



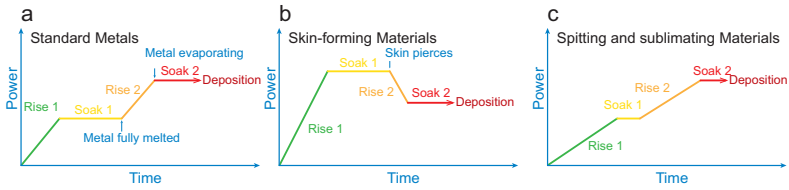


**Figure 3.7:** Schematic representation of the soak and rise times applied for different materials. **a)** For standard metals the beam power is turned up and the metal is molten at an appropriate value. When fully melted, the power is increased up to the point where the final evaporation rate is reached. **b)** Some materials, mostly metals, form a solid skin around molten core which has to be pierced at a higher power than the actual evaporation. **c)** Some magnetic materials tend to spit when hit with the electron beam and a slow increase in power is required to heat up or melt the material.

tooling factor. Fig. 3.6 shows how the tooling factors changed over time. The graph shows that Si, Ge and  $\text{YF}_3$  have a relatively constant tooling factor, whereas  $\text{Al}_2\text{O}_3$  shows a much more inconsistent behavior. This can be explained by the surface structure and melting behavior. Si, Ge and  $\text{YF}_3$  all melt and have a clearly defined surface and shape. For  $\text{Al}_2\text{O}_3$  on the other hand, the vapor cone will change with the consumption of the material within the crucible.

### 3.3 Fabrication

This section describes the evaporation procedures for different material groups and surface preparation protocols set in place to improve reproducibility and reliability of the coatings.

#### 3.3.1 Deposition technique

All coatings were fabricated with an electron-beam evaporator (Univex500, Oerlikon Leybold Vacuum) from the cleanroom facilities at ETH Zurich, Switzerland, and evaporated either by e-beam or thermal evaporation. The base pressure of the main chamber was in the order of  $10^{-6}$  mbar and increased to  $10^{-5}$  mbar during evaporation. The distance between the target material and the rotating sample holder was 50 cm. The crucible carousel had 6 pockets and the vapor beam had a divergence between  $5^\circ$  and  $8^\circ$  covering sample sizes up to 4-inch diameter. To avoid cross con-

tamination, the materials were cooled down after evaporation and before rotating to the next material. The e-beam and the thermal evaporation boat were powered by a 10 kV source and for the evaporation by e-beam currents between 15 and 120 mA were applied.

Materials evaporated by e-beam can be categorized according to their melting behavior.

**Standard metals** have a melting point well below their vapor pressure and can be evaporated without problems. Fig. 3.7 a) shows a simplified diagram of the procedure: The beam power is increased until the metal starts melting and is then kept constant until the material is fully melted. The power is further increased until the final evaporation rate is reached and the power is kept constant to stabilize the rate. Good thermal conduction and convection in the metal ensures a homogeneous heating of the material with no need to sweep the e-beam over the whole surface. Materials in this category are Copper, Gold and Titanium.

Some materials, mostly metals and some semiconductors, form a solid skin around the molten core. These are called **drum melts**. Due to the skin formation a modified heating procedure is necessary as shown schematically in Fig. 3.7 b). Initially, the beam power is increased above the value for evaporation and is kept constant until the skin is pierced. The power is then reduced and the rate stabilized for deposition. Materials like Silver, Tin, Germanium and Silicon belong to this group of materials.

**Sublimating materials** have yet another behavior owed to a melting point at or above vapor pressure. These materials do not form good melts and have a poor heat distribution. They need to be heated up slowly as indicated in Fig. 3.7 c). Additionally, the e-beam has to be swept over the material to heat it evenly. If the beam is kept in one position, the material will be fully consumed at this position. This can lead to an unexpected and fast decrease of the rate. Materials such as Chrome, Zinc, Tungsten, Molybdenum, Tantalum and most dielectric material compounds such as  $\text{Al}_2\text{O}_3$  and  $\text{SiO}_2$  belong to this category.

Another group of materials that has to be treated in a similar way as sublimating materials are **spitting materials**. Most magnetic materials, if not carefully heated up with the e-beam, jump out of the crucible. Sweep-

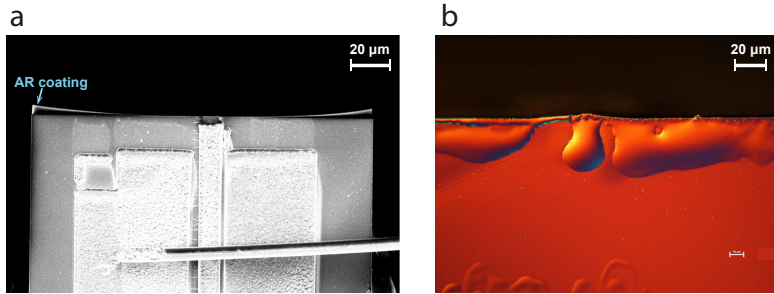


**Figure 3.8:** **a)** Top view of a front facet with an AR coating peeling off at the etches. **b)** AR coated front facet. The coating blisters due to surface preparation with wet chemistry, cf. Table 3.1.

ing the e-beam at a very low power  $\leq 1$  mA over the material demagnetizes it and prevents it from spitting. Other materials, if heated up too fast, boil over and spill over the top of the crucible. SiO is a special case inside the spitting materials since it can only be evaporated with a covered crucible or by thermal evaporation.

The preparation of the materials and the heating sequence can strongly influence the quality of the coatings since the surface shape of the material determines the shape of the vapor cloud and thus the homogeneity of the layers.

### 3.3.2 Adhesion promoters and surface preparation

Initially, the facets of the lasers were coated as cleaved with no further treatment. That resulted in sticking problems and coatings peeling off, sometimes instantaneously, sometimes after being exposed to ambient air for some days. Fig. 3.8 a) shows a coating that peeled off on the top of the facet. It was suspected that the stress within individual layers and between layers caused the degradation. To counteract this effect, thin layers of Ti were applied as stress relieve and sticking layer. Even though an improvement in durability was observed, the Ti layers caused catastrophic mirror damage through absorption and the test was abandoned.

A concern for good adhesion properties to the facets was the duration between the moment a QCL was cleaved and coated. Initial findings sug-

gested that fresher facets showed better adhesion. It is known from other groups that coating unmounted laser facets yields very good results concerning long term stability. But as the behavior before and after coating is of some interest to the characterization of the device, we continued to mount and measure the devices before coating. Thus a cleaning or surface preparation procedure had to be applied.

A series of different cleaning sequences were tested and the results summarized in table 3.1. The wet chemistry cleaning procedures consisted of carefully wiping the facet with clean room grade cotton swabs to remove any particles adhering to the facet surface. That procedure was met with limited success. Although, after Aceton and Isopropanol (IPA) wiping, the facet looked clean to the eye, applying a coating to the facet resulted in blistering as shown in Fig. 3.8 b) and was observed for all the wet wiping procedures. A widely used preparation technique for semiconductor surfaces in the clean room at ETH is a UV ozone treatment. Neither alone nor in combination with other techniques did it yield good results and we suspect that the ozone treatment possibly was an additional source of surface contamination. Good results were obtained by treating the facet to a  $O_2$  plasma immediately before applying the coating. Initial tests were done for 30 s at 100 W and the power and time were increased to 150 W for 120 s at which parameters good and consistent adhesion was observed.

After the surface treatment the devices were immediately transferred into the vacuum chamber of the e-beam evaporator and coated as described in section 3.3.1.

Method	Effect	Comment
Wiping of the facet with Isopropanol	✗	Risk of facet scratching due to the use of cotton swabs. IPA is not enough to clean the surface from residuals.
Wiping of the facet with Aceton	✗	Some residues on the facet. Usually not around the active region, if device was mounted epi-up.
Wiping of the facet with IPA and Aceton	✗	Looks clean to the eye but blisters when a coating is applied (cf. Fig. 3.8b)).
UV Ozone treatment	✗	No positive effect on the adhesion observed.
Wiping of the facet with IPA plus Ozone treatment	✗	No positive effect on the adhesion observed.
Wiping of the facet with Aceton plus Ozone treatment	✗	No positive effect on the adhesion observed.
Wiping of the facet with IPA/Aceton plus Ozone treatment	✗	No positive effect on the adhesion observed.
Wiping of the facet with IPA plus O <sub>2</sub> plasma treatment	✗	Better adhesion in some cases.
Wiping of the facet with IPA/Aceton plus O <sub>2</sub> Plasma treatment	✗	Better adhesion in some cases.
Wiping of the facet with IPA/Aceton plus Ozone and O <sub>2</sub> Plasma treatment	✗	Better adhesion in some cases.
O <sub>2</sub> Plasma treatment	✓	Consistent adhesion with plasma treatment for 120 s at 150 W

**Table 3.1:** Test of different facet cleaning routines to improve adhesion of dielectric coatings on the facets. Wet chemistry solutions, facet wiping with a clean room grade swabs did partially improve sticking but also introduced air bubbles in the coating. Consistently good adhesion properties were only observed with pure O<sub>2</sub> plasma treatment at 150 W for 120 s.



---

# Dielectric AR and HR coatings in the mid-infrared

In this chapter, results on anti-reflection (AR), high-reflection (HR) and dispersion compensation coatings for use with Quantum Cascade Lasers (QCLs) are shown. Simulations are shown alongside measurements of single- and multi-layer coatings in the 3 to 11  $\mu\text{m}$  wavelength region. The impact of such coatings on the threshold current density and output power of QCLs is shown as well as the dispersion of QCL frequency combs.

## 4.1 Introduction

Coatings are used to modify reflectivities of lenses, windows, mirrors and laser facets for a variety of applications. Thin film coatings deposited on the QC laser facets allow the modification of their transmission and reflection. For example, QCLs operated in an external cavity need an AR coating to suppress Fabry-Pérot modes and consequently enhance the tuning range of the laser. Another application is the enhancement of the outcoupling efficiency.

Dielectric HR coatings are also important to prevent short circuiting epi-side down mounted QCLs. To improve the heat extraction, a device can be mounted epi-side down onto a AlN submount (cf. section 2.3). In this configuration the active region is very close to the submount and the risk of short-circuiting the device by applying a standard metallic HR

coating is very high, making a non-conductive HR coating more desirable. The reflectivity of both AR and HR coatings can be adjusted to satisfy the specific need of different applications.

QCLs can be operated as frequency combs, but it requires the refractive index dispersion to be as close to zero as possible. Multi-layer dielectric coatings can induce required negative or positive dispersion at specific wavelengths and therefore improve comb operation.

## 4.2 Theory

This section gives a short summary of the matrix formulation of isotropic layered media for TM- and TE-polarized light. For the full treatment, the reader is referred to *Optical Waves in Layered Media* by P. Yeh [130].

The transmittance and reflectance of the AR- and HR-coatings of QCLs can be calculated starting from Maxwell's equations which are complemented by the material equations. We only consider linear responses of the dielectric media, i.e. an electric polarization of  $\mathbf{P} = \varepsilon_0\chi\mathbf{E}$  (with  $\chi$  being the dielectric susceptibility) and nonmagnetic materials ( $\mu = \mu_0$ ). The wave equation for a linear, homogenous and isotropic media can be derived as

$$\nabla^2\mathbf{E} - \mu\varepsilon\frac{\partial^2\mathbf{E}}{\partial t^2} = 0, \quad (4.1)$$

where  $\varepsilon = \varepsilon_0(1 + \chi)$ . Stokes' and Gauss' divergence theorems then show that the tangential components of  $\mathbf{E}$  and  $\mathbf{H}$ , the electric and magnetic field vector, respectively, are continuous across the interface between two media, in case of zero surface charge and surface current density. From this, Snell's law can be derived:

$$n_1 \sin(\theta_1) = n_2 \sin(\theta_2) \quad (4.2)$$

where  $\theta_1$  and  $\theta_2$  are the incident and refracted angle, respectively.

As we only consider normal incidence we are more interested in the amplitudes of the reflected and transmitted waves. Starting from the general solution of the wave equation 4.1 as a superposition of reflected and transmitted waves on the boundary surface we find two relations for the



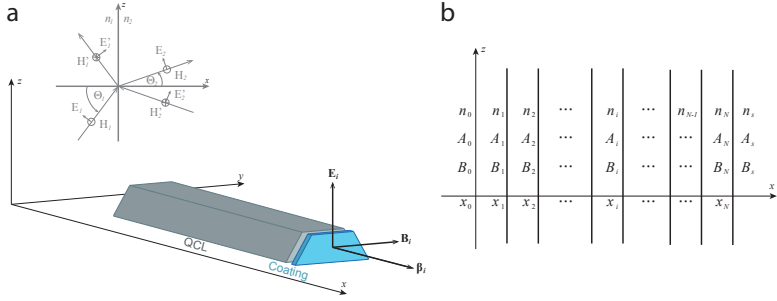


**Figure 4.1:** Propagation of electro-magnetic waves at dielectric boundaries: **a)** Schematic of a QCL waveguide with a TM-polarized output. The inset shows the reflection and refraction at such a boundary. **b)** Multilayer arrangement with left- and right-going wave amplitudes, position and refractive indices of the individual layers.

continuity of the tangential components of  $\mathbf{E}$  and  $\mathbf{H}$  in TM-polarization:

$$(E_1 + E'_1) \cos(\theta_1) = (E_2 + E'_2) \cos(\theta_2), \quad (4.3)$$

$$\sqrt{\frac{\epsilon_1}{\mu_1}}(E_1 - E'_1) = \sqrt{\frac{\epsilon_2}{\mu_2}}(E_2 - E'_2). \quad (4.4)$$

These relations can be written in matrix form:

$$\begin{pmatrix} E_1 \\ E'_1 \end{pmatrix} = D(1)^{-1} D(2) \begin{pmatrix} E_2 \\ E'_2 \end{pmatrix}, \quad (4.5)$$

where

$$D_{TM}(i) = \begin{pmatrix} \cos(\theta_i) & \cos(\theta_i) \\ \sqrt{\frac{\epsilon_i}{\mu_0}} & -\sqrt{\frac{\epsilon_i}{\mu_0}} \end{pmatrix} \quad (4.6)$$

is the dynamic matrix for a TM-polarized wave for medium  $i$ .

To describe the propagation of the wave across multiple thin-film layers of thicknesses  $d_i = x_i - x_{i-1}$  and refractive indices  $n_i$ , as shown schematically in Fig. 4.1 b), the propagation matrix  $P_i$  is introduced

$$P_i = \begin{pmatrix} e^{i\varphi_i} & 0 \\ 0 & e^{-i\varphi_i} \end{pmatrix} \quad (4.7)$$

which accounts for the phase change  $\varphi_i$ ,

$$\varphi_i = \frac{2\pi n_i d_i}{\lambda} \cos(\theta_i) \quad (4.8)$$

acquired by the light propagating through the medium layer  $i$ .  $A_i$  and  $B_i$  are the amplitudes of the right and left traveling wave in the different material layers as shown in Fig. 4.1 b). The whole propagation through all  $N$  layers, from medium 0 at  $x = x_0$  to medium  $s$  at  $x = x_N$  can be written in the following form

$$\begin{pmatrix} A_0 \\ B_0 \end{pmatrix} = \begin{pmatrix} M_{11} & M_{12} \\ M_{21} & M_{22} \end{pmatrix} \begin{pmatrix} A_s \\ B_s \end{pmatrix} \quad (4.9)$$

where  $M$  is given by

$$M = D_1^{-1} \left[ \prod_{l=1}^N D_l P_l D_l^{-1} \right] D_s. \quad (4.10)$$

From this the reflection  $r$  and transmission  $t$  can be obtained as

$$r = \frac{M_{21}}{M_{11}} \quad (4.11)$$

and

$$t = \frac{1}{M_{11}} \quad (4.12)$$

and for lossless media we find the reflectance  $R$

$$R = |r|^2 = \left| \frac{M_{21}}{M_{11}} \right| \quad (4.13)$$

and transmittance  $T$

$$T = \frac{n_s \cos(\theta_s)}{n_0 \cos(\theta_0)} |t|^2 = \frac{n_s \cos(\theta_s)}{n_0 \cos(\theta_0)} \left| \frac{1}{M_{11}} \right|^2. \quad (4.14)$$

Using the complex refractive index  $n = n_R + in_I$  takes the absorption  $n_I$  into account. The second term is related to the absorption coefficient in the following way:

$$\alpha = \frac{4\pi n_I}{\lambda}. \quad (4.15)$$

#### 4.2.1 High-reflection coatings

The most widely used HR coating for QCLs is a metallic HR coating. The laser back-facet is first coated with a layer of an electrically insulating material to prevent short circuiting the top and bottom contacts of the laser.

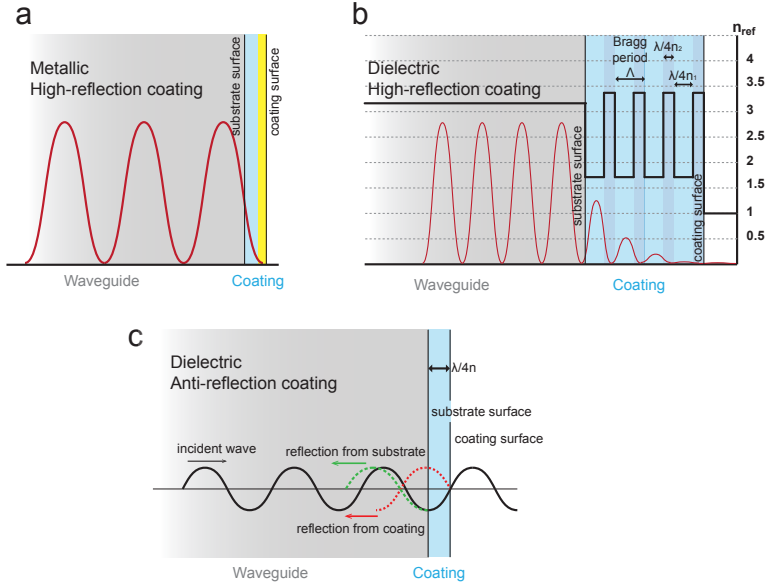


**Figure 4.2:** Schematic representation of the different coatings discussed. **a)** Standard HR coating with a layer of dielectrics to prevent electrical short-circuiting and a layer of gold as a mirror. **b)** Dielectric HR coating with several pairs consisting of a low- and a high-index material, effectively creating a Bragg mirror. **c)** The simplest version of a dielectric AR coating consisting of a single quarter wave layer to induce restructive interference.

Then a metallic layer is deposited, acting as a mirror. These coatings are easy to be manufactured and extremely durable. In certain cases, however, it is not possible or not advised to use a metallic HR coating. In such situations, fully dielectric mirrors can be used. They utilize the principle of the Bragg mirror [131], where a low refractive index material stack is interleaved with layers of a high refractive index, forming pairs of layers (cf. Fig. 4.2 b). The simplest dielectric mirror is a quarter wave stack. As the name suggests, both material layers have a thickness of  $d = \frac{\lambda}{4n}$ , forming half wave layer. Therefore, all reflected components from the interfaces interfere constructively, resulting in a strong reflection. The reflectivity of the coating increases with increasing number of layer pairs and the contrast of the two refractive indices. Fig. 4.2 b) shows a pictographic view of the refractive index values and the corresponding amplitudes.

### 4.2.2 Anti-reflection coatings

From the theory outlined in section 4.2 we know that to achieve minimum reflectance, we have to induce a phase change of  $\pi$  to have destructive interference at the interface (cf. Fig. 4.2 c). Thus minimum reflectance of a quarter wave layer at a certain given wavelength  $\lambda$  is achieved for a thickness fulfilling the following relation

$$d = \frac{\lambda}{4n}, \quad (4.16)$$

where  $n$  is the refractive index of the layer material at the wavelength  $\lambda$ . To achieve zero reflectance however, the refractive index of the dielectric material has to fulfill the following requirement

$$n = \sqrt{n_{\text{substrate}} n_{\text{air}}}. \quad (4.17)$$

If a material with the required refractive index is available, the thickness can be calculated and the coating is straightforward to manufacture since it only consists of a single layer. Finding a material that fulfils the refractive index requirement, resulting in non-zero reflectances, can be challenging. More often, a combination of two different materials with different refractive indices is used. Again, the simplest form consists of one pair of high- and low- refractive index materials. Such double-layer coatings are commonly known as V-coatings due to the resulting V-shape of the coating's reflectance as a function of the wavelength. In addition to zero reflectance, these coatings have the advantage over the single-layer coatings of being thinner, thus being easier to manufacture and more stable. But the V-coatings have a relatively narrow bandwidth. To achieve broader bandwidth, more layers have to be added. Such a third layer or a second pair of layers will act as an individual coating. If the designed center wavelength for the second coating is shifted from the center wavelength of the first pair, a double peak shape of the coating is created and thus a broader bandwidth is covered. To create broadband coatings the positions of the individual coatings have to be carefully planned.

### Simulation

The simulations were done using a Matlab code applying a generic algorithm optimization. The matrix equation 4.9 is solved iteratively for a

given wavelength range and layer sequence. Input parameters are the sequence of layer materials, the wavelength range in which to optimize the coating, and the desired final reflectivity.

In a first step a matrix with the refractive indices of the different materials as a function of wavelength is generated from existing data tables of the materials. Then a fitness function is defined with the parameter to be minimized, i.e. for an AR coating the sum square root of the reflectivity  $R$  ( $\text{sumsq}(R)$ ). The fitness function is then run through the genetic algorithm to find the individual layer thicknesses according to the optimized reflectivity.

### 4.2.3 Dispersion compensation with Gires -Tournois - interferometer mirrors

A new and promising branch of spectroscopy is owed to frequency combs. Optical frequency combs are generated when the different longitudinal laser modes are locked in phase [69, 132], creating an array of equidistantly spaced phase-coherent modes. Their discrete and equally spaced optical lines can be mapped into the radio frequency regime, allowing the application of radio frequency standards to the optical frequency regime.

QCLs are more and more often operated as frequency combs in different frequency regimes [133, 106, 134, 135]. They achieve frequency comb operation by four-wave-mixing (FWM) as a phase-locking mechanism [106, 136]. Since the FWM process starts to be efficient in the zero-dispersion region, it is important to know how the device dispersion of a QCL influences the comb operation. Thus it is of interest to find a way to compensate the introduced dispersion.

A first step is the optimization of the design of the active region and cladding layers [134]. Additionally, one can use a Gires-Tournois Interferometer (GTI) approach to integrate a dispersion compensation scheme [137] on the facet. GTIs are optical cavities specifically designed to introduce a certain amount of dispersion and are well established for solid state based mode-locked lasers [138]. GTI coatings are a combination of metallic and dielectric HR coatings and have a specific layer sequence schematically shown in Fig. 4.3. The coating acts as a cavity which modu-

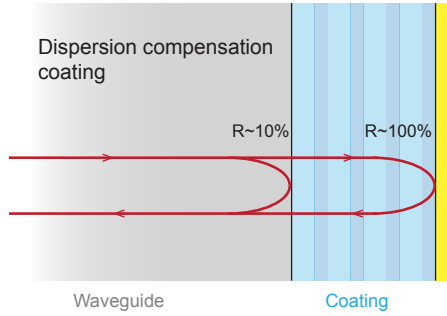


**Figure 4.3:** Schematic view of a GTI mirror deposited by e-beam evaporation onto the back facet of a QCL or on a InP substrate for reference measurements. The GTI acts as a HR coating but due to the well chosen layer thicknesses also introduces dispersion.

lates the phase as a function of the wavelength and thus allows to modify the dispersion.

### Simulation

The design of such mirrors starts with the analytical expression of the group delay dispersion (GDD) introduced by a perfectly transparent material:

$$GDD_{GTI} = -\frac{2\tau_0^2(1 - R_t)\sqrt{R_t}\sin(\omega\tau_0)}{(1 + R_t - 2\sqrt{R_t}\cos(\omega\tau_0))^2}, \quad (4.18)$$

with  $\tau_0$  the cavity roundtrip time,  $R_t$  the reflection coefficient at the interface between laser facet and GTI coating and  $\omega$  the optical frequency. From the total thickness of an ideally transparent material, a real coating with layers of different dielectric materials is composed that fulfills the requirements for the GDD in a certain wavelength range. Considerations that have to be taken into account are the set of available materials, the maximum possible thickness per layer and material and the evaporation behavior of said materials. (cf. chapter 3)

To numerically test the obtained layer sequence, according to the GDD the following expression for the phase spectrum can be considered:

$$\Delta\varphi(\omega) = \underbrace{\Delta\varphi_0}_{\text{absolute phase at } \omega_0} + (\omega - \omega_0) \underbrace{\left(\frac{d\Delta\varphi}{d\omega}\right)_{\omega_0}}_{\text{Group Delay}} + \frac{1}{2}(\omega - \omega_0)^2 \underbrace{\left(\frac{d^2\Delta\varphi}{d\omega^2}\right)_{\omega_0}}_{\text{GDD}}. \quad (4.19)$$

Since the GDD is defined as the second derivative of the relative phase  $\Delta\varphi$  with respect to  $\omega$ , the layers can be numerically tested by calculating the phase spectrum for the frequency range of interest and taking the second derivative. From this, the layers can be manually adapted if a different frequency regime has to be addressed.

#### 4.2.4 Graded index - Interface free coatings

Many coatings still suffer from an insufficiency at high laser powers. Even if the coatings applied to a high power laser contain materials with small absorption coefficients, the laser will suffer from a catastrophic mirror damage due to overheating. Even using the best conditions and most suitable materials, there will always be some absorption introduced by the sharp interfaces between the coating layers. The fast change in refractive index is needed to obtain the wanted effect of positive or negative interference, but abrupt change should be avoided. Therefore a gradual change of the refractive index by introducing a thin, less than one optical wavelength, mixing region is advised. As the evaporation equipment at hand did not have such a feature, gradual interfaces could not be implemented.

### 4.3 Measurement setup

To check the coating quality and measure the reflectivity as a function of wavelength, reference samples were manufactured for every coating run. They consist of low doped ( $1 \times 10^{15} \text{ cm}^{-3}$ ) double-side polished Indium Phosphite (InP) wafers ( $320 \text{ }\mu\text{m}$  thick) which are coated in parallel to the real sample, with the respective layer sequence. Reflection and transmission measurements were conducted on the reference samples in a Vertex 80v and Vertex 80 FTIR, respectively.

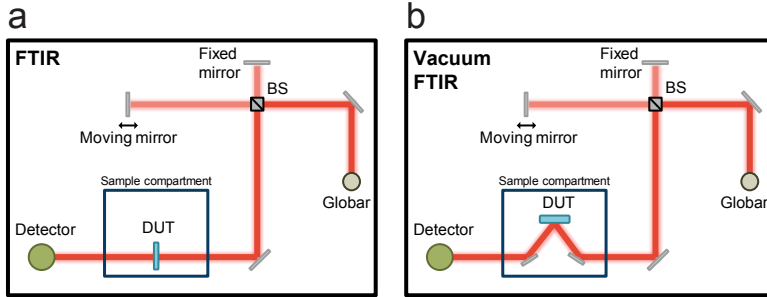


**Figure 4.4:** **a)** Schematics of the setup for transmission measurements of the AR and HR samples. The device under test (DUT) is placed in the sample compartment of a FTIR (Bruker Vertex 80) and purged with nitrogen to eliminate any absorption unrelated to the device. **b)** Schematics of the setup for reflection measurements for the GTI mirrors. The device under test (DUT) is placed in the sample compartment of a vacuum FTIR (Bruker Vertex 80v).

#### 4.3.1 Transmission measurement

To measure the transmission of AR or HR coatings in a Fourier-transform interferometer, a sample holder with a circular opening of 1.5 mm diameter was placed in the focus of the beam of the FTIR. The setup is schematically shown in Fig. 4.4 a). Three transmission measurements were taken per sample; one background scan, i.e. through the empty pinhole, one with the mean transmission through the uncoated InP substrate, and the mean transmission through the one side coated InP reference sample. From the ratio of the InP reference to the background scan and the coated sample to the background scan the transmission through the sample was calculated. Assuming no absorption, energy conservation  $T + R = 1$  holds and the reflectance can be calculated from the measured transmission. If the sample is absorbing, the measurement will show a higher reflectivity than it actually has.

#### 4.3.2 Reflection measurement

The characterization of the GTI coatings is done by placing the sample on a reflection holder inside the sample compartment of a vacuum FTIR (Bruker Vertex 80v). The recombined beam reflects off the coated surface with near normal incidence and the signal is measured with the inter-



nal DTGS (deuterated triglycine sulfate) detector. The schematics of the setup are shown in Fig. 4.4 b). A typical interferogram has a strong center burst, corresponding to the position of the moving mirror of the FTIR. The interesting feature, however, are the several small satellites that can be observed which stem from the multiple roundtrips of the light inside the GTI mirror. The first satellite originates from the single roundtrip of the light and thus contains the information about the introduced dispersion.

To extract the introduced dispersion from the interferogram, the first satellite is numerically isolated and apodized. Then a Fourier transform (Fast Fourier Transform algorithm) is performed and the phase spectrum computed. Using Eq. 4.19, the GDD is obtained by computing the second derivative of the obtained phase spectrum with respect to the frequency  $\omega$ .

## 4.4 Results

This section gives an overview on different manufactured coatings. High-reflectivity coatings will be discussed as well as anti-reflection coatings and integrated Gire-Tournois-Interferometers acting as dispersion compensation coatings. Some shortcomings of the design and manufacturing process are highlighted.

Some examples of AR coatings at different wavelengths and with different layer configurations are shown, illustrating how such coatings can cover various bandwidths. Similarly, the reflectivity of dielectric HR coatings can be adjusted from full dielectric mirrors to partial HR coatings with reflectivities of  $R \approx 40\%$ .

### 4.4.1 High-reflection coatings

For QCLs that are mounted epi-side up, cf. Fig. 2.8 a), the backside HR coating is by default a metallic coating resulting in an almost perfect mirror for the MIR range. This standard metallic HR coating consists of an insulating layer of  $\text{Al}_2\text{O}_3$  ( $\approx 200$  nm) followed by a layer of gold ( $\approx 100$  nm), where the insulating layer prevents the top and bottom contacts of the QCL to short circuit. Fig. 4.5 a) shows the simulated and measured re-

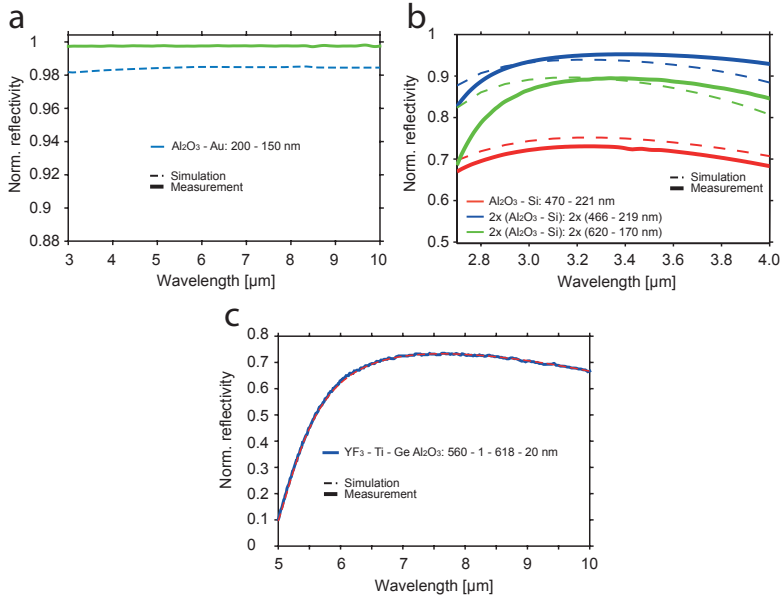


**Figure 4.5:** High-reflectivity coatings: **a)** Standard HR coating ( $\approx 200$  nm  $\text{Al}_2\text{O}_3$  and  $\approx 100$  nm Au). Gold acts as a near perfect mirror in this wavelength range. **b)** Simulation (dashed line) and measurement (straight line) of two dielectric HR coatings for a reflectivity of 90 % (green) and 94 % (blue). The coatings consist of two pairs of low- and high-index materials: 2x ( $\text{Al}_2\text{O}_3$ -Si) with layer thicknesses of 2x (620 nm - 170 nm) (green) and 2x (466 nm - 219 nm) (blue). **c)** Dielectric HR coating with a thin titanium layer as adhesion promoter. The coating was designed and fabricated as a partial front facet HR coating and has a reflectivity around 70 % between the wavelengths of 6 and 10  $\mu\text{m}$ .

sults of such a metallic HR coating with reflectivities close to 100 %, as expected.

QCLs that are mounted epi-side down, see Fig. 2.8 b), have a very high risk of short circuiting when a metallic HR coating is applied. Thus a dielectric coating is preferable to exclude any risks. Dielectric HR coatings can consist of either a single low/high-index pair or of a stack of such pairs. Figure 4.5 b) shows the simulation and measurement of dielectric HR coatings in the range of 3 to 4  $\mu\text{m}$  using  $\text{Al}_2\text{O}_3$  and Si as low- and high-index material, respectively. A single pair optimized for that wavelength range only reaches a maximum reflectivity of 70% whereas two repetitions of the same pair bring the reflectivity up to over 90%. Additional material-

pair layers would increase the reflectivity even further until the desired reflectivity is obtained.

For certain applications, for example to lower the threshold current density, only partial HR coatings are needed. In such cases, single material-pair layers can be of advantage to artificially reduce the reflectivity to values around 70 %. With the correct layer sequence design, reflectivities between a few percent up to nearly 100 percent can be achieved continuously. The green line in Fig. 4.5 b) shows a HR coating that was designed to have a reflectivity of 90 % at  $\approx 3.3 \mu\text{m}$  even though higher reflectivities could have been manufactured.

The dielectric HR coating shown in Fig. 4.5 c) was designed to reduce the lasing threshold but keep a substantial part of the extracted light. Thus a partial front facet HR coating with 70 % reflectivity was designed and applied to the facets. Fig. 4.5 c) shows another approach that can be taken when targeting an intermediate reflectivity value for the coating. Since dielectric coatings are wavelength dependent, different reflectivities can be achieved by offsetting the coating center wavelength in order to position the lasing wavelength on the side slope of the reflectivity curve. However, this approach is more vulnerable to changes in the layer thickness and should therefore not be the first choice when designing partial HR coatings.

#### 4.4.2 Anti-reflection coatings

As mentioned in section 4.2, thin film coatings can consist of a single or multiple layers of low- and high-refractive index materials. Here we will investigate one-, two- and three-layer AR coatings in simulation and experiment. Fig. 4.6 visualizes the concept of such single-, double- and multi-layer coatings.

The simplest AR coatings consist of a single layer of a low-index material with a thickness of  $\lambda/4n$ . The advantage of such coatings lies in the straightforward thickness computation and the simple deposition. On the other hand, such coatings have a narrow bandwidth for which the reflectivity might fulfill the requirements, cf. Fig. 4.6 a). Single-layer coatings indeed have an upper limit to reflectivities that can be achieved. Fig. 4.7

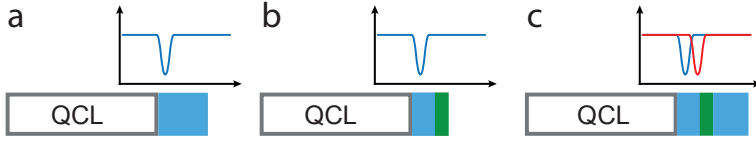


**Figure 4.6:** Schematic visualization of the principle of multi-wavelength coatings: **a)** a single layer reduces the reflectivity for a narrow bandwidth around a center frequency. **b)** A pair of a low- and a high-index material reduce the reflectivity achievable by the coating, but does not broaden the bandwidth. The pair effectively acts as a single coating. **c)** A third layer (or a second pair of layers) adds a single-wavelength coating at a shifted center wavelength and the overlap of both coatings constitute a broad bandwidth coating.

shows the good agreement between the simulation and the measurement, emphasizing the simplicity of such coatings.

As mentioned above, adding a second layer of a high-index material, cf. Fig. 4.6 b), reduces the total coating thickness but does not broaden the bandwidth of the coating. It does, however, ensure low reflectivities for single wavelengths. Fig. 4.7 shows a single layer  $\text{Al}_2\text{O}_3$  coating (400 nm) and two double layer coatings ( $\text{Al}_2\text{O}_3$  – Si (320 nm – 25 nm);  $\text{Al}_2\text{O}_3$  – Ge (330 nm – 20 nm)). The total thickness of the two double layer coatings (345 nm and 350 nm) is smaller than the thickness of the single layer (400 nm). The reduction of the total coating thickness can be an argument in favor of a double-layer structure to reduce the internal strain and prevent peeling.

Fig. 4.8 shows three examples of double-layer coatings. The coating in Fig. 4.8 a) was designed to be centered around  $3.1 \mu\text{m}$  wavelength with a reflectivity of 0.01. The measurement shows a blue-shift of the center wavelength and an increase in the reflectivity. The shift is attributed to a reduced  $\text{Al}_2\text{O}_3$  thickness, where a too thin Ge layer accounts for the increased overall reflectivity. Fig. 4.8 b) shows an AR coating for a center wavelength of  $3.3 \mu\text{m}$ . Even though the general agreement of the simulation and measurement is good, the measurement exhibits a broader bandwidth than the simulation. For this specific coating, a final 30 nm thick  $\text{Al}_2\text{O}_3$  layer was added as a protection layer. Due to the short wavelength regime, that thin layer acted as a third layer, broadening the bandwidth and effectively creating a three-layer coating. Fig. 4.8 c) shows a third ex-

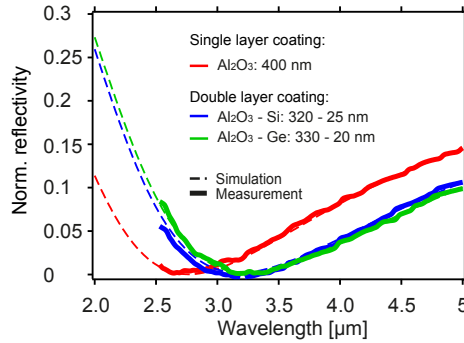


**Figure 4.7:** Simulation (dashed lines) and measurement (straight lines) of a single-layer  $\text{Al}_2\text{O}_3$  coating and two double-layer coatings ( $\text{Al}_2\text{O}_3$ -Ge and  $\text{Al}_2\text{O}_3$ -Si).

ample of a double-layer AR coating. It shows a good agreement of the simulation and measurement.

For truly broadband AR coatings, three or more layers are needed. The third layer (or the third and fourth layer together) adds a second coating on top of the first layer pair, with an offset center wavelength as shown in Fig. 4.6 c). The overlap of both coatings constitutes a broad bandwidth coating and the bandwidth can be tuned by changing the offset of the two effective coatings, i.e. the first and second layer pair.

Some examples of three layer AR coatings are shown in Fig. 4.9. Fig. 4.9 a) shows an  $\text{Al}_2\text{O}_3$  based coating which was simulated for wavelengths between 5.4 and 7.8  $\mu\text{m}$ . As can be seen in the graph, the real reflectivity is considerably higher on the long wavelength side. This can partially be attributed to the increasing absorption coefficient of  $\text{Al}_2\text{O}_3$  for wavelengths longer than 6  $\mu\text{m}$ , and partially to the too thin  $\text{Al}_2\text{O}_3$  layers. As visualized in Fig. 3.6, the geometric tooling factor for  $\text{Al}_2\text{O}_3$  is subject to change and strongly depends on the material surface, i.e. the position of the grains within the crucible. Thus even calibrating the thickness is no absolute guarantee for high accuracy in thicknesses.

Fig. 4.9 shows a coating in a similar wavelength range, but based on  $\text{YF}_3$  ( $\text{YF}_3$ -Ge- $\text{YF}_3$ : 398 - 152 - 1790 nm). Here, the agreement between sim-

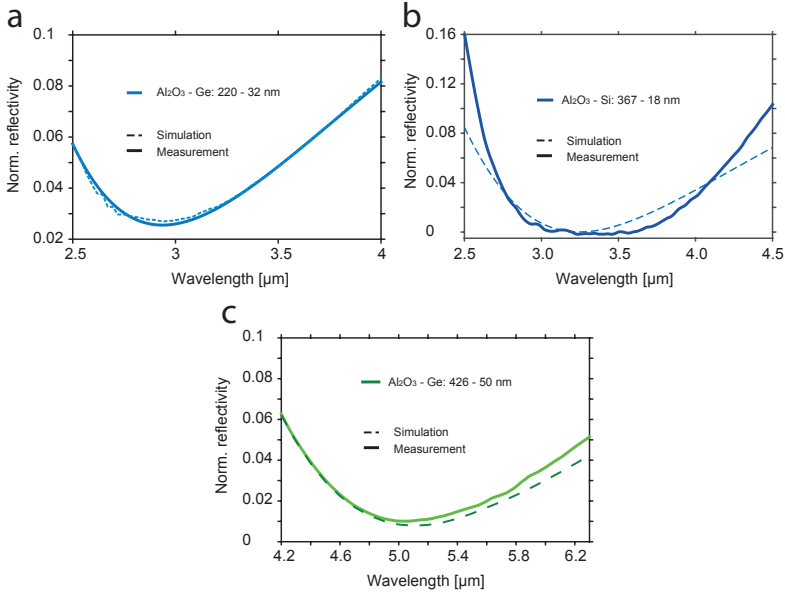


**Figure 4.8:** Two-layer anti-reflection coatings: **a)** Al<sub>2</sub>O<sub>3</sub>-Ge coating for epi-down mounted lasers with a center frequency of 3.1 μm. **b)** Alternative AR coating for wavelengths around 3.3 μm. The measurement shows a broader bandwidth than the simulation due to a 30 nm Al<sub>2</sub>O<sub>3</sub> passivation layer that acted as a third layer in the coating, effectively giving a three-layer coating. **c)** AR optimized for low reflectivities around 5.2 μm wavelength. All coatings show a good agreement between simulation and measurement.

ulation and measurement is very good. As the water absorption at 6 μm was not within the range of interest, no passivation layer was applied as a last layer of the coating, and the humidity absorbed by the YF<sub>3</sub> is visible in the H<sub>2</sub>O absorption at 6 μm. The coating itself shows the W-shape profile of three- and four-layer coatings. This W-shape emphasizes the compositorial nature of multilayer coatings from individual single wavelength coatings, consisting of one or two layers.

Fig. 4.9 b) shows an example of a three layer coating optimized for 3.1 to 3.8 μm wavelength. The sequence of Al<sub>2</sub>O<sub>3</sub>-Si-Al<sub>2</sub>O<sub>3</sub> (948 nm - 106 nm - 590 nm) has a reflectivity lower than 1 % from 2.9 to 3.8 μm. In contrast to the latter YF<sub>3</sub> based coating, the two reflectivity dips can't be distinguished due to the proximity of the two minima. This coating was applied to lasers that were tuned in an external cavity setup and published [76].

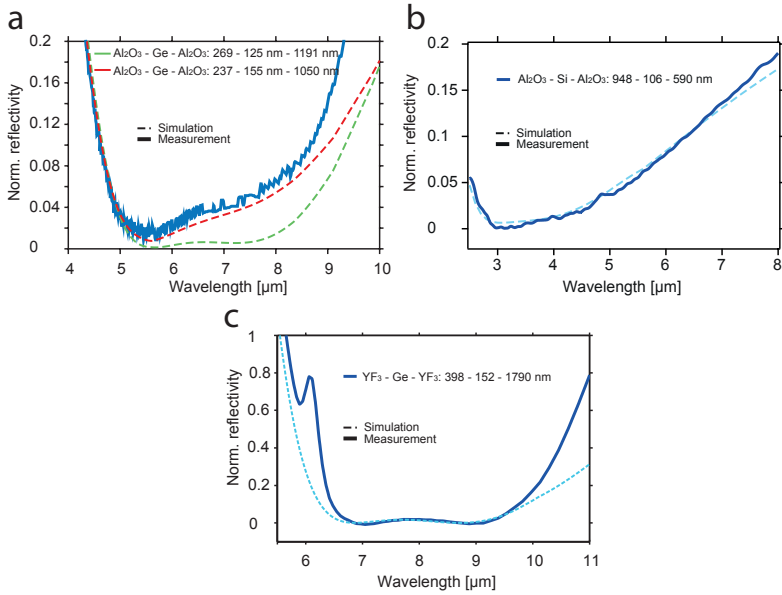


**Figure 4.9:** Three layer anti-reflection coatings: **a)** Coating optimized for wavelengths from 5.4  $\mu\text{m}$  to 7.8  $\mu\text{m}$ . The  $\text{Al}_2\text{O}_3$  thickness was underestimated and led to the increased reflectivity towards the longer wavelengths.  $\text{Al}_2\text{O}_3$  starts absorbing for wavelengths larger than 6  $\mu\text{m}$  and thus additionally increased the reflectivity. A more suited material would have been  $\text{YF}_3$ . **b)** Simulation (dashed line) and measurement (straight line) of a  $\text{Al}_2\text{O}_3$ -Si- $\text{Al}_2\text{O}_3$  (948 nm - 106 nm - 590 nm) AR coating optimized for the range of 3 - 4  $\mu\text{m}$ . **c)**  $\text{YF}_3$  based coating with good agreement with the simulation. Since no passivation layer was applied, the humidity absorbed by the  $\text{YF}_3$  is visible in the  $\text{H}_2\text{O}$  absorption at 6  $\mu\text{m}$ . The coating nicely shows the W-shape of three- or four-layer coatings.

### Octave spanning coating

An ultra broadband laser design with five active region stacks was developed and showed great promise for octave spanning operation. Since the gain was not perfectly flat a good AR coating over the whole lasing bandwidth was required to operate it successfully in external cavity. To cover all five lasing colors a multi-layer coating consisting of five low-/high-index layer pairs was developed, one pair per lasing color. We used  $\text{YF}_3$  and Ge as low- and high-index materials, respectively. The sequence and thicknesses are  $\text{YF}_3$  (160 nm) - Ge (170 nm) -  $\text{YF}_3$  (360 nm) - Ge (70 nm) -  $\text{YF}_3$  (230 nm) - Ge (38 nm) -  $\text{YF}_3$  (10 nm) - Ge (20 nm) -  $\text{YF}_3$  (1080 nm) - Ge (15 nm) and the simulation and measurement are shown in Fig. 4.10. The

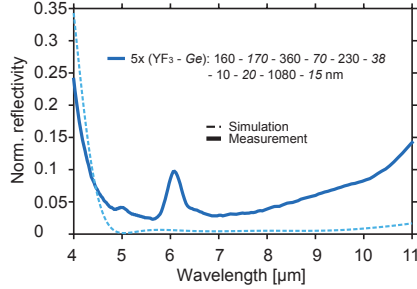


**Figure 4.10:** Ten layer coating for the range from 5 to 10  $\mu\text{m}$  wavelength. The difference between the simulation and the measurement can be attributed to the increased absorption of the  $\text{Al}_2\text{O}_3$  from 6  $\mu\text{m}$  wavelength and longer.

measurement shows a large discrepancy from the flat and low reflectivity simulation. This is partially attributed to the thin layers of the coating. Thin layers have a much smaller tolerance for errors in the thickness. And since thin layers are the most difficult to deposit accurately with the evaporator used, a large error could have been introduced in this manner. From the high reflectivities at the long wavelength end one can deduce that the low index material thickness was too small. So a too high tooling factor was assumed for the  $\text{YF}_3$  deposition, leading to too thin layers.

#### 4.4.3 Coatings for mode selection

For multi-species trace gas analysis a single mode laser with lasing modes at two distinct wavelengths was designed [94]. A stacked double color active region, centered around  $2180\text{ cm}^{-1}$  ( $4.6\text{ }\mu\text{m}$ ) and  $2280\text{ cm}^{-1}$  ( $4.4\text{ }\mu\text{m}$ ), was processed into twin DFB lasers. That is, the laser has a front section DFB grating for the first target wavelength and a back section DFB grating for the second target wavelength as visualized in Fig. 4.11 c). The front and back section lasers can be operated separately, but for some wavelengths parasitic modes turn on. To prevent the lasers from lasing on the other mode, a AR coating for the appropriate wavelength is applied to introduce losses for one of the lasing modes. Fig. 4.11 a) and b) show two examples of coatings applied to two laser designs with center wavelengths at  $4.4\text{ }\mu\text{m}$  and  $4.6\text{ }\mu\text{m}$  (Fig. 4.11 a)) and  $5.26\text{ }\mu\text{m}$  and  $6.25\text{ }\mu\text{m}$  (Fig. 4.11 b)).



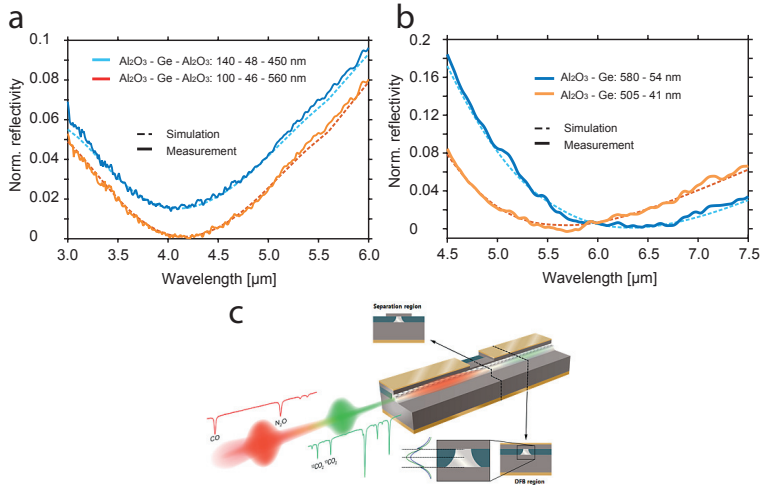


**Figure 4.11:** Simulation and measurement of AR coatings applied to twin DFB lasers: **a)** The center wavelengths for the two sections are  $4.4\ \mu\text{m}$  and  $4.6\ \mu\text{m}$ , respectively. **b)** Center wavelengths are  $5.26\ \mu\text{m}$  and  $6.25\ \mu\text{m}$ , respectively. **c)** SOURCE: Süess *et al.* [94]; visualization of the twin DFB laser structure. The front and back lasers can be operated individually or together. The coatings are applied to the facets to increase losses of the wavelength further from the facet to prevent parasitic modes.

#### 4.4.4 Fabry-Pérot cavity

In QCLs, designed to have a low group delay dispersion (GDD), comb operation can be achieved [106, 139] by a four-wave mixing process taking place in the gain medium itself [136]. To better understand the fundamental properties of such QCL comb devices and improve upon the spectroscopic applications, measurements of the frequency noise and the intrinsic linewidth is of great importance. In order to investigate the frequency noise, a high-finesse optical cavity is used to resolve the laser spectrum, acting as a frequency-to-amplitude converter. [135]

Such a study was done on QCLs based on the structure reported by Hugi *et al.* [106].

To create a self-made Fabry-Pérot cavity, a pair of high-reflectivity mirrors was used. The mirrors were coated with a dielectric HR coating based on YF<sub>3</sub> and Ge with Ti adhesion layers and a Al<sub>2</sub>O<sub>3</sub> passivation layer (2x

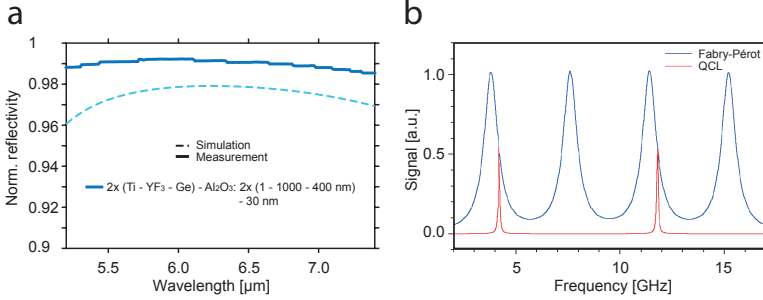


**Figure 4.12:** a) Simulation and measurement of a dielectric HR coating for mirrors of a self-made Fabry-Pérot cavity, acting as a frequency ruler to measure the frequency noise of a QCL comb. b) Courtesy of F. Cappelli; Fabry-Pérot cavity and QCL characteristics. The length of the FP cavity is  $l = 39$  mm, the free spectral range (FSR) = 3.8 GHz and the FWHM = 80 MHz.

(Ti - YF<sub>3</sub> - Ge) - Al<sub>2</sub>O<sub>3</sub>: 2x (1 - 1000 - 400 nm) - 30 nm). Fig. 4.12 a) shows values for the reflectivity of the mirrors of 98 %. Measuring the relevant characteristics of the cavity, i.e. the free spectral range (FSR) = 3.8 GHz and FWHM = 80 MHz at a cavity length of  $l = 39$  mm, cf. Fig. 4.12 b), the finesse of the cavity can be calculated to be

$$\mathcal{F} = \frac{\text{FSR}}{\text{FWHM}} = \frac{3.8 \text{ GHz}}{80 \text{ MHz}} = 47.5; \quad (4.20)$$

which can be approximated for reflectivities  $R \geq 0.5$  as follows:

$$\mathcal{F} = \frac{\text{FSR}}{\text{FWHM}} \approx \frac{\pi\sqrt{R}}{1-R}. \quad (4.21)$$

Extracting the reflectivity  $R$  thus gives mirror reflectivities of  $R = 0.94$ . The discrepancy between the transmission measurement and the cavity calculation can partially be explained by the absorption of the Titanium adhesion layers, and partially by the low signal when measuring a HR coating in transmission mode and its uncertainty.

#### 4.4.5 Dispersion compensation coatings

As mentioned in section 4.2.3, we expect to improve the range of the QCL's frequency comb regime by reducing the dispersion through a GTI mirror on the back facet of a QCL frequency comb. The first design was a simple alternating sequence of Al<sub>2</sub>O<sub>3</sub> and SiO<sub>2</sub> finished with a Au layer. The left

first GTI structure		revised GTI structure	
Material	Thickness	Material	Thickness
$\text{Al}_2\text{O}_3$	250 nm	$\text{Al}_2\text{O}_3$	511 nm
$\text{SiO}_2$	250 nm	$\text{SiO}_2$	102 nm
$\text{Al}_2\text{O}_3$	250 nm	$\text{Al}_2\text{O}_3$	511 nm
$\text{SiO}_2$	250 nm	$\text{SiO}_2$	102 nm
$\text{Al}_2\text{O}_3$	250 nm	$\text{Al}_2\text{O}_3$	511 nm
$\text{SiO}_2$	250 nm	$\text{SiO}_2$	102 nm
$\text{Al}_2\text{O}_3$	250 nm	$\text{Al}_2\text{O}_3$	511 nm
$\text{SiO}_2$	250 nm	$\text{SiO}_2$	102 nm
$\text{Al}_2\text{O}_3$	250 nm	$\text{Al}_2\text{O}_3$	511 nm
$\text{SiO}_2$	250 nm	$\text{SiO}_2$	102 nm
$\text{Al}_2\text{O}_3$	150 nm	$\text{Al}_2\text{O}_3$	154 nm
Au	150 nm	Au	154 nm

**Table 4.1:** Left: first GTI mirror structure, introducing positive GDD due to a shift in frequency. Right: revised GTI mirror structure with adapted layer thicknesses to correct for the correct center frequency.

columns of Table 4.1 show the layer sequence and thicknesses in question. This first GTI layer was evaporated onto an InP reference sample and measured in the reflection setup. Fig. 4.13 a) shows the measurement of the reference sample (purple) together with the measurement of a standard metallic HR coating (green). The standard HR coating introduces a constant negative dispersion attributed to thickness of the insulating  $\text{Al}_2\text{O}_3$  layer. The first GTI design, however, resulted in a positive GDD, counteracting the desired compensating effect of the GTI mirror. After careful evaluation of the first GTI mirror, it was found that the layer sequence shifted the GDD minimum to higher frequencies and thus the layer thicknesses were adapted to the sequence shown in the right hand side columns of Table 4.1. A coating fabricated according to the revised layer sequence yielded a negative GDD as planned, shown in Fig. 4.13 a), and the center frequency corresponds well to the simulation. The more pronounced minimum in the measurement compared to the simulation is believed to stem from the  $\text{SiO}_2$  absorption in this wavelength range, which enhances the effect. The revised layer sequence was applied to QCLs operated as frequency combs and it was shown by Villares *et al.* [137] that the GTI mirror coatings dramatically improved the comb operation regime as expected.

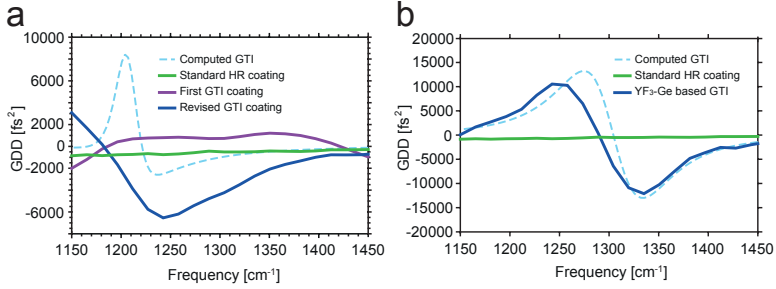


**Figure 4.13:** GTI coatings. **a)** Simulation (dashed, light blue) and measurement of the first GTI mirror structure (purple) and the revised structure (dark blue) as described in Table 4.1. The measurement of a standard metallic HR coating is shown alongside (green). **b)** Simulation (dashed, light blue) and measurement (dark blue) of the  $\text{YF}_3$  - Ge based GTI structure and the standard metallic HR coating (green).

Further investigations showed that using  $\text{YF}_3$ , the interference observed with  $\text{SiO}_2$  can be avoided and GTI mirrors based on  $\text{YF}_3$  and Ge showed a good overlap of simulation and measurement as shown in Fig. 4.13 b).

---

# External Cavity and experimental setup

In this chapter, the mechanism of a QCL based grating tuned external cavity setup are discussed. It will give an overview on the different available setups and their main components as well as some background on the theory of the tuning mechanism behind it.

As mentioned in chapter 1, to detect multiple gas lines, light sources with the ability to tune over large parts of the mid-infrared are desirable. This can be achieved using a grating coupled external cavity (EC) and has first been demonstrated by Luo *et al.* in 2001 [84] at cryogenic temperatures. The first room temperature EC-QCL tuning was shown only one year later by Totschnig *et al.* at a wavelength of  $10.4\ \mu\text{m}$  [140]. In the same year, Luo *et al.* combined grating and temperature tuning and showed the suitability of such a system for spectroscopic applications by measuring the water absorption at  $5.083\ \mu\text{m}$  [141]. After the introduction of a new broadband gain active region design called bound-to-continuum [108], works by Maulini *et al.* [85, 86, 142], Wittmann *et al.* [143] and Hugi *et al.* [73, 105] focused on increasing the tuning range of EC QCLs. Thermoelectric stabilization and mode-hop free tuning with temperature fine tuning was shown [59, 87] as well as continuous wave tuning [144].

For spectroscopic applications, not only the tuning range is of critical importance, but also the tuning speed, the time in which a full spectral scan is completed. Fast tuning ranges allow for constant monitoring, for example of production processes without the need to take random sam-

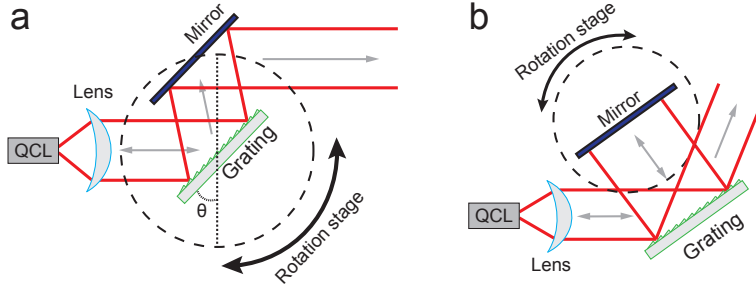


**Figure 5.1:** EC-QCL configurations: **a)** Littrow front extraction configuration. The first order diffracted beam is coupled back into the QCL, the 0th order is coupled out by a mirror. **b)** Littmann-Metcalf configuration: The first order diffracted beam is reflected off a mirror and diffracted a second time and then coupled back into the laser. The 0th order is coupled out.

ples [145]. In 2010, Tsai and Wysocki reported a fast wavelength scanning of an EC based on a modified Littrow configuration, with scan rates of up to 5 kHz and tuning ranges up to  $7 \text{ cm}^{-1}$  [146]. The fast scanning was achieved with an incorporated piezo-driven fast tilt mirror. A scan rate of  $\approx 2 \text{ cm}^{-1}/\mu\text{s}$  was achieved by Hugger *et al.* by replacing the piezo-driven mirror by a fast scanning micro-optic-electro-mechanic system (MOEMS) mirror [147]. Using an acousto-optic modulator (AOM), Lyakh *et al.* presented a tuning range of  $\sim 150 \text{ cm}^{-1}$  with a switching time of less than  $1 \mu\text{s}$  between two wavelengths [148]. Ostendorf *et al.* recently presented a fast tuning of more than  $300 \text{ cm}^{-1}$  using a resonantly driven MOEMS scanner with an integrated diffraction grating, with a resonance frequency of 1 kHz [145]. This scanning frequency allows for two full wavelength scans in 1 ms. In addition to being very fast, these systems are also very compact ( $50 \times 40 \times 52 \text{ mm}$ ), i.e. so called miniaturized EC setups [149] and thus very well suited for a wide range of sensing applications [150].

## 5.1 Experimental setup

This section will give an overview on the setup used to conduct all external cavity measurements presented in this work.

### 5.1.1 External cavity configuration

Grating coupled EC setups allow us to force a free running semiconductor laser to lase on a single mode that is tunable over a substantial part of its gain curve. Such EC setups consist of three main components: the gain medium, in our case the QCL, a collimating lens and a grating acting as the filter element for the frequency [151].

The QCL, as the gain medium, limits the tuning range to part of the bandwidth of the QCL gain curve. Hence, the importance of the active region design becomes apparent. However, here we will focus on the optical elements while the gain medium will be discussed in detail in chapters 6 and 7.

The two most widely used grating-coupled EC setups are the Littrow [81, 82] and Littman-Metcalf [77] setups, illustrated in Figure 5.1, and have both been used with QCLs as gain medium [141].

The Littrow configuration, Fig. 5.1 a), comprises a grating that is mounted on a rotation stage. The wavelength is tuned by changing the angle of incidence of the laser beam on the grating, which is done by rotating the grating. A mirror is mounted in parallel to the grating on the rotation stage and is used to couple out the light from the external cavity. The laser beam impinges on the grating and the first order diffracted beam is coupled back into the gain region directly while the zeroth order of the mirror is coupled out by a mirror. This setup has the advantage of requiring only two optical elements, the lens and the grating, simplifying the alignment, and showing strong feedback due to the single pass on the grating.

The Littmann-Metcalf configuration, Fig. 5.1 b), consists of a grating, mounted at a fixed angle with respect to the laser source, and a mirror that is mounted on a rotation stage and acts as the wavelength selection element. The laser beam is collimated by the lens, diffracted by the grating and then reflected by the mirror. The first order diffracted beam impinges on the mirror at normal incidence and is reflected back onto the grating, where it is diffracted a second time and coupled back into the active region. The zeroth order beam is coupled out via the mirror, which is used for extraction. The double-pass through the grating increases the wavelength

selectivity but reduces the feedback strength compared to a single-pass setup.

Alternative setups are Littrow configurations with a back facet extraction, resulting in higher output powers but slightly smaller tuning ranges [96]. Since the aim was to maximize the tuning range, the Littrow configuration as shown in Fig. 5.1 a) was chosen for this work.

### Optical components

For a broad EC-QCL tuning, it is of utmost importance to work with suitable lenses and gratings for the respective wavelength ranges. For this work, mostly two aspheric molded collimating lenses (Infrared Collimating Lenses, LightPath Technologies) were used. The IR glass used is BD-2, which is a  $\text{Ge}_{28}\text{Sb}_{12}\text{Se}_{60}$  compound.

For the wavelength range from 3 to 5  $\mu\text{m}$ , a lens with a design wavelength of 2.5  $\mu\text{m}$  and an AR coating optimized for 3 – 5  $\mu\text{m}$  was used. The outer diameter was  $d = 6.5$  mm, the numerical aperture  $\text{NA} = 0.56$ , the effective focal length  $\text{EFL} = 4.0$  mm and the working distance  $\text{WD} = 3.05$  mm. The lens for wavelengths from 6 to 10  $\mu\text{m}$  had a design wavelength of 7  $\mu\text{m}$  and an AR coating centered around 9 – 10  $\mu\text{m}$ . The outer diameter was 5.5 mm,  $\text{NA} = 0.85$ ,  $\text{EFL} = 1.873$  mm and  $\text{WD} = 0.723$  mm. The average reflectance coefficient for both lenses was  $R_{\text{avg}} < 0.6$  % and the absorption was  $\sim 0.01$   $\text{cm}^{-1}$ .

The intermediate wavelength range from 4 to 7  $\mu\text{m}$  was difficult to cover, since no lens for this range was commercially available that would fit the mechanical and geometrical requirements of the setup. Thus a combination of a long wavelength lens and a short wavelength AR coating was used in addition to the two aforementioned lenses.

All used gratings were 12.5 mm  $\times$  12.5 mm in size and optimized for different wavelength ranges, similar to the lenses. The grating for wavelengths between 3 and 5  $\mu\text{m}$  had a blazing for 5.4  $\mu\text{m}$  and 300 grooves per millimeter ( $g/\text{mm}$ ), i.e a line spacing of  $d = 3.33$   $\mu\text{m}$ . The range from 5 to 7  $\mu\text{m}$  wavelength was covered by a grating with a 5.4  $\mu\text{m}$  blaze and 150  $g/\text{mm}$  ( $d = 6.67$   $\mu\text{m}$ ). The range from 7 to 10  $\mu\text{m}$  was covered by a grating with a blaze at 10.6  $\mu\text{m}$  and 150  $g/\text{mm}$  ( $d = 6.67$   $\mu\text{m}$ ). The grating



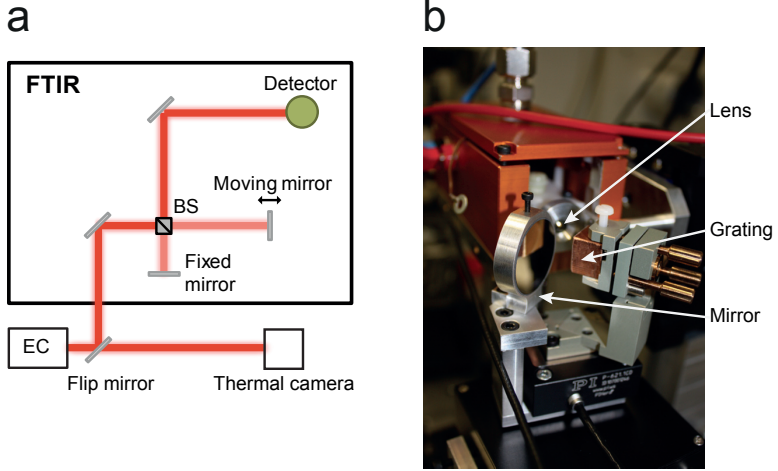


**Figure 5.2:** **a)** Schematic view of the measurement setup. The extracted light from the EC setup is directed into a FTIR (Nicolet 800) and measured with an Nitrogen cooled MCT detector. To align the lens, the beam was observed with a thermal camera. **b)** Adapted from A. Hugl [96]; front view of the EC setup with the collimating lens, the grating and the outcoupling mirror.

acts as a wavelength filter and in the case of the front-extraction Littrow configuration the wavelength depends on the period  $d$  and of the grating and the incident angle  $\Theta$  and can be expressed as [152]

$$\lambda = 2d \sin(\Theta). \quad (5.1)$$

### 5.1.2 Measurement setup

A series of steps was necessary to characterize a QCL in the EC setup. Depending on the wavelength of the QCL, the appropriate lens and grating had to be selected and mounted into their respective holders. The lens was mounted onto a piezo-electric xyz-stage (PI, Physikinstrumente) which allowed us to position the lens with an accuracy of several tens of micrometers. To enable the absolute positioning of the lens, the x, y and z axes were initialized and calibrated for every new laser inside the EC setup. The grating was mounted on top of the rotation stage and adjusted to the same height as the lens to keep the beam in the same plane. Since the diffracted laser beam has to be coupled back into the active region, it

is very important to position the grating in a perfectly vertical position, in order to keep the diffracted beam in the same optical plane as the rest of the setup. This alignment was done with the help of a red laser pointer with a beam parallel to the surface of the optical table. The beam was guided onto the rotating grating and the grating tilt adjusted until all the diffracted beams were parallel to the incident beam.

Once these preparations were finished, the collimating lens was roughly centered in front of the facet of the mounted QCL and positioned approximately one millimeter from the facet. To align the lens, the QCL was operated at 1 % duty cycle (100 ns, 100 kHz) and the beam shape observed with a thermal camera. The lens was then aligned until a parallel beam of constant diameter was obtained. Once the alignment of the lens was complete, the beam was directed into a FTIR (Nicolet 800) and measured with the internal Nitrogen cooled MCT detector. A schematic of the measurement setup is shown in Fig. 5.2 a). To simplify the positioning of the grating in front of the lens, the angle was set to a wavelength corresponding to the center of the lasing spectrum. Once the grating was positioned, the fine alignment of the lens and the grating would allow to explore the tuning ability of the device under test. Fig. 5.2 b) shows the front view of the EC setup with the lens, the grating and the outcoupling mirror.

## 5.2 Theory

### 5.2.1 Rate equations

In comparison to the rate equations for a quantum cascade laser as shown in section 2.2.1, the rate equations for an EC-QCL have to include the external cavity, or external resonator. The optical flux has to be divided into two separate flux densities  $S_{FP}$  and  $S_{EC}$ , describing the total photon flux per unit active region width ( $\text{cm}^{-1}\text{s}^{-1}$ ) in the chip, i.e. the Fabry-Pérot (FP) modes, and in the external cavity, i.e. EC modes. Additionally, the longer round trip time of the photons in the EC has to be taken into account and can be implemented by multiplying their speed by  $\rho_{cav}^{-1} = (1 + \frac{L}{nl})^{-1}$ , where  $\rho_{cav}$  is the ratio of the optical path lengths of the two cavities.  $L$  the distance between the front facet of the laser to the external

grating,  $l$  is the laser chip length and  $n$  the refractive index of the active region. The total losses have to be addressed for the chip modes and the EC modes separately as well, introducing  $\alpha_{\text{tot}}^{\text{FP}}$  and  $\alpha_{\text{tot}}^{\text{EC}}$ . Finally, the gain cross section per period ( $\text{cm}^{-1}$ ) of the EC depends on the gain profile, i.e.  $g_{\text{EC}}$  reflects the gain cross section at a wavelength  $\lambda$  within the gain curve of the active region  $g_c(\lambda)$ , see equation 2.5, whereas  $g_{\text{FP}}$ , the gain cross section of the FP chip modes, is the gain cross section per period at the maximum of the gain curve  $g_c(\lambda_{\text{max}})$ . The rate equations for the EC can then be written as [152]

$$\frac{dn_3}{dt} = \frac{J}{e} - \frac{n_3}{\tau_3} - (S_{\text{FP}}g_{\text{FP}} + S_{\text{EC}}g_{\text{EC}})(n_3 - n_2) \quad (5.2)$$

$$\frac{dn_2}{dt} = \frac{n_3}{\tau_{32}} - \frac{n_2 - n_2^{\text{therm}}}{\tau_2} + (S_{\text{FP}}g_{\text{FP}} + S_{\text{EC}}g_{\text{EC}})(n_3 - n_2) \quad (5.3)$$

$$\frac{dS_{\text{FP}}}{dt} = \frac{c}{n_{\text{refr}}} \left( [N_{\text{P}}g_{\text{FP}}(n_3 - n_2) - \alpha_{\text{tot}}^{\text{FP}}] S_{\text{FP}} + \beta \frac{n_3}{\tau_{\text{sp}}} \right) \quad (5.4)$$

$$\frac{dS_{\text{EC}}}{dt} = \frac{c}{\rho_{\text{cav}}} n_{\text{refr}} \left( [N_{\text{P}}g_{\text{EC}}(n_3 - n_2) - \alpha_{\text{tot}}^{\text{EC}}] S_{\text{EC}} + \beta \frac{n_3}{\tau_{\text{sp}}} \right) \quad (5.5)$$

where  $n_i$  are the sheet densities per period ( $\text{cm}^{-2}$ ),  $\tau_i$  are the total lifetimes of the states,  $n_2^{\text{therm}}$  the thermal population of level 2,  $\tau_{32}$  the non-radiative relaxation time from the upper to the lower level,  $\tau_{\text{sp}}$  is the spontaneous emission lifetime and  $\beta$  is the fraction of spontaneous light emitted into the lasing mode.  $\alpha_{\text{tot}}^{\text{FP}}$  are the total FP-chip losses, consisting of the waveguide losses  $\alpha_{\text{wg}}$  and the mirror losses of the AR coated QCL. The total losses of the EC are

$$\alpha_{\text{tot}}^{\text{EC}} = \alpha_{\text{wg}} + \frac{1}{2L} \ln \frac{1}{R_{\text{EC}}} R_{\text{HR}}, \quad (5.6)$$

with  $R_{\text{HR}}$  being the reflectivity of the HR coated back facet and the EC resonator reflectivity defined as

$$R_{\text{EC}} = (r_1 + \eta T_1 T_L \sqrt{R_{\text{G}}})^2, \quad (5.7)$$

where  $r_1$  and  $T_1$  are the front facet amplitude reflectance and transmittance, respectively,  $T_L$  the transmittance of the lens,  $R_{\text{G}}$  the grating reflectance and  $\eta$  the coupling of the EC reflected wave into the waveguide mode.

### 5.2.2 Tuning range

The coarse tuning range can be estimated by considering the steady-state solutions of the two rate equations describing the time evolution of the photon flux of the electronic modes  $S_{EC}$  in dependance of the electronic populations of the upper and lower laser states  $n_3, n_2$ , as was done by Maulini [152] and Hugi *et al.* [73]. The only solution with a non-zero photon flux for the EC mode requires that the following condition is fulfilled:

$$\frac{g_{EC}}{g_{FP}} \geq \frac{\alpha_{tot}^{EC}}{\alpha_{tot}^{FP}}. \quad (5.8)$$

$g_{EC}$  and  $\alpha_{tot}^{EC}$  are the gain and total losses of the external cavity resonator and  $g_{FP}$  and  $\alpha_{tot}^{FP}$  the gain and total losses of the Fabry-Pérot chip modes [95]. To increase the tuning range of an EC-QCL the EC gain  $g_{EC}$  has to be increased compared to FP  $g_{FP}$ . This can be achieved by a broadband active region design, as discussed in chapters 2 and 6.

Secondly, the right-hand-side of eq. 5.8, the ratio of the total FP chip mode losses and the total EC mode losses, has to be minimized. The total losses of the FP chip and the EC setup are given by

$$\alpha_{tot}^{FP} = \alpha_{wg} + \alpha_m^{FP} \quad (5.9)$$

$$\alpha_{tot}^{EC} = \alpha_{wg} + \alpha_m^{EC}, \quad (5.10)$$

where  $\alpha_{wg}$  are the waveguide losses and

$$\alpha_m^{FP,EC} = \frac{1}{2l} \ln \left( \frac{1}{R_{1,EC} R_2} \right) \quad (5.11)$$

the mirror losses with  $l$  being the QCL length,  $R_{1,2}$  the front and back facet mirror reflectivities and  $R_{EC}$  the total EC reflection given by eq. 5.7.

The total derivative of  $\frac{\alpha_{tot}^{EC}}{\alpha_{tot}^{FP}}$  is

$$d \left( \frac{\alpha_{tot}^{EC}}{\alpha_{tot}^{FP}} \right) = \frac{1}{\alpha_{wg} + \alpha_m^{FP}} d(\alpha_m^{EC}) + \frac{\alpha_m^{FP} - \alpha_m^{EC}}{(\alpha_{wg} + \alpha_m^{FP})^2} d(\alpha_{wg}) - \frac{\alpha_{wg} + \alpha_m^{EC}}{(\alpha_{wg} + \alpha_m^{FP})^2} d(\alpha_m^{FP}) \quad (5.12)$$

and shows the importance of the waveguide losses in the EC tuning. Decreasing the waveguide losses not only directly reduces the value of the second term in eq. 5.12, but also helps increase the FP losses in the third

term, as well as reduce the EC losses in the first term. Low waveguide losses ( $\sim 2\text{cm}^{-1}$ ) additionally lower the dependance of the tuning on the device length  $l$ . A. Hugi showed that a back facet HR coating helps to increase the tuning range even though at first glance, the effect on the FP chip losses and EC losses should be equal [96]. The third term of eq. 5.12 again stresses the importance of front facet AR coatings in EC tuning. To minimize the ratio, the FP mirror losses have to be increased, which can be done by efficient AR coatings applied on the front facet, effectively removing the chip cavity.

When a QCL is operated in pulsed mode in EC, the FP and EC modes undergo mode competition due to the different roundtrip times of the FP chip cavity and the external cavity. This dynamic behavior can be studied with the rate equation 5.5 and has been published by Maulini *et al.* in 2004 [85]. First, the FP chip modes begin to lase and the photon flux increases until gain clamping sets in and the photon flux saturates and stabilizes. The EC photon flux still continues to grow and reduces the population inversion and eventually, the FP gain can't compensate for the losses anymore and the FP modes will vanish.

### Tuning limits

In EC, the tuning limit of the QCL can be set by two different mechanisms. Fig. 5.3 shows a schematic representation of the tuning process and two measurements to illustrate the point.

When a QCL is operated in EC, the threshold gain has been influenced already by the waveguide losses, i.e. the processing, and the mirror losses, i.e. the front facet AR coating. Ideally, the QCL does not reach threshold when operated as a free running device. When operated in EC though, the grating will provide a filtered feedback which will allow a selective decrease of the losses for a certain wavelength and the QCL will reach threshold. By changing the optical feedback, with changing the incident angle on the grating, the lasing wavelength can be tuned.

Panel 5 in Fig. 5.3 a) shows the first tuning limiting situation, where the selective feedback still accesses an EC mode, but simultaneously the peak gain reaches threshold. In this situation, both an EC and FP mode

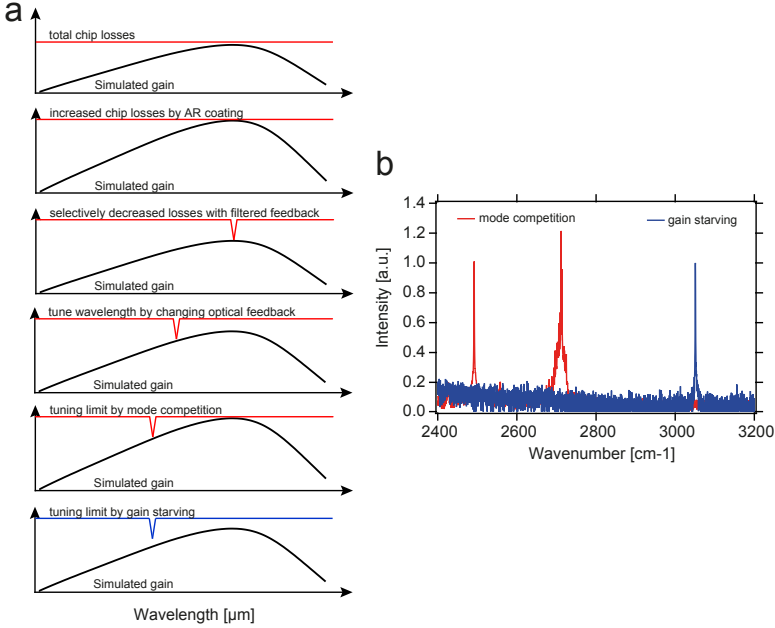


**Figure 5.3:** **a)** Schematic representation of the EC tuning principle and the tuning limits. The limit can be given by mode competition with FP modes (fifth panel) or by gain starving (sixth panel). **b)** Tuning extremes reached with a 4.5 mm long device in pulsed mode (1 % duty cycle). The red curve shows the tuning limit by mode competition, where FP modes are dominating. The blue curve shows the limit by gain starving, when the mode vanishes without any FP modes appearing.

is visible in the spectrum, as is shown in Fig. 5.3 b) by the red spectrum. This limit can be due to the fact, that the AR coating of the front facet didn't reduce the reflectivity enough to suppress FP modes. Hence, an AR coating with an overall lower reflectivity, or a broader bandwidth could increase the tuning range.

Panel 6 in Fig. 5.3 a) shows the second limiting mechanism, in which no FP mode appears, but the EC mode decreases until it vanishes. This is called gain starving and comes from a lack of gain that can be accessed by the filtered feedback. Here, the AR coating fully suppresses the FP modes, but the gain is not high enough to be accessed by the optical feedback. The blue spectrum in Fig. 5.3 b) shows such a situation.

Coating and design mainly determine the tunability of a laser, but it is possible to influence the tuning for example by temperature. The tuning condition 5.8 shows that the tuning range itself does not depend on the temperature. Hence, no change in the tuning range by lowering the temperature should be expected. This is true for the case where we have gain competition and the FP-chip modes limit the tuning range. But in the case of gain starving the temperature plays an important role. As known, the Fermi-level of the electrons depends strongly on the temperature. Thus high temperatures lead to high Fermi-levels making it difficult to achieve population inversion due to reabsorption into the lower laser states. Lowering the temperature also lowers the Fermi-level and consequently it becomes easier to achieve and maintain population inversion. The gain curve behaves accordingly and broadens with decreasing temperature (cf. Fig. 5.3).





## Chapter 6

---

# Broadband QCL in the 3 - 4 $\mu\text{m}$ range

This chapter will outline the design of an active region centered around 3.8  $\mu\text{m}$  wavelength based on the design at 3.3  $\mu\text{m}$  by Bismuto *et al.* [51]. The active regions were combined into a broadband heterostructure that was tested in external cavity.

The chapter will go through some of the details concerning material systems and strain compensation in short wavelength designs. The different designs will be labeled with their growth numbers, which is composed of the abbreviation **EV** and a four-digit number, for example EV1234.

### 6.1 Introduction

The 3 - 5  $\mu\text{m}$  spectral region, also known as the first atmospheric window, is of importance since the fundamental C-H, N-H and O-H stretching modes have strong resonances in this region [1, 2], for example green house gases such as Methane, Formaldehyde, Carbomonoxyde and Nitrous Oxide. Hence, these so called fingerprint regions are particularly interesting for applications like pollution control, breath analysis or detection of water contaminants.

Over the last decades, interband cascade lasers (ICLs) have reached very good performance in the spectral range around 3  $\mu\text{m}$ , such as room temperature continuous wave operation [153]. They show low threshold current densities, low power consumption and high output power

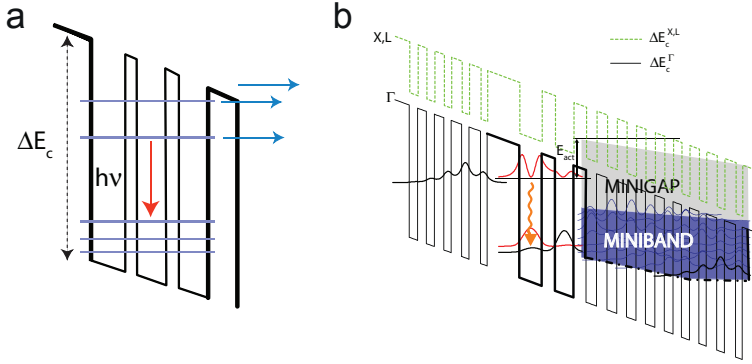


**Figure 6.1:** SOURCE: Faist [95]. **a)** Schematic bandstructure where possible escape routes for electrons into the continuum are indicated by the blue arrows. **b)** Conduction band diagram including the X and L valleys (dashed, green).

[47]. Compared to QCLs however, ICLs show relatively low slope efficiencies and are based on a AlSb/GaAs/InAs/AlInSb material system on GaSb substrate, making the growth challenging and a crucial parameter of optimization. QCLs on the other hand are very promising lasers due to their unique possibility to tailor the emission frequency as mentioned in chapter 2. In recent years, single mode QCLs operating in pulsed and continuous wave mode close to 3  $\mu\text{m}$  have been presented [51, 154, 104, 52, 53, 54]. Room temperature output powers as high as 900 mW in pulsed and 500 mW in continuous wave were reported [53, 54]. Initially good results for QCLs in output power and threshold current densities were achieved for Sb-containing materials [155]. But using more prevalent materials brings the advantage of a more mature technology.

However, to detect multiple gas lines, high tuning ability of light sources in the entire mid-infrared is desirable and a broad gain structure is a prerequisite for a broadband tuning.

## 6.2 Material systems

For QCLs the accessible photon transition energy is limited on the high energy side by the conduction band discontinuity  $\Delta E_c$  between the semiconductor materials of the wells and barriers. This limitation arises due

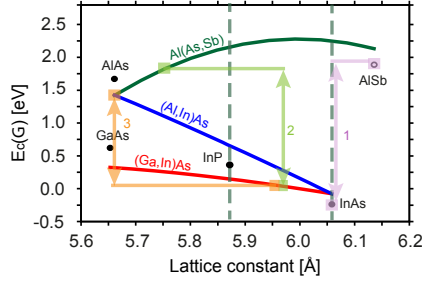


**Figure 6.2:** SOURCE: Vandewalle [95] [156] and Vurgaftman *et al.* [157]. *Gamma*-valley conduction band edges for the three most used material systems for short wavelength QCLs. (1) InAs/AlSb grown on InAs. (2) Strain compensated InGaAs/AlAsSb and (3) strain compensated InGaAs/InAlAs considered to be pseudomorphically grown on InP.

to thermal escape of electrons from the upper laser state to the continuum of the  $\Gamma$  point or states in the lateral X and L valleys. The escape time of the electron into the continuum is exponential in temperature [95]

$$\tau_{\text{esc}}^{-1} = \tau_{\text{cont}}^{-1} \exp(-E_{\text{act}}/kT), \quad (6.1)$$

with an escape time into the continuum  $\tau_{\text{cont}}^{-1} \approx 100$  fs, estimated from the width of the typical continuum resonance. For good room temperature performance, a minimum energy offset between the band edge of the minigap and the upper laser state of  $E_{\text{act}} = 85$  meV is usually chosen, yielding an escape time of  $\tau_{\text{esc}} = 2.7$  ps [95].

For QCLs with wavelengths longer than  $5 - 6 \mu\text{m}$ , the standard lattice matched  $\text{In}_{0.53}\text{Ga}_{0.47}\text{As}/\text{Al}_{0.48}\text{In}_{0.52}\text{As}$  material system with a conduction band offset of  $\Delta E_c = 520$  meV is the most widely used [20]. For QCLs with short wavelengths however, other material systems with higher conduction band offsets have to be employed. Fig. 6.2 shows the  $\Gamma$ -valley conduction band edges of the main III-IV semiconductor materials. (2) is a strain compensated InGaAs/AlAsSb system and (3) a InGaAs/InAlAs system which both are considered to be grown pseudomorphically on InP, while the InAs/AlSb composition (1) is grown on InAs.

A good candidate for short wavelength lasers is the InAs/AlSb material system grown on InAs substrates due to its large conduction band discontinuity of  $\Delta E_c = 2.1$  eV. However, compared to InP based material systems,

this Sb containing system suffers from less favorable thermal conduction and from a difficult epitaxial growth. A very successful, Sb-free, material system is the strain compensated  $\text{Ga}_x\text{In}_{1-x}\text{As}/\text{Al}_y\text{In}_{1-y}\text{As}$  on InP, which can have conduction band discontinuities of  $\Delta E_c = 0.8 \text{ eV}$  or  $\Delta E_c = 1.0 \text{ eV}$ .

For high performance QCLs and long lifetimes, high crystalline quality is a strong requirement. This was believed to only be possible with lattice matched semiconductor heterostructure materials to prevent dislocations. It was, however, discovered that thin layers of strained material could be grown without inducing dislocations. Since the active region of QCLs is also based on thin quantum wells and barriers, it is compatible with these findings. As the strain is cumulative, the total strain induced by all individual layers must stay below a critical value to prevent dislocations. If strain with only one sign is used, i.e. only tensile strain or only compressive strain, the critical value of the total strain of all the layers determines the amount of strain that can be incorporated into every individual layer. If, on the other hand, materials with opposite strain are used, i.e. compressive strain for the wells and tensile strain for the barriers, the strain can be compensated on the scale of nanometers and the total strain can be kept very small while a considerable strain can be introduced into every individual layer. In the example mentioned above, the well material  $\text{In}_x\text{Ga}_{1-x}\text{As}$  is compressively strained and the barrier material  $\text{Al}_x\text{In}_{1-x}\text{As}$  is tensile strained. This leads to some attractive features: The conduction band discontinuity can be increased to about 750 meV in comparison to the 520 meV of the lattice matched material system. Secondly, InP waveguides with their low losses and high thermal conductivity can be used. Finally, the amount of strain can be chosen almost arbitrarily according to the target wavelength.

Though being promising, this strained material system still limits the individual layer thicknesses to a maximum thickness on the order of a few nanometers. Additionally, the strong condition of the strain compensation imposes an important constraint on the laser design and it is not possible to tune the barrier and well thicknesses independently. Especially the injector design is limited by these design constraints. In 2006, Semtsiv and coworkers [158] presented a solution to this problem. By introducing a composite barrier consisting of the two components  $\text{AlInAs}$  and  $\text{AlAs}$ , the

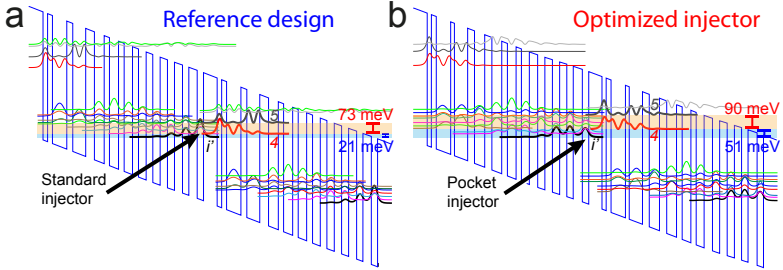


**Figure 6.3:** Adapted from Bismuto *et al.* [160]. **a)** Conduction band diagram of a standard injector design. **b)** Optimized injector design, the so called *pocket injector*, with a lowered injector ground state acting as a charge reservoir, while the injection is reached via the excited states.

benefit of the high barrier can be conserved, while the barrier thicknesses and the strain can be tuned almost independently. QCLs lasing at  $3.05\ \mu\text{m}$  wavelength at cryogenic temperatures were achieved in such a material composition [159].

An additional modification of the injector design was made by Bismuto *et al.* [160]. The difference between a traditional injector and the new design is shown in Fig. 6.3, where the differences between a reference design (a) and the new injector structure (b) are highlighted. Firstly, the energy separation between the injector state  $i'$  and the upper lasing state 4 is increased by approximately 30 meV from the reference to the optimized structure. In this new structure, the injector ground state acts as a charge reservoir while the injection is achieved by the excited states. Thus, the maximum current of the structure corresponds to an alignment of the excited injector states, as opposed to the alignment of the injector ground state as in the reference structure. This new injector scheme was named *pocket injector* [160]. The second difference between the reference and the new design is the increased separation of the upper lasing state 4 and the first excited state 5 by  $\sim 20$  meV reducing thermal excitation of electrons into the continuum. It has been shown experimentally by Bismuto *et al.* that such an optimized design has significantly higher performance compared to its reference design [160].

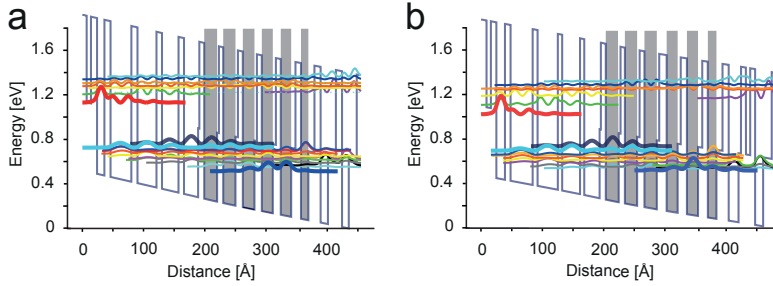


**Figure 6.4:** SOURCE: Riedi *et al.* [76]. Conduction band diagram of one period of the active region at an average field of 120 kV/cm. The shaded area shows the location of the doping. Moduli squared of the relevant wavefunctions are shown. **a)** shows the active region as presented by Bismuto *et al.* with a center wavelength of 3.3  $\mu\text{m}$ . Shaded areas are doped wells with a doping of  $6 \times 10^{17} \text{ cm}^{-3}$ . **b)** Same material system but shifted to a center wavelength of 3.7  $\mu\text{m}$ . An additional composite barrier was inserted into the injector to maintain high injection efficiencies. The shaded wells are doped with  $5 \times 10^{17} \text{ cm}^{-3}$ .

### 6.3 EC tuning around 3.3 $\mu\text{m}$ wavelength

Using the material system and pocket injector discussed above in a bound-to-continuum architecture [110] Bismuto *et al.* demonstrated room temperature lasing at 3.3  $\mu\text{m}$  [51]. The conduction band diagram of one period and the moduli squared of the relevant wavefunctions are shown in Fig. 6.4 a). The layer sequence for one period of the original 3.3  $\mu\text{m}$  stack in nanometers is, starting from the injector barrier:

**0.5/0.7/1.0/1.2/1.0/3.4/1.0/3.1/0.9/2.7/0.9/2.3/0.2/0.8/2.1/0.3/0.7/2.0/0.4/0.8/1.9/0.4/0.8/1.8/0.5/0.8/1.7/0.7/0.9/1.2/1.0/1.0/1.2/1.3/1.0/1.1/1.3,**

where  $\text{In}_{0.715}\text{Ga}_{0.285}\text{As}$  layers are in roman,  $\text{In}_{0.52}\text{Al}_{0.48}\text{As}$  layers are in *italic* and **AlAs** ones are in **bold**, underlined layers are doped to  $6 \times 10^{17} \text{ cm}^{-3}$ . The epitaxial growth was optimized in order to allow the growth of strain compensated material and at the same time assure a control of the local strain [161].

Devices of two different growths of such a design (EV1517 and EV1518) were coated with back facet HR coatings and front facet AR coatings, see Fig. 6.5 c). Fig. 6.5 a) and b) show the EC tunings around 3.3  $\mu\text{m}$  wavelength of two devices. Both devices were based on the design by Bismuto *et al.* [51] but from different epitaxial growths. The device shown

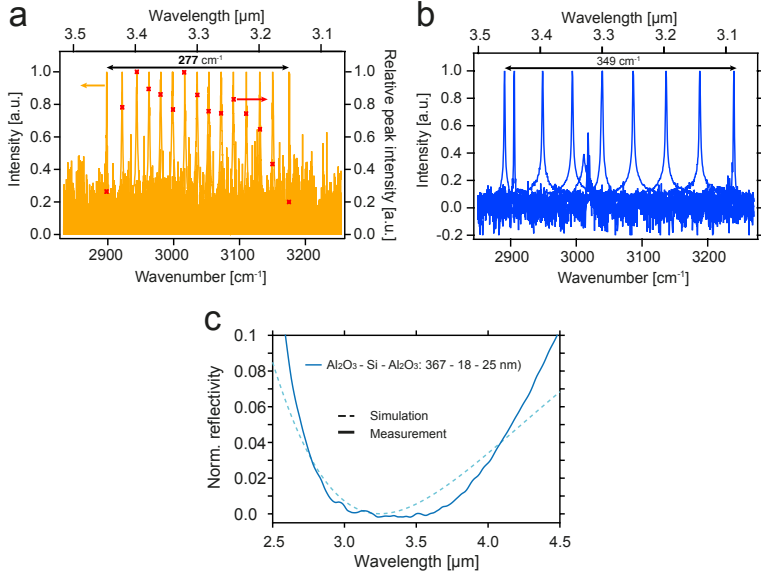


**Figure 6.5:** External cavity tuning of the active region design centered around 3.3  $\mu\text{m}$  wavelength. **a)** MBE growth EV1517: 3.9 mm long and 11  $\mu\text{m}$  wide device, operated in pulsed mode at 1 % duty cycle (100 ns, 100 kHz). **b)** MBE growth EV1695: A 3.5 mm long device, with a ridge width of 9  $\mu\text{m}$ , was operated in pulsed mode at 0.5 % duty cycle (50 ns, 100 kHz). **c)** Simulation and measurement of an AR coating with reflectivities below 1 % over the tuning range.

in Fig. 6.5 a) was 3.9 mm long and 11  $\mu\text{m}$  wide and was operated in pulsed mode at 1 % duty cycle (100 ns, 100 kHz) while the device shown in Fig. 6.5 b) had the dimensions of 3.5 mm and 9  $\mu\text{m}$  and was operated at 0.5 % duty cycle (50 ns, 100 kHz). Tuning of 9% and 11 % of the center frequency was achieved, respectively. This difference is most likely due to the fact that the devices came from two different growths and were therefore processed at different times, which will influence the laser performance.

## 6.4 Active region design at 3.7 $\mu\text{m}$ wavelength

To further increase the tuning range in the 3 to 4  $\mu\text{m}$  range, a second active region with the same material system but with a center wavelength of 3.7  $\mu\text{m}$  was designed.

In order to be able to grow both stacks together, they had to be designed with the same material system, InGaAs/InAlAs-AlAs [162]. The pocket injector scheme [160] used in the original design was also used in the design at 3.7  $\mu\text{m}$ . To redshift the emission frequency, the transition energy had to be lowered, which was achieved by stretching the whole structure, i.e adjusting the barrier and well widths while keeping the strain balanced. To maintain the high injection efficiency of the pocket injector, a second composite barrier was introduced into the injector region, stretching the injector miniband.

Fig. 6.4 shows the original 3.3  $\mu\text{m}$  design (a) with one composite injector barrier and the 3.7  $\mu\text{m}$  active region (b) with the second double barrier in the injector. The shaded areas show the location of the doping in both active regions. It can be seen that both designs are similar in injector and transition design.

The layer sequence for one period of the 3.7  $\mu\text{m}$  stack in nanometers, starting from the injector barrier is:

**0.7/0.7/0.9/1.4/0.9/3.9/0.8/3.3/0.7/2.9/0.7/2.5/0.2/0.8/2.1/0.3/0.7/  
2.0/0.4/0.8/2.0/0.4/1.2/1.8/0.5/1.0/1.8/0.7/0.9/1.2/1.0/1.0/1.6/0.4/  
0.8/0.7/0.8/1.3/1.4**

with a doping of the underlined layers of  $5 \times 10^{17} \text{ cm}^{-3}$  and the notation as before.

The simulated gain and electroluminescence are shown in Fig. 6.6 a) and b), while c) shows the measurement of luminescence of a 3.2 mm long and 13  $\mu\text{m}$  wide device (EV1790) at different voltages. The measurements agree well with the simulations.

For the simulations shown in Fig. 6.6 d), the dimensions of a real device (3.75 mm long and 10  $\mu\text{m}$  wide) were taken as an input and compared to the measurements in Fig. 6.6 e). The voltage-current behavior corresponds well to the prediction. Fig. 6.6 e) shows the LIV behavior of the same device at different temperatures from -30°C to 10°C in steps of 10°C. The small change in threshold current density with temperature indicates a low thermal dependence of the threshold current density from temperature. An exponential fit of the temperature versus the threshold current density shows a  $T_0$  of 198 K for the measured device.



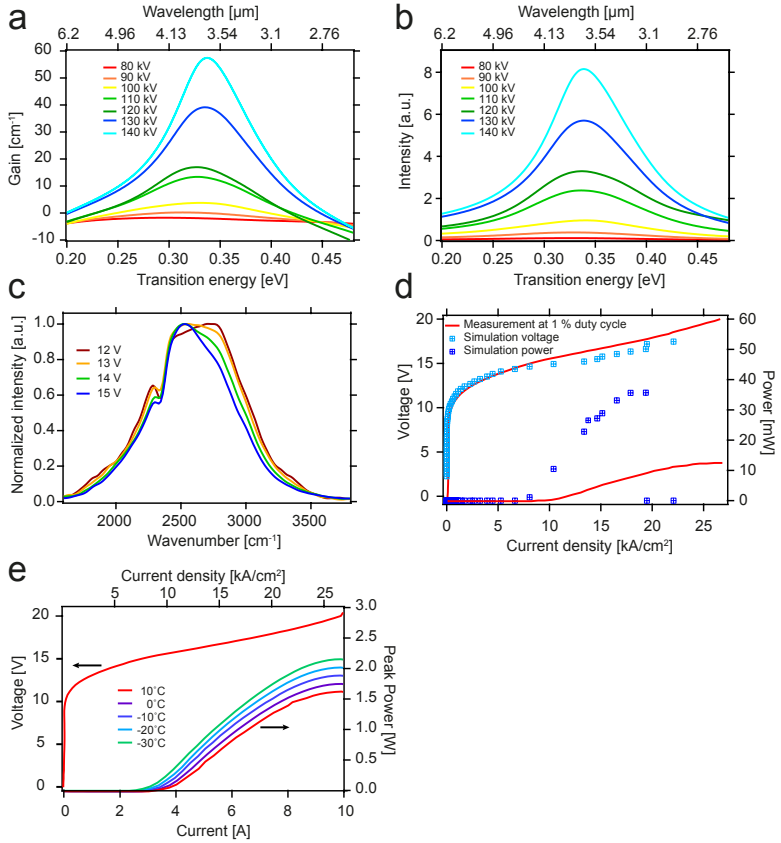


**Figure 6.6:** EV1790. Simulated gain **a)** and luminescence **b)** at applied field from 80 kV to 140 kV in steps of 10 kV. **c)** Measured luminescence at different voltages of a device with a length of 3.2 mm and width of 13  $\mu\text{m}$ . **d)** Light-current-voltage (LIV) simulation of a 3.75 mm long and 10  $\mu\text{m}$  wide device. For the active region, 30 period repetitions, facet reflectivities of 29 % and 4 cm<sup>-1</sup> total losses were assumed, matching the losses of the real device. **e)** EV1790: Measured LIV characteristics of a 3.75 mm long and 10  $\mu\text{m}$  wide QCL at 1 % duty cycle (100 ns, 100 kHz) at temperatures from -30°C to 10°C in steps of 10°C.

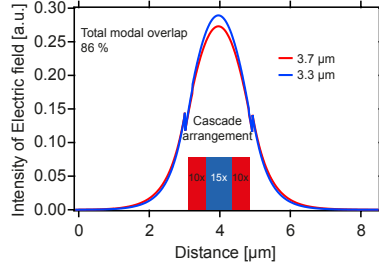


**Figure 6.7:** Calculated modal intensities and profiles for the 3.3  $\mu\text{m}$  and 3.7  $\mu\text{m}$  stack and the symmetrical cascade arrangement of the stacks with 10 3.7  $\mu\text{m}$  stacks each flanking the 15 3.3  $\mu\text{m}$  stacks.

### 6.5 Heterogeneous active region design from 3 to 4 $\mu\text{m}$ wavelength

The two active regions described above were combined into a heterogeneous double-stack active region. To obtain a balanced total gain, the two active regions were stacked symmetrically with 15 short wavelength stacks in the center and flanked by 10 long wavelength stacks on either side [105] as shown in Fig. 6.7. Placing the short wavelength stack in the center has two advantages. First, the photons with higher energies experience stronger confinement in the waveguide compared to the lower energy photons, which leads to a higher total modal overlap and therefore to a larger total modal gain. Second, the overlap with the short wavelength stack is reduced. [95, 105]. The resulting total modal overlap of the optical mode with the active region was calculated to be  $\Gamma = 86\%$ .

The heterogeneous structure was grown in a solid source MBE and subsequently processed into buried heterostructure lasers, see chapter 2, cleaved into individual lasers and mounted epi-side up onto copper submounts. The device presented in this chapter was 5.3 mm long with a 9  $\mu\text{m}$  wide ridge.

Fig. 6.8 a) shows simulations and measurements of the luminescence at different current densities. Simulations and measurements show a broad and stable full-width-at-half-maximum (FWHM) of  $\sim 900 \text{ cm}^{-1}$  with different current densities. The measured luminescence (bold lines) shows a

slight blue-shift compared to simulations (dashed lines). Fig. 6.8 b) shows the simulated total gain at different current densities. For this device a characteristic temperature of  $T_0 = 154$  K was measured indicating the low temperature dependence of the gain.

The light-current-voltage (LIV) characteristics of the device were measured in pulsed mode at 1 % duty cycle (50 ns, 200 kHz) at 289 K for the as-cleaved facet, the HR coated and HR/AR coated device. The LIV in the EC setup was measured at 249 K, however. To be able to compare the threshold currents of all the measurements, the threshold for the EC setup was calculated to be 3.13 A at 289 K with the help of the characteristic temperature of the device,  $T_0 = 154$  K. As shown in Fig. 6.8 c), after high-reflectivity (HR) coating of the device back facet with a standard  $\text{Al}_2\text{O}_3$ -Au coating,  $R_{\text{HR}} = 99\%$ , a lowering of the threshold current density and an increase in the slope efficiency was observed. From the reduction in threshold current density we extrapolated the total waveguide losses (resonant and non-resonant losses) to be  $3.8 \text{ cm}^{-1}$ . Similarly the change in slope efficiency yields a value of the non-resonant losses of  $2.6 \text{ cm}^{-1}$ , which we attribute partly to visible inhomogeneities along the active region ridge. The resonant losses thus are estimated to be  $1.2 \text{ cm}^{-1}$ . This value has to be compared to the prediction of our model,  $2.5 \text{ cm}^{-1}$ , obtained by extrapolating the maximum computed gain as a function of current density down to zero. The difference between the experimental and predicted value could originate from either storage of electrons in the lateral valleys or a sub unity efficiency of the doping that effectively reduced the electron density participating in transport.

## 6.6 EC tuning from 3 to 4 $\mu\text{m}$ wavelength

Fig. 6.8 c) shows in blue the light-current-voltage characteristic of the QCL in the EC setup measured at 249 K, taken at the EC wavelength of  $2711 \text{ cm}^{-1}$ . From the change in threshold between the back facet HR coated device and the double side coated device inside the external cavity, the total reflectivity of the cavity was calculated to be 69 %. In a further experiment, the threshold current density was measured as a function of the external cavity emission energy. In Fig. 6.8 b), the inverse of the mea-

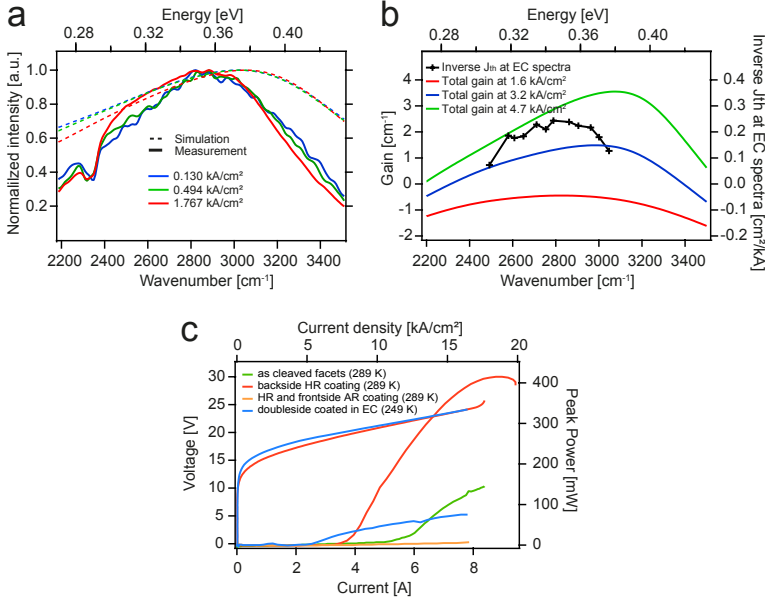


**Figure 6.8:** EV1792. **a)** Luminescence simulations (dashed) and measurements for the heterogeneous active region at different current densities. **b)** Simulated gain for both individual cascades and the total gain. The black crosses show the inverted threshold current densities at different wavelengths of the EC spectra. **c)** LIV characteristics of a 5.3 mm long, 9  $\mu\text{m}$  wide device in pulsed mode (50 ns, 200 kHz) for the as-cleaved (green), HR coated (red) and HR/AR (orange) coated laser at 289 K. The external cavity LIV (blue) was taken at 249 K at the wavelength of  $2711\text{ cm}^{-1}$ .

sured threshold current density is compared to the computed gain, in the tuning range of the experiment. As in the case for the comparison of the luminescence, a higher peak gain energy and a broader range is predicted, perhaps indicating an overestimate of the gain broadening by the model.

For operation in an Littrow configuration EC setup, cf. chapter 5, and to suppress Fabry-Pérot laser chip modes, the front facet was coated with a three-layer AR coating consisting of  $\text{Al}_2\text{O}_3$ -Si- $\text{Al}_2\text{O}_3$  (94 - 86 - 543 nm). As shown in Fig. 6.9 a), where this measurement is reported, a significant reduction of the front facet reflectivity to a maximum value of 1.4 % over the whole tuning range (highlighted area) has been achieved. As shown in Fig. 6.8 c), an additional indication of the high quality of the anti-reflection

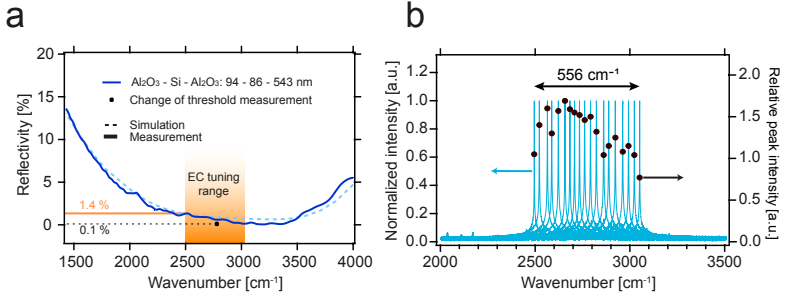


**Figure 6.9:** EV1792. **a)** Simulation (dashed, blue) and transmission measurement (solid, blue) of the three layer  $\text{Al}_2\text{O}_3$ -Si- $\text{Al}_2\text{O}_3$  (94 - 86 - 543 nm) anti-reflection front facet coating. The green line indicates the 1.4 % level which is the maximum reflectivity calculated and measured for the tuning range. The black square indicates the position and reflectivity of 0.1 % calculated from the change in threshold due to facet coating. The shaded area shows the tuning range covered by the device with this coating. **b)** 556  $\text{cm}^{-1}$  single mode tuning. The spectra at different wavelengths were normalized to the same intensity and the black dots show the relative intensities of the different mode peaks since they were measured with an uncalibrated detector.

coating is the fact that the coated laser did not achieve threshold operation in its whole dynamical range, setting an upper bound of  $<0.1\%$  for the residual facet reflectivity, shown with a black square in Fig. 6.9 a). This value compares well to two-layer AR coatings done in previous works, where reflectivities of 0.7 % were measured [163].

To obtain the EC tuning spectra, the coated device was carefully aligned inside the setup and tuned over 556  $\text{cm}^{-1}$ , as displayed in Fig. 6.9 b). The final tuning range from 2495  $\text{cm}^{-1}$  (4.01  $\mu\text{m}$ ) to 3051  $\text{cm}^{-1}$  (3.28  $\mu\text{m}$ ) covers one third of the first atmospheric window (3 – 5  $\mu\text{m}$ ) and corresponds to a tuning of 20% of the center wavelength. In this wavelength region, tuning ranges in the order of 100  $\text{cm}^{-1}$  in Sb-containing material systems [164] and 275  $\text{cm}^{-1}$  in Sb-free material systems [162] have been reported. The 556  $\text{cm}^{-1}$  shown here are an improvement by a factor of two in tuning range with peak output powers in the order of tens of mW for all wavelengths. The spectra at different wavelengths were normalized to the same intensity and the black dots in Fig. 6.9 b) show the relative intensities of the different mode peaks since they were measured with an uncalibrated detector.

The device showed gain starving on the short wavelength end of the spectrum whereas on the long wavelength end of the tuning we were limited by mode competition, i.e. the AR coating reflectivity, as is confirmed by Fig. 6.9 a). To overcome the gain starving, longer devices could be tested to increase the length of the gain medium. Another approach is the optimization of the AR coating, especially to further reduce the front facet reflectivity on the long wavelength side.

In this work the focus was on the tuning range and not output power. We believe that using a back facet extraction setup would significantly increase the peak output power with a small sacrifice in tuning range.

# Broadband QCLs in the 5 - 10 $\mu\text{m}$ range

This chapter summarizes the results of the external cavity tuning at wavelengths between 5 and 10  $\mu\text{m}$ . Different active region structures that were not designed within the framework of this thesis were coated and characterized in external cavity.

## 7.1 EC tuning around 5.7 $\mu\text{m}$

This first structure is a heterogeneous structure composed of two active regions with center wavelengths of 5.26  $\mu\text{m}$  ( $1900\text{ cm}^{-1}$ ) and 6.25  $\mu\text{m}$  ( $1600\text{ cm}^{-1}$ ) (EV1815, processed by P. Jouy). The structure is based on

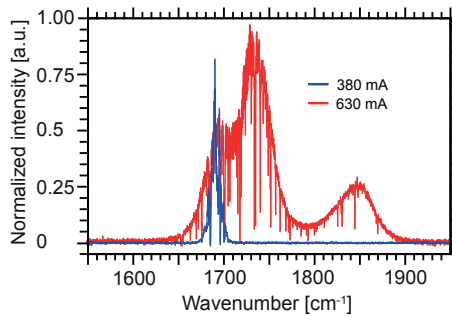


**Figure 7.1:** Lasing spectrum of an uncoated device at currents just above threshold (380 mA) and close to rollover (630 mA). The spectrum broadens considerably over the dynamic range of the device.

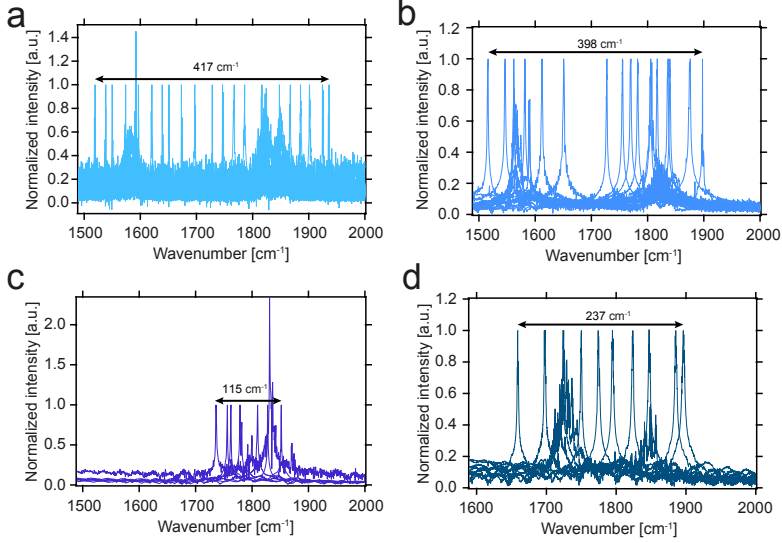


**Figure 7.2:** EV1815. **a)** Pulsed EC tuning at 1 % duty cycle with a center wavelength tuning of 24 %. **b)** EC tuning at 50 % duty cycle and 23 % center wavelength tuning. **c)** Cw tuning without AR coating and 6.4 % center wavelength tuning. **d)** Cw EC tuning with AR coating and 13% center wavelength tuning.

a bound to continuum design and lases at wavenumbers from  $1880\text{ cm}^{-1}$  ( $5.3\text{ }\mu\text{m}$ ) around threshold (380 mA) to  $1670\text{ cm}^{-1}$  ( $6\text{ }\mu\text{m}$ ) close to rollover current (630 mA), as can be seen in Fig. 7.1. Two different devices were then coated and characterized in external cavity. The first device had an HR coating on the back facet as well as a front facet AR coating. Fig. 7.2 a) and b) show the tuning of that device at 1 % (50 ns, 200 kHz) and 50 % (250 ns, 2 MHz) duty cycle, respectively. They show tuning ranges of  $417\text{ cm}^{-1}$  and  $398\text{ cm}^{-1}$ , which corresponds to 24 % and 23 % of their center frequencies. Both devices are limited by mode competition on both edges of the spectrum. That is an indication that the AR coating of the front facets was not sufficient to suppress the Fabry-Pérot modes on the edges of the tuning range. Thus, an AR coating with lower residual reflectivities would need to be applied to the front facet to further increase the tuning range.



The device in Fig. 7.2 c) shows a device driven in continuous wave (cw) but without a front facet AR coating. The tuning range is limited by mode competition on the long wavelength edge, while the short wavelength edge is limited by gain starving. The tuning of  $115\text{ cm}^{-1}$  corresponds to 6.4 % center wavelength tuning. Fig. 7.2 d) shows another device in cw but with a front facet AR coating. For this device, a center wavelength tuning of 13 % was achieved, but the device was limited by mode competition on both edges.

## 7.2 EC tuning around 8 $\mu\text{m}$

The devices of this design were provided by Alpes Lasers SA as already mounted and HR coated chips (sbcw/d180). The front facets were AR coated at ETH and then tested in external cavity. A total of three devices (3 mm x 8  $\mu\text{m}$  (a); 3 mm x 8  $\mu\text{m}$  (b); 4.5 mm x 8  $\mu\text{m}$  (c)) of this design were tested and the tuning results are shown in Fig. 7.3. Fig. 7.3 d) shows the spectrum of a HR coated device of 3 mm length and 8  $\mu\text{m}$  width at 15.5 V (close to rollover,  $\sim 780\text{ mA}$ ). It clearly shows two distinct Fabry-Pérot peak regions. One group is centered around  $1010\text{ cm}^{-1}$  (9.9  $\mu\text{m}$ ) and the second one around  $1210\text{ cm}^{-1}$  (8.26  $\mu\text{m}$ ). From  $1020\text{ cm}^{-1}$  to  $1170\text{ cm}^{-1}$ , no lasing is observed. The total width of the lasing spectrum covers the wavelength region from 8 to 10  $\mu\text{m}$  ( $1250\text{ cm}^{-1}$  -  $1000\text{ cm}^{-1}$ ). Fig. 7.3 f) shows a luminescence spectrum just above threshold (140 mA), which shows a broad FWHM of  $370\text{ cm}^{-1}$ , from  $1057\text{ cm}^{-1}$  (9.46  $\mu\text{m}$ ) to  $1427\text{ cm}^{-1}$  (7.01  $\mu\text{m}$ ). Considering the AR coating applied to the devices, see Fig. 7.3 e), which does not reduce the facet reflectivities below 1 %, the achieved tuning ranges have to be noted. The lasing spectra shows a gap in which no lasing is observed, as is shown in Fig. 7.3 d). But in the external cavity, all devices were tuned over or well into this gap. For the devices shown in Fig. 7.3 a) and b), this can be explained by the AR coating on the front facet, see Fig. 7.3 e). These devices exhibit center wavelength tunings of 30 % (a) and 37 % (b), respectively. The device in Fig. 7.3 c) did not have a front facet AR coating and still exhibits a tuning of  $243\text{ cm}^{-1}$ , corresponding to 20 % center wavelength tuning. Since the luminescence gives a good indication of the true gain, its broad and relatively flat shape

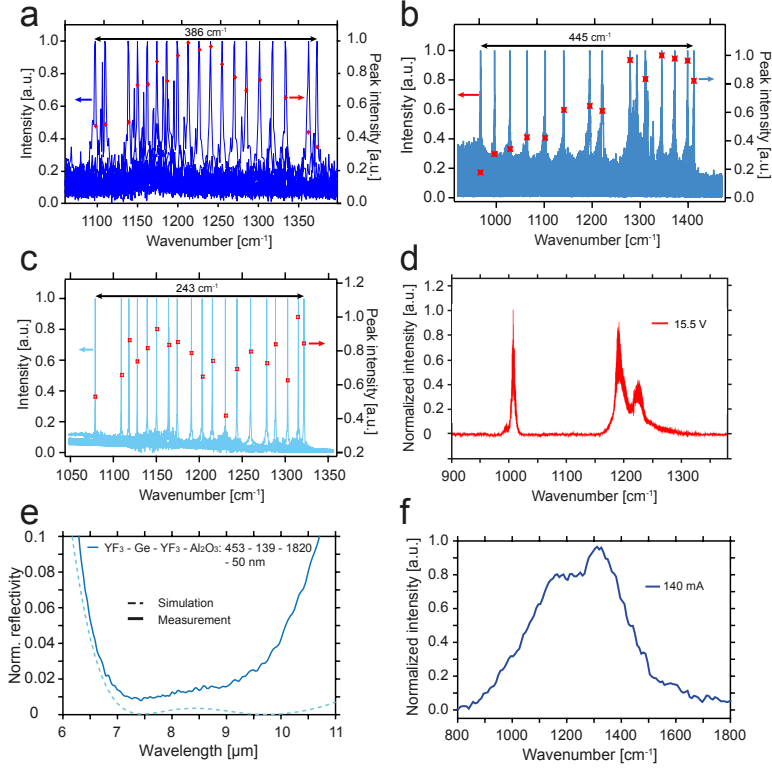


**Figure 7.3:** Alphas Lasers SA design. **a)** EC tuning of a 3 mm long and 8  $\mu\text{m}$  wide device at 1% duty cycle (100 ns, 100 kHz) with an AR coated back facet. **b)** EC tuning of a 3 mm long and 8  $\mu\text{m}$  wide device with AR coating in pulsed mode at 1% duty cycle (50 ns, 200 kHz). **c)** Tuning of a 4.5 mm long and 8  $\mu\text{m}$  wide device without a front facet AR coating. **d)** Lasing spectrum of the HR coated device (3 mm x 8  $\mu\text{m}$ ) from b) at 15.5 V in pulsed mode (100 ns, 200 kHz) (Courtesy of Alphas Lasers SA). **e)** AR coating applied to the front facets of the devices in a) and b). **f)** Luminescence of the device in b) at 140 mA (just above threshold).

(Fig. 7.3 f)) explains that the device could be tuned over the gap in the lasing spectrum. But especially for the device in Fig. 7.3 b), the tuning range could be extended beyond the FWHM of the luminescence and the lasing spectrum. This can be attributed to a very well aligned QCL, lens and grating.

### 7.3 EC tuning of heterogeneous cascade designs with three and five colors

To cover the wavelength range from 5  $\mu\text{m}$  to 10  $\mu\text{m}$ , a heterogeneous cascade active region design, consisting of three active regions at 5.5  $\mu\text{m}$ , 6.4  $\mu\text{m}$  and 7.8  $\mu\text{m}$  center wavelengths, was characterized in EC configuration. The active regions are all based on a strained InGaAs/InAlAs material system and developed by N. Wälti and J. M. Wolf. The cascade arrangement was symmetrical from the center outwards with 14 periods of the 5.5  $\mu\text{m}$  stack, 7 periods each of the 6.4  $\mu\text{m}$  stack and finally 10 periods of the 7.8  $\mu\text{m}$  stack on both sides (EV2154). Fig. 7.4 b) shows the LIV characteristics of a 6 mm long and 5  $\mu\text{m}$  wide device in pulsed operation mode (100 ns, 100 kHz). The threshold current was reduced by the back facet HR coating as expected and then increased by the front facet AR coating. From the change of threshold of the HR coated device to the AR coated one, a front facet reflectivity of 1.3 % was calculated, as explained in section 2.5.1. This value corresponds to the measurement shown in Fig. 7.4 c). The 20 nm thick  $\text{Al}_2\text{O}_3$  passivation layer as the last coating layer was not sufficient to prevent the absorption of water as can be seen by the reflectivity peak around 6  $\mu\text{m}$  in Fig. 7.4 c). This can potentially lead to a limitation of the tuning in that wavelength range as well as compromise the stability of the coating under thermal stress, such as is applied when the device is cooled thermoelectrically. The lasing spectra and luminescence of a similar device are shown in Fig. 7.4 a). The lasing spectra as well as the luminescence show three distinct peaks around the design wavelengths of the active region stacks.

The HR and AR coated device was then tested in external configuration. The corresponding LIV measurement is shown in Fig. 7.4 b). Its tuning spectra are shown in Fig. 7.4 d) and exhibit three separated tuning ranges

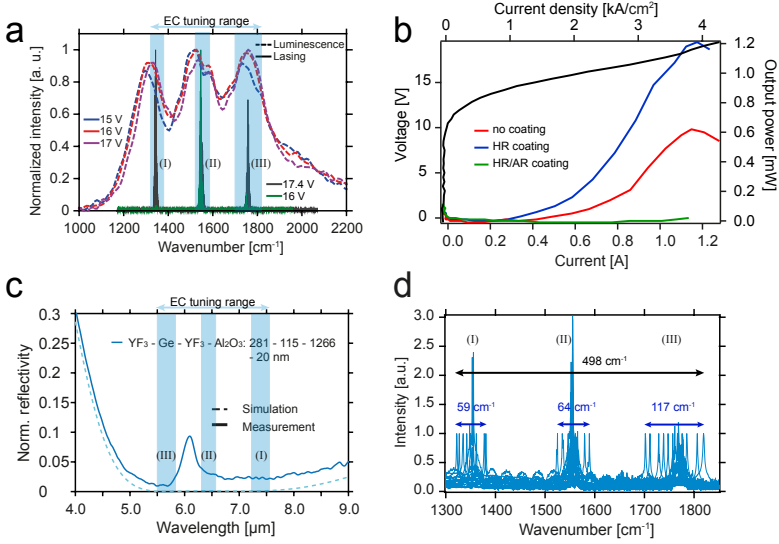


**Figure 7.4:** EV2154. **a)** Subthreshold luminescence and laser spectra of a heterogeneous active region with three designs at 5.5  $\mu\text{m}$ , 6.4  $\mu\text{m}$  and 7.8  $\mu\text{m}$  center wavelengths. The EC tuning range is indicated by the areas shaded in blue (I, II, III). **b)** LIV characteristics at 1 % duty cycle (100 ns, 100 kHz) at  $-20^\circ\text{C}$  for a 6 mm long and 5  $\mu\text{m}$  wide QCL with as-cleaved facets (red), back facet HR coating (blue) and additional front facet AR coating (green). **c)** Simulation and measurement of the applied AR coating. The peak in the measurement is due to the water absorption in YF<sub>3</sub>. **d)** EC tuning with three distinct tuning ranges (I, II, III).

which correspond to the positions of the Fabry-Pérot cavity modes visible in Fig. 7.4 a). To emphasize this overlap, the tuning ranges are indicated in Fig. 7.4 a) by areas shaded in blue. It is worth taking a closer look at all three tuning ranges and the limitations of the tuning.

The range (III) around 1780  $\text{cm}^{-1}$  (5.6  $\mu\text{m}$ ) is limited on the short wavelength edge (5.49  $\mu\text{m}$ , 1820  $\text{cm}^{-1}$ ) by gain starving while the longer wavelength edge (5.88  $\mu\text{m}$ , 1702  $\text{cm}^{-1}$ ) is limited by mode competition. This can be explained by the AR coating depicted in Fig. 7.4 c), where the lowest reflectivity (1.1 %) is at a wavelength of 5.5  $\mu\text{m}$ , suppressing the FP chip modes. The long wavelength edge of range (I) is on the flank of the water absorption and thus has a higher reflectivity (2.5 %), in this case allowing the FP chip modes to reach threshold. This individual tuning of 117  $\text{cm}^{-1}$  corresponds to a center wavelength tuning of 6.5 %.

The central tuning range (II) is limited on both sides by gain starving even though the reflectivities of the AR coating range between 3 and 4 %. However, the luminescence and lasing spectra in Fig. 7.4 a) indicate that the gain is possibly highest in this wavelength range, giving preference to the EC modes. The tuning of  $64 \text{ cm}^{-1}$  from  $1524 \text{ cm}^{-1}$  ( $6.56 \text{ }\mu\text{m}$ ) to  $1589 \text{ cm}^{-1}$  ( $6.3 \text{ }\mu\text{m}$ ) corresponds to a center wavelength tuning of 4.1 %. The tuning range (I) is the narrowest in wavenumber, i.e.  $59 \text{ cm}^{-1}$ , from  $1322 \text{ cm}^{-1}$  ( $7.56 \text{ }\mu\text{m}$ ) to  $1381 \text{ cm}^{-1}$  ( $7.24 \text{ }\mu\text{m}$ ) but corresponds to a center wavelength tuning of 4.3 %. This tuning range is limited on both sides by mode competition, explained by the facet reflectivity of 4 % over the whole tuning range as well as the luminescence being weakest in this wavelength range.

If we disregard the gaps in the tuning and consider the overall tuning, almost  $500 \text{ cm}^{-1}$  were covered with a single device, corresponding to a center wavelength tuning of 31.6 % around  $6.37 \text{ }\mu\text{m}$  ( $1570 \text{ cm}^{-1}$ ). This is comparable to the tuning around  $8 \text{ }\mu\text{m}$  shown in the previous section. Another similarity to the devices shown in Fig. 7.3, are the gaps in the lasing spectrum. In the previous section, we showed that with a coating with reflectivities  $\leq 1.8 \text{ }\%$ , such a gap can be tuned over. Thus it is reasonable to assume, that a flat and low reflectivity coating allows for closing these gaps in the tuning. If such a low reflectivity coating is applied and the gaps tuned over, tuning ranges of  $600 \text{ cm}^{-1}$  are realistic targets for such a three-color structure.

On the basis of this three color design, an even broader design was created by adding an additional stack both on the long and short wavelength side. The center wavelengths are  $5.0 \text{ }\mu\text{m}$ ,  $5.5 \text{ }\mu\text{m}$ ,  $6.4 \text{ }\mu\text{m}$ ,  $7.8 \text{ }\mu\text{m}$  and  $9.5 \text{ }\mu\text{m}$  and were stacked symmetrically around the shortest wavelength stack. Fig. 7.5 a) shows the lasing and luminescence spectra of a  $3 \text{ mm}$  long and  $4 \text{ }\mu\text{m}$  wide device in pulsed mode ( $100 \text{ ns}$ ,  $100 \text{ kHz}$ ). The strongest peak in the lasing spectrum as well as in the luminescence spectrum is centered around  $1370 \text{ cm}^{-1}$  ( $7.3 \text{ }\mu\text{m}$ ). The large difference in intensity indicates possible challenges for EC tuning such devices. An AR coating with very small residual reflectivities ( $\sim 0.1 \text{ }\%$ ) is needed over a wavelength range covering more than  $800 \text{ cm}^{-1}$  from  $1200 \text{ cm}^{-1}$  ( $8.33 \text{ }\mu\text{m}$ ) to  $2000 \text{ cm}^{-1}$  ( $5.0 \text{ }\mu\text{m}$ ) to suppress such strong Fabry-Pérot chip modes. A

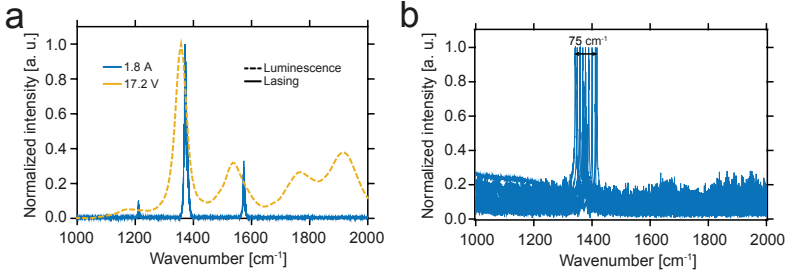


**Figure 7.5:** EV2188. **a)** Subthreshold luminescence and laser spectra of a five color heterogeneous active region with center wavelengths of 5.0  $\mu\text{m}$ , 5.5  $\mu\text{m}$ , 6.4  $\mu\text{m}$ , 7.8  $\mu\text{m}$  and 9.5  $\mu\text{m}$ . **b)** EC tuning of a 6 mm long and 4  $\mu\text{m}$  wide laser in pulsed mode (100 ns, 100 kHz) at 253 K. The tuning is limited by gain starving on both sides.

6 mm long and 4  $\mu\text{m}$  wide QCL was coated with the AR front facet coating shown in Fig. 4.10 which exhibits reflectivities between 3 and 6 % in the lasing range. The device was operated in pulsed mode at 1 % duty cycle (100 ns, 100 kHz) at 253 K. EC tuning was achieved from 1342  $\text{cm}^{-1}$  (7.45  $\mu\text{m}$ ) to 1417  $\text{cm}^{-1}$  (7.06  $\mu\text{m}$ ) which corresponds to a center wavelength tuning of 5.4 %. The center wavelength of the tuning corresponds to the strongest lasing and luminescence peak and is shown in Fig. 7.5 b). For this device, the tuning was limited by gain starving on both sides, indicating an unbalanced gain structure of this five color heterogeneous design.

---

# Superluminescence and amplifiers

This chapter summarizes the results on subthreshold behavior of QCLs. It analyzes superluminescent behavior and corresponding output powers and gives possible applications of such devices.

## 8.1 Introduction

Speckle patterns are a general problem that occur in most laser-based imaging techniques [88, 89, 90]. These interference patterns reduce the resolution power of different imaging techniques and strongly limit the use of such applications. The effect of speckles has been mentioned as early as the 1960s [165, 166] and it was soon realized that it arises from interference patterns of strongly coherent light sources on rough surfaces. A short coherence time is required to prevent the light from interfering. Another requirement for good imaging quality is single mode optics which requires a high brilliance. Superluminescent diodes fulfill both requirements. They are based on amplified spontaneous emission in a confined waveguide. Such devices therefore combine the short coherence time of amplified spontaneous emission, necessary to reduce speckle, with a high brilliance, necessary for single mode optics.

Superluminescent sources are the core of optical coherence tomography (OCT) [91], where coherence lengths below 15-30  $\mu\text{m}$  and irradiances above 100  $\mu\text{W}$  are required [93]. OCT is heavily applied in the

near-infrared wavelength range for industrial and medical applications [167, 168]. Such applications include high-resolution and cross-sectional tomographic real time imaging of e.g. internal structures in the human eye [169]. Extending OCT to the mid-IR will potentially expand the use for biomedical imaging to cancerous tissues [170] and compounds such as collagen amide, phosphate and carbonate [91]. Mid-IR OCT systems can also aid in industrial process monitoring [171]. QCL structures present themselves as potential superluminescent diodes and have been investigated over the years. While first devices suffered from low output powers ( $\sim 25 \mu\text{W}$  at 10 K) [172], more recent results show output powers of  $\geq 10 \text{ mW}$  at 250 K [173, 174]. These latest results, however, do not show pure superluminescent diode characteristics, since all devices shown by Aung *et al.* and Zheng *et al.* [173, 174] feature a lasing threshold. The superluminescent behavior of the devices could therefore only be measured in a narrow current range below threshold and it is difficult to determine the lasing threshold with high accuracy. Other potential approaches use rapid swept-source lasers also in the mid-infrared [90].

## 8.2 Theory

The basic working principle of a superluminescent diode (SLED) is similar to a laser diode, in general based on an electrically driven pn-junction. When biased, the material becomes optically active and generates amplified spontaneous emission over a wide range of wavelengths that depend on the composition of the gain material and the injection current level. In a laser, this amplified light undergoes internal feedback and mode selection by the cavity, i.e. the front and back facet in the case of a QCL. This internal feedback narrows the emission bandwidth and the device will reach its lasing threshold. To obtain a broadband emission output with low coherence, but maintain the high emission intensity of the amplified light, the cavity restriction has to be removed. For QCLs, this is done with anti-reflection (AR) coatings on both the front and back facets.

Since the emission bandwidth of a QC SLED depends on the gain structure the same way as any other QCL, the requirements on the gain structure are the same as for a broadband QCL to be operated in external cavity.



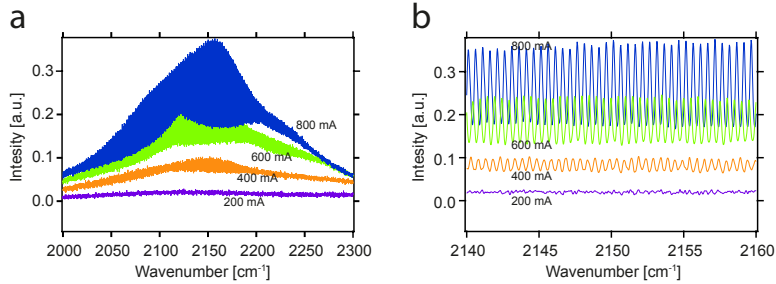


**Figure 8.1:** EV1299. High-resolution ( $0.075 \text{ cm}^{-1}$ ) subthreshold luminescence of a 3 mm long QCL as a function of current, from 200 mA to 800 mA, in steps of 200 mA. **a)** shows the full bandwidth of the laser. **b)** The Fabry-Pérot fringes are clearly visible as well as the increase of the contrast with increasing current.

A broad and flat gain is required to have an evenly distributed superluminescent spectrum. Thus existing QCL material was used to show a proof of principle.

### 8.2.1 Fabry-Pérot cavity fringes

QCLs are edge emitting ridge lasers that are formed by cleaving the ridge to an appropriate length (1-6 mm), forming a Fabry-Pérot (FP) cavity, with facets that exhibit amplitude reflectivities  $r = \sqrt{R}$ . When the subthreshold luminescence spectrum of a free running laser in a Fabry-Pérot cavity is measured, one observes characteristic FP fringes in the intensity that originate from the feedback of the FP cavity. Fig. 8.1 a) shows high resolution ( $0.075 \text{ cm}^{-1}$ ) spectra of a 3 mm long, double side AR coated QCL, operated at different currents below threshold. It shows how the spectrum is defined by two envelope functions, one tracking the maxima and minima of the FP fringes, respectively. Fig. 8.1 b) zooms in around the emission peak and clearly shows the correlation of the fringe contrast with injection current.

Since the FP fringes originate in the FP chip cavity, it can be assumed that the fringe contrast depends on the mirror reflectivities as well as on the current. To find this correlation between injected current and fringe contrast, we can consider a stationary mode running in the cavity of length

$l$  and find

$$r^2 e^{2i\beta l} = 1 \quad (8.1)$$

where the propagation constant  $\beta$  for a mode with a vacuum propagation constant  $k_0 = 2\pi/\lambda$  can be written as

$$\beta = n_{\text{eff}} k_0 - i \frac{g - \alpha_{\text{wg}}}{2} \quad (8.2)$$

with  $g - \alpha_{\text{wg}}$  the net gain. From the condition on the wavelength

$$\lambda = \frac{2n_{\text{eff}} l}{N}, \quad (8.3)$$

where  $N$  is a positive integer, and a wavelength dependent effective refractive index, we find the mode spacing between two neighboring FP modes to be

$$\Delta\lambda = \frac{\lambda^2}{2ln_g} \quad (8.4)$$

or in wavenumbers

$$\Delta\left(\frac{1}{\lambda}\right) = \frac{1}{2ln_g}, \quad (8.5)$$

where the group refractive index, expressed in wavelength and wavenumbers, respectively, is written as

$$n_g = n_{\text{eff}} - \lambda \frac{\partial n_{\text{eff}}}{\partial \lambda} = n_{\text{eff}} + \frac{1}{\lambda} \frac{\partial n_{\text{eff}}}{\partial \left(\frac{1}{\lambda}\right)}. \quad (8.6)$$

Fig. 8.1 b) clearly shows the correlation between the fringe contrast and the current. This effect can be employed to calculate the gain by using the Airy formula characterizing the contrast of the FP fringes, here given as a function of wavenumber

$$I\left(\frac{1}{\lambda}\right) = \left(\frac{1-R}{\sqrt{R}}\right)^2 \frac{b}{1+b^2-2b\cos(4\pi n_{\text{eff}} \frac{l}{\lambda})} \quad (8.7)$$

with the phase  $\varphi = 4\pi n_{\text{eff}} l / \lambda$  and  $b$  the parameter controlling the finesse of the FP cavity, given by

$$b\left(\frac{1}{\lambda}\right) = \text{Re}^{(g-\alpha_{\text{wg}})l}. \quad (8.8)$$

### 8.2.2 Hakki-Paoli

Hakki and Paoli first demonstrated the measurement of subthreshold gain in semiconductor lasers in 1973 [175]. The gain evaluation method involved a measurement of the separation of the two envelope functions of the maxima and minima in the spontaneous emission spectrum. We consider a field  $F_1$  and trace its propagation through the device of length  $l$  with mirror reflectivities  $R_1$  and  $R_2$ . When multiple internal reflections interfere constructively the total incident field in a single mode can be written as

$$F_{1T}^+ = \frac{F_1}{1 - \sqrt{R_1 R_2} e^{-\alpha_{wg} l}}, \quad (8.9)$$

whereas the destructive interference is

$$F_{1T}^- = \frac{F_1}{1 + \sqrt{R_1 R_2} e^{-\alpha_{wg} l}} \quad (8.10)$$

where  $\alpha_{wg}$  are the total waveguide losses. From these equations, the gain as a function of wavelength can be extracted in the following way

$$\alpha(\lambda) = \frac{1}{l} \ln \left( \frac{\sqrt{P^+} + \sqrt{P^-}}{\sqrt{P^+} - \sqrt{P^-}} \right) + \frac{1}{2l} \ln(R_1 R_2), \quad (8.11)$$

where  $P^+$  and  $P^-$  are the intensity maxima and minima of the spontaneous spectrum. With this approach, a problem arose for our situation. Since the devices were meant to act as amplifiers, both facets were treated with AR coatings to prevent the device from lasing and acting as a single pass amplifier. This of course reduced the finesse of the FP cavity and thus reduced the fringe contrast, decreasing the possible accuracy of the gain measurements.

An alternative method was presented by Hofstetter and Faist in 1999 [176] where the gain is extracted from the Fourier transform of the acquired subthreshold spectra, i.e. the interferograms themselves. In this technique, the contrast of the FP optical cavity fringes is measured as a function of the current. We can rewrite eq. 8.7 as an infinite series of cosine functions

$$I\left(\frac{1}{\lambda}\right) = \left(\frac{1-R}{\sqrt{R}}\right)^2 \cdot \frac{2b(\frac{1}{\lambda})}{1 - b^2(\frac{1}{\lambda})} \cdot \sum_{m=0}^{\infty} b^m\left(\frac{1}{\lambda}\right) \cdot \cos\left(4\pi n l \left(\frac{1}{\lambda}\right) m\right). \quad (8.12)$$

Taking the Fourier transforms of these transmission functions as a function of the phase  $\varphi$  of two adjacent harmonic peaks ( $\tilde{I}_1(\varphi)$  and  $\tilde{I}_2(\varphi)$ ) and dividing them, we obtain

$$b \left( \frac{1}{\lambda} \right) = \frac{\tilde{I}_2(\varphi)}{\tilde{I}_1(\varphi)}. \quad (8.13)$$

The net gain can then be retrieved by solving eq. 8.8:

$$g \left( \frac{1}{\lambda} \right) - \alpha_{\text{wg}} = \frac{1}{l} \ln \left( \frac{\tilde{I}_2(\varphi)}{\tilde{I}_1(\varphi)} \right). \quad (8.14)$$

However, there are some limitations to this technique. Firstly, the technique outlined above assumes that the measured spectra consist only of first order modes. That is, a second order transverse mode will perturb the measurement in such a way, that this mode will interfere with the fringes of the fundamental mode. This effect can be observed in Fig. 8.1 a). The spectrum at 800 mA shows a lower fringe intensity that is modulated, i.e. modulated by higher order modes. Thus, it should be taken care that the measurement setup has low numerical aperture optics, which will be discussed in section 8.3.3.

### 8.2.3 Optical power

The measured intensity will be compared to that of an ideal SLED. We consider a two level system with an upper level 2 with an upper state population  $n_{\text{up}}$  and a lower level 1 to calculate the output intensity of the amplified spontaneous emission (ASE). The geometry considered is a long, slender rod of active region, which is completely surrounded by an InP waveguide. The rate equations then are:

$$\frac{dn_{\text{up}}}{dt} = \frac{J}{e} - \frac{n_{\text{up}}}{\tau_{\text{nr}}} - Sg\Delta n - n_{\text{up}}A_{21} \quad (8.15)$$

$$\frac{dS}{dt} = \frac{c}{n_{\text{refr}}} \left( S(g - \alpha)\Delta n + \beta \frac{n_{\text{up}}}{\tau_{\text{spont}}} \right). \quad (8.16)$$

$J$  is the injected current,  $e$  the electron charge,  $\tau_{\text{nr}}$  the non-radiative relaxation time from the upper to the lower laser level,  $S$  the photon flux ( $\text{cm}^{-1}\text{s}^{-1}$ ),  $\Delta n = (n_2 - n_1)$  the population inversion and  $A_{21}$  the Einstein

coefficient for spontaneous emission from state 2 to 1.  $n_{\text{refr}}$  is the refractive index of the mode,  $(g - \alpha)$  is the peak gain,  $\beta$  is the fraction of spontaneous light emitted into the lasing mode and  $\tau_{\text{spont}}$  the spontaneous emission lifetime.

The third and forth term in equation 8.15 are negligible, because operation below threshold is considered, and the spontaneous emission is negligible compared to stimulated emission. In the second equation, we are interested in the second term, which describes the amplified spontaneous emission.

The electromagnetic wave inside the active region rod loses intensity as  $I(x) = I_0 \exp(-\alpha x)$ , where  $x$  is the distance along the ridge as indicated in Fig. 8.2. An infinitesimally short piece of active region  $dx$  will absorb the following amount of energy

$$dI = I_0 e^{-\alpha(l-x)} = I_0 e^{\Gamma g(l-x)} dx, \quad (8.17)$$

where we treated the losses as negative gain  $\alpha = -g$ . The total intensity gained over a device length  $l$  are then calculated as

$$I = I_0 \int_0^l e^{g(l-x)} dx \quad (8.18)$$

$$\vdots \quad (8.19)$$

$$= I_0 \frac{e^{lg} - 1}{g}. \quad (8.20)$$

For QCLs the gain considered is usually the net gain, which is written as  $g - \alpha$ , and will be replaced by  $g(\omega)$  for the rest of this calculation.

The initial spontaneous emission power  $I_0$  is

$$I_0 = \eta_{\text{coll}} \beta h\nu \frac{n_{\text{up}}}{\tau_{\text{rad}}} \frac{N_{\text{p}}}{l} \quad (8.21)$$

where  $n_{\text{up}} = \frac{J}{e} \tau_{\text{up}}$  is the upper state population,  $\tau_{\text{up}}$  the upper state lifetime and  $\tau_{\text{rad}}$  the radiative lifetime. The values of the lifetimes are found from simulations of the active region.  $J/e$  is the injected current density,  $h\nu$  the transition energy and  $l$  the device length. As the rate equations are stated per active region period,  $N_{\text{p}}$  is the number of active region stacks and  $\eta_{\text{coll}}$  is the geometric collection efficiency, depending on the collection

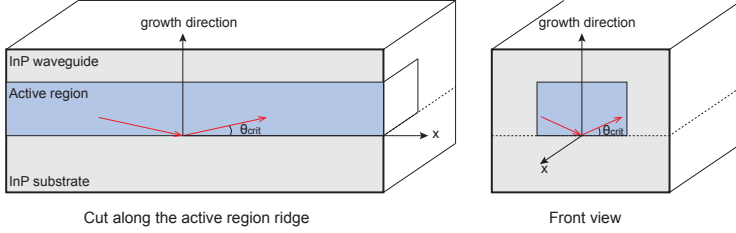


**Figure 8.2:** Schematic view of the active region ridge with the surrounding InP waveguide. The growth direction and the critical angle  $\theta_{\text{crit}}$  are indicated.

optics and detector efficiency.  $\beta$  is the fraction of spontaneous emission in the laser mode and is calculated assuming dipole radiation. Thus  $\beta$  can be calculated as the ratio of the dipole radiation intensity to the total intensity  $I_{\text{dipole}}/I_{\text{tot}}$ . To calculate the fraction of the spontaneous emission in the laser mode, we assume that the active region of the QCL is a long cylinder with a small diameter compared to its length. This approximation is justified as the active region is completely surrounded by a InP waveguide and its length ( $\sim 3 - 6$  mm) is much larger than its height and width ( $\sim 2 - 10$   $\mu\text{m}$ ). Light that is isotropically emitted inside the active region will undergo total internal reflection for angles smaller than  $\theta_{\text{crit}}$  and only light under that angle will be coupled out. Fig. 8.2 schematically shows a front view and a cut along the active region ridge with the surrounding InP waveguide. The critical angle  $\theta_{\text{crit}}$  is indicated together with the growth direction.

We can write

$$\beta = \frac{I_{\text{dipole}}}{I_{\text{tot}}} \quad (8.22)$$

$$= \frac{\int_0^{2\pi} d\varphi \int_0^{\theta_{\text{crit}}} \cos^2 \theta \sin \theta d\theta}{\int_0^{2\pi} d\varphi \int_0^{\pi} \cos^2 \theta \sin \theta d\theta}. \quad (8.23)$$

Finally, the intensity of the spontaneous emission can be described by the following model:

$$I_{\text{spont}} = \eta_{\text{coll}} \beta \cdot \frac{h\nu}{e} \cdot J \cdot N_{\text{p}} \cdot \frac{\tau_{\text{up}}}{\tau_{\text{rad}}} \cdot \frac{e^{l(g-\alpha)} - 1}{l \cdot (g - \alpha)}. \quad (8.24)$$

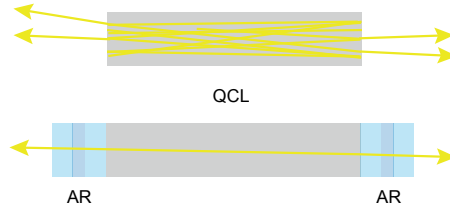


**Figure 8.3:** QCL with as-cleaved facet and internal amplification of the laser light and a QCL with AR coatings on both front and back facet resulting in a single pass gain structure.

### 8.3 Experimental setup and measurements

A standard QCL device has a certain gain as defined by the epi-structure and a certain mirror reflectivity of the cleaved facet that provides a natural cavity. When characterizing a QCL with as-cleaved facets, we will observe amplification and mode selection due to the cavity, when the threshold current is reached. In order to be able to measure only the amplified spontaneous emission inherent to the gain region we have to suppress the cavity effects. This is done preferentially with AR coatings on the front and back facet. The effect of such coatings on the cavity is schematically shown in Fig. 8.3.

#### 8.3.1 QC-SLED

For this investigation, multistack broadband QCL devices provided by Alpes Lasers with a center wavelength of  $6.6 \mu\text{m}$  (sb5021) were used. Devices of 3 mm length were cleaved and mounted epi-structure up onto submounts of the same length, such that both facets could be accessed with collimating optics if necessary.

Fig. 8.4 shows the front (blue) and back (red) facet coatings applied to the QC-SLED. The coatings decreased the mirror reflectivities sufficiently to prevent the QCL from lasing. For more details on the design and challenges of such coatings, please refer to chapters 3 and 4. Once the devices were coated, they were spectrally and electrically characterized.

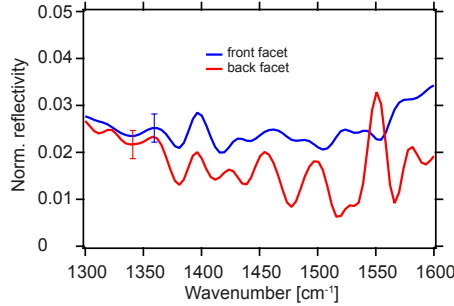


**Figure 8.4:** Data: courtesy of S. Blaser, Alpes Lasers SA. Measurements of the anti-reflection coatings of the front (blue) and back (red) facet of the QC-SLED with error bars.

### 8.3.2 Light-Current-Voltage characteristics of a superluminescent QC-SLED

A very sensitive detector is required to measure the standard light-current-voltage (LIV) characteristics of such a superluminescent device as it will not reach lasing threshold. Thus, a pyroelectric detector (Gentec THZ2I-BL-BNC) was used. The setup had to be optimized to collect as much of the light as possible, that is the geometric collection factor had to be maximized. To ensure such, the devices were measured in a laser box made for the external cavity setup, see chapter 5, where a small collimating lens (Black diamond,  $NA = 0.85$ ) on a piezo-electric xyz-stage was attached. With the lens, the light was focused onto the detector and measured with a lock-in amplifier. In such a way, collection efficiencies of 99 % were obtained. To match the detector response, the device was operated with pulse trains of micro and macro pulses. The macro pulse was set at duty cycle of 50 % at 30 Hz, while the micropulses had a pulse length of 150 ns and different repetition rates to achieve different duty cycles from 10 % to 30 % in steps of 5 %.

The power was then corrected for the responsivity of the detector and the duty cycle and yielded a maximum total output power of  $38 \mu\text{W}$  at 10 % duty cycle. The observed decrease of the intensity with increasing duty cycle is attributed to the heating of the device and the resulting de-



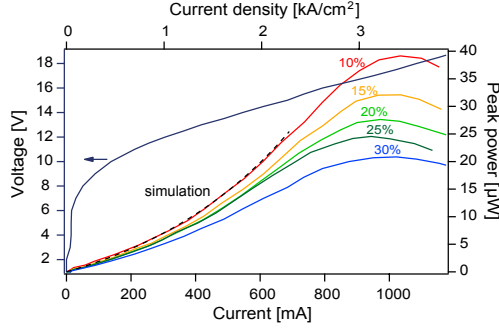


**Figure 8.5:** LIV characteristics at different duty cycles (10%, 15%, 20%, 25% and 30%) measured at 243 K. Maximum output power of  $38 \mu\text{W}$  at 10% duty cycle. Measurement corresponds well with the model for amplified spontaneous emission as presented in eq. 8.24 (dashed line).

crease of the gain. Junction down mounting would significantly improve the thermal behavior.

The measured amplified spontaneous emission of  $38 \mu\text{W}$  at 10 % duty cycle was compared to the radiance of a global, i.e a black body at 1173 K, in the same spectral range ( $1700 \text{ cm}^{-1}$  -  $1350 \text{ cm}^{-1}$ ) and of the same size ( $2.8 \mu\text{m} \times 8.5 \mu\text{m}$ ). With  $63 \text{ nW}$  the radiance of the global is three orders of magnitude lower than the amplified spontaneous emission from the measured device. In combination with the directionality and the size of a QC device, the latter could replace the global for example in a mid-IR microscope increasing the signal strength and reducing the setup size.

The measured values of the amplified spontaneous emission were compared to the simple model described by eq. 8.24. The geometrical collection efficiency was determined by the high numerical aperture lens used ( $\text{NA} = 0.85$ ) and the detector efficiency and was calculated to be  $\eta_{\text{coll}} = 0.99$ .  $\eta_{\text{mode}} = 0.103$  was determined as described in equation 8.23 with the average refractive index of the active region  $n_{\text{active}} = 3.35$  and the substrate  $n_{\text{sub}} = 3.1$ .  $h\nu/e = 0.18 \text{ eV}$  is the transition energy,  $N_p = 35$  the number of repetitions of the active region period and  $l = 3 \text{ mm}$  the device length. The upper state and radiative lifetimes  $\tau_{\text{up}} = 0.5 \text{ ps}$  and  $\tau_{\text{rad}} = 19 \text{ ns}$  were extracted from a density matrix approach [177, 178] based on a similar bandstructure as the one used here [117]. The peak gain

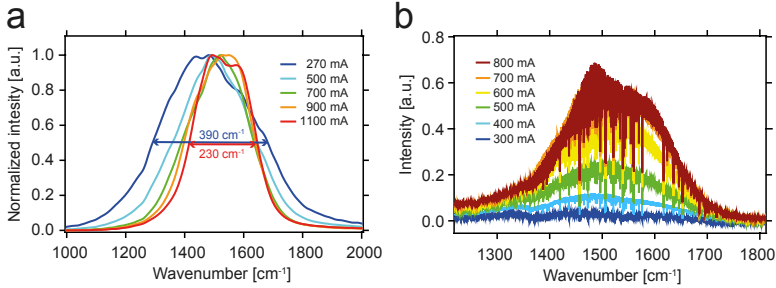


**Figure 8.6:** **a)** Electroluminescence of the double side AR coated QC device at 243 K, at 1 % duty cycle (101 ns, 99 kHz) and  $16 \text{ cm}^{-1}$  resolution, measured at different currents. Flat spectral shape and FWHM of  $230 \text{ cm}^{-1}$  to  $390 \text{ cm}^{-1}$ . **b)** Rapid scan measurements at 243 K, with a resolution of  $0.075 \text{ cm}^{-1}$ . 11 ns pulses with a repetition rate of 10 MHz were applied to prevent the heating of the device during the pulse. The strong absorption features are water absorption lines.

$(g - \alpha)$  is shown in Fig. 8.7. The formula is presented in equation 8.24 and is plotted alongside the LIV measurements in Fig. 8.5 and shows a good agreement with the experiment. The accuracy is reduced by the rough assumptions made to calculate the fraction of spontaneous emission in the laser mode. Nevertheless, the good agreement shows that the measured device did not experience any mode selection due to the Fabry-Pérot cavity and thus represents only the amplified spontaneous emission of the active region.

### 8.3.3 Subthreshold luminescence spectral measurements

All spectral measurements were performed below room temperature (243 K) in pulsed mode, with duty cycles between 1 % and 30 %, and continuous wave (cw) operation mode. All spectral measurements were conducted with a Bruker Vertex 80 fourier-transform interferometer (FTIR) with an external liquid nitrogen cooled HgCdT (MCT) detector.

As mentioned in section 8.2.2, to minimize the contribution of higher order modes in the spectra, low numerical aperture optics have to be employed. Thus the measurements were conducted using the side entrance of the FTIR which has smaller aperture optics than the back entrance.

To fully characterize the device, both low and high resolution luminescence spectra were acquired. The rapid-scan spectra with a resolution of  $16 \text{ cm}^{-1}$  and low duty cycle, 101 ns and 99 kHz, are shown in Fig. 8.6 a). The luminescence spectra exhibit a flat center region of about  $200 \text{ cm}^{-1}$  and a FWHM of more than  $230 \text{ cm}^{-1}$ , showing their suitability as broad-band amplified spontaneous emission sources.

The high resolution spectra were the basis for the Hakki-Paoli gain evaluation and great care has been taken in finding good conditions for the measurements and in aligning the setup. Eq. 8.3 shows that the wavelength of the FP cavity modes depends on the effective refractive index  $n_{\text{eff}}$ , which again depends on the temperature. As QCLs are heating during the duration of one pulse, short pulses have to be applied to prevent the modes from drifting due to the thermal shift and thus smear out the FP fringes in the spectrum. The pulse length was set to 11 ns and the repetition frequency adapted from 10 MHz to 30 MHz for duty cycles of 10 % to 30 %. To resolve all FP cavity fringes, the resolution was set to  $0.075 \text{ cm}^{-1}$  and spectra were taken for currents from 300 mA to 800 mA in steps of 100 mA as shown in Fig. 8.6 b). The strong absorption lines in Fig. 8.6 b) are water absorptions since a short section of the beam path (about 6 cm) was not purged.

### 8.3.4 Gain evaluation

As outlined above, the gain of the device was extracted from the contrast of the measured FP fringes, using the Hakki-Paoli technique [175]. The reflectivities used were the ones measured experimentally on a test wafer coated alongside the chip facets and are shown in Fig. 8.4. The peak gain was evaluated for different currents at a wavelength of  $6.67 \text{ }\mu\text{m}$  ( $1480 \text{ cm}^{-1}$ ) with measured facet reflectivities of 3.8 % and 2.2 % for the back and front facet, respectively, and plotted in Fig. 8.7.

The dashed line (blue) indicates the mirror losses of  $13.9 \text{ cm}^{-1}$  of the device. This also equals the peak gain at which threshold would be reached and lasing would occur. The accuracy of this gain measurement however is limited by the perturbation of the fringes provided by higher order transverse modes as is clearly visible in Fig. 8.1 a). The lower envelope

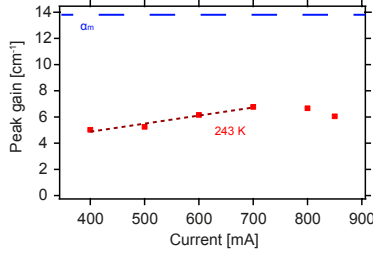


**Figure 8.7:** SOURCE: Riedi *et al.* [180]. Peak gain of  $6.3 \text{ cm}^{-1}$  extracted at  $6.67 \mu\text{m}$  ( $1480 \text{ cm}^{-1}$ ) corresponding to a single pass gain of 1.89.

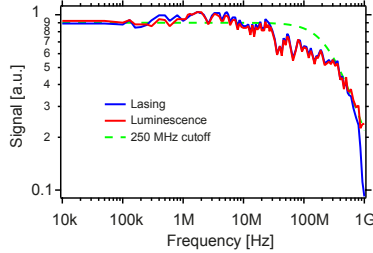


**Figure 8.8:** SOURCE: Riedi *et al.* [180]. Modulation frequency versus signal with a cutoff frequency at 250 MHz.

function of the fringes shows a modulation of the intensity that arises from the higher order lateral modes. Another limiting factor are the inaccuracies in the measurement of the facet reflectivities. In general such a QC device would be optimized for a minimum amount of reflectivity such that the spectrum shows a negligible amount of fringes.

A peak gain value of  $6.3 \text{ cm}^{-1}$  was measured for the device and a single-pass gain of 1.89 was extracted from the data. This result can be compared to the work of Bidaux *et al.* [179] where the gain of single- and multistack QCLs was measured with the interferogram technique of Hofstetter *et al.* [176], see section 8.2.2. Peak gains of  $4 \text{ cm}^{-1}$  were found for both designs which corresponds well to the peak gain of  $6.3 \text{ cm}^{-1}$  found in this work.

### 8.3.5 Modulation of the QC-SLED

Quantum cascade lasers have a very short upper state lifetime ( $\tau_{\text{up}} \approx 0.5$  ps) which limits their efficiency and requires a careful band engineering to create population inversion. By the same thought, such a short lifetime should enable the modulation of such QC SLEDs at very high frequencies. Such a fast modulation could give QC SLEDs another advantage over conventional semiconductor SLEDs in high speed applications [90]. The modulation speed of LEDs is inherently limited by their long lifetimes which are on the order of 1 ns. To confirm this fast modulation behavior of QCLs, we compared the modulation response of a broadband device centered around  $1410 \text{ cm}^{-1}$ , similar to the one measured as a QC SLED, above and below threshold from 10 kHz up to 1 GHz as shown in Fig. 8.8. The fabrication process of these devices was not optimized for RF injection and they exhibit a very large capacitance. Thus the observed cut-off at 250 MHz showed the limitation by the device RC time constant and not by the lifetime. Fig. 8.8 shows the signal vs. modulation frequency for the device in lasing condition (blue) as well as for the luminescence below threshold (red). The green, dashed line shows a simulation of a 250 MHz cutoff. Devices optimized for RF injection and applied low reflectivity AR coatings would make very promising high speed SLEDs for various mid-IR applications.

## 8.4 QCL amplifiers

Double side AR coated devices, as discussed above, can be used in many different ways. One particularly interesting application is the amplification of frequency combs. These coated devices are essentially slabs of gain material that provide single pass gain. Such devices can be used for amplification before micro-resonators or as amplifiers for frequency combs as schematized in Fig. 8.9 a). The light is coupled in through one facet and coupled out through the second one with a precisely determined amplification factor, which depends on the active region gain design and can be measured with the Hakki-Paoli technique as explained in section 8.2.2. QCLs with a center wavelength of  $4.6 \text{ }\mu\text{m}$  (EV1299) were AR coated on both facets and spectrally measured. A set of Hakki-Paoli spectra at dif-

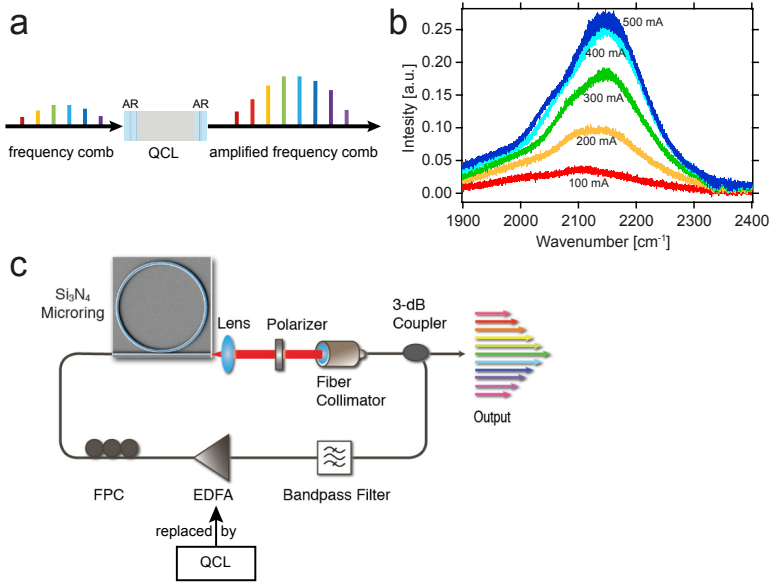


**Figure 8.9:** **a)** Schematics of a double-side AR coated QCL acting as a frequency comb amplifier. The amplification factor versus wavelength depends on the gain region design and can be measured via sub-threshold superluminescence measurements. **b)** Hakki-Paoli spectra of a 3 mm long and  $7.5\ \mu\text{m}$  wide, double-side AR coated QCL around  $4.6\ \mu\text{m}$  center wavelength. The weak Fabry-Pérot fringes indicate a very low reflectivity coating. **c)** SOURCE: based on Johnson *et al.* [181]. Experimental setup for comb generation based on a dual-cavity design with a silicon-nitride micro-resonator. In the experiments conducted in the group of A. Gaeta at Columbia University, New York City, NY, USA, the erbium-doped fiber amplifier (EDFA) is replaced by a QCL acting as an amplifier in the desired wavelength range.

ferent currents is shown in Fig. 8.9 b). The weak Fabry-Pérot fringes indicate very low residual facet reflectivities. Devices of 3 mm length and 5 and  $7.5\ \mu\text{m}$  width yielded peak gains between  $4\ \text{cm}^{-1}$  and  $7.8\ \text{cm}^{-1}$ . Prof. Alexander Gaeta at Columbia University, New York City, NY, United States, conducts experiments with microresonators for frequency comb generation [181, 182, 183]. Fig. 8.9 c) shows a typical experimental setup [181]. For further experiments, QCL amplifiers were provided to replace the erbium-doped fiber amplifier (EDFA) as indicated in Fig. 8.9 c). The amplification factor is calculated by the multiplication of the peak gain with the device length. For example, a device with a peak gain of  $6.3\ \text{cm}^{-1}$  and a length of 3 mm has an amplification factor of 1.89, see Fig. 8.7.

---

### Summary and outlook

The presented work focused on the development and study of broadband quantum cascade lasers in an external cavity configuration. In order to reach this objective, three different topics were investigated.

First, an active region for the wavelength range around  $3.7\text{ }\mu\text{m}$  was designed. The design was based on an existing active region centered around  $3.3\text{ }\mu\text{m}$  such that the two active regions could be combined into a heterogeneously cascaded structure. QCLs of this new design showed good agreement with simulations and achieved peak output powers of 1 W in pulsed mode. It was shown that the two-color design can be tuned over  $556\text{ cm}^{-1}$ , corresponding to 21 % center wavelength tuning around  $3.5\text{ }\mu\text{m}$ , while the individual stacks can be tuned over 11 % of the center wavelength. The tuning range of several other QCLs was tested, including a multistack heterogeneous design around  $5.8\text{ }\mu\text{m}$  and an active region design provided by Alpes Lasers SA at  $8\text{ }\mu\text{m}$ . Center wavelength tunings of 24 % for the multistack and 37 % for the Alpes Lasers SA design were measured. Two heterogeneous cascade designs with 3 and 5 active region designs, respectively, were investigated as well. The three color design showed promising results of an overall tuning over  $500\text{ cm}^{-1}$ , although continuous tuning over the whole gain bandwidth could not be obtained. This was attributed to the insufficient reduction of the facet reflectivity through the AR coating. The five color design, on the other hand, showed a rather inhomogeneous luminescence spectrum which was mirrored in

the narrow tuning range and the tuning limitation of gain starving. An additional challenge was the fabrication of an octave spanning AR coating with reflectivities  $\leq 2\%$ .

Second, dielectric anti-reflection and high-reflectivity coatings were simulated and fabricated and their influence on the lasing behavior of QCLs was examined. As a basis for dielectric coatings with good quality and long-term stability, different materials were tested with respect to both their mechanical as well as optical behavior in the mid-infrared. Anti-reflection coatings with reflectivities  $\leq 1\%$  over broad bandwidths were shown along with dielectric high-reflection coatings acting as partial coatings, with reflectivities from 65 % to nearly perfect mirrors with reflectivities of 98 %.

Finally, it was demonstrated that QCLs can be used as superluminescent QC diodes. The characterized devices exhibited a peak power of 38  $\mu\text{W}$  at 10 % duty cycle, which agrees with a simple model of amplified spontaneous emission and is three orders of magnitude larger than a blackbody of the same size and at global temperature. In addition, it was shown that the luminescence exhibits a flat center region of 200  $\text{cm}^{-1}$  and a peak gain of 6.3  $\text{cm}^{-1}$ . Together with the possibility to modulate the device at high frequencies, such QC SLEDs can be ideal sources for mid-IR microscopy, OCT and process monitoring. Such double-side AR coated devices can also be used as amplifiers for frequency combs.

QCLs have become a mature laser technology over the past years but the field still holds many challenges. The demonstration of an optical frequency comb based on QCLs has opened new possibilities for compact spectroscopy setups and a lot of interest is focused on this area of research. The more mature technique of grating tuned external cavity setups has been advanced further with miniaturized EC-QCL setups with footprints of only a few square centimeters. Such systems are compact and mechanically robust due to MEMS gratings that can be tuned at high frequencies. Together with the broad gain bandwidth of the QCL, such compact modules can be deployed for a wide range of applications including medical care, environmental monitoring, remote detection of hazardous materials and explosives, leak detection and many more.



## Literature

- [1] L. Ciaffoni, R. Grilli, G. Hancock, A. J. Orr-Ewing, R. Peverall, G. A. D. Ritchie, "3.5- $\mu\text{m}$  high-resolution gas sensing employing a LiNbO<sub>3</sub> QPM-DFG waveguide module", *Appl. Phys. B* 94 (2009), 517–525
- [2] A. Bauer, K. Roessner, T. Lehnhardt, M. Kamp, S. Hoefling, L. Worschech, A. Forchel, "Mid-infrared semiconductor heterostructure lasers for gas sensing applications", *Semicond. Sci. Technol.* 26 (2011)
- [3] M. W. Sigrist, "Trace gas monitoring by laser photoacoustic spectroscopy and related techniques (plenary)", *Review of Scientific Instruments* 74 (2003), 486–490
- [4] H. Sauren, D. Bicanic, W. Hillen, H. Jalink, K. v. Asselt, J. Quist, J. Reuss, "Resonant Stark spectrophone as an enhanced trace level ammonia concentration detector: design and performance at CO<sub>2</sub> laser frequencies", *Applied Optics* 29 (1990), 2679–2681
- [5] S. Cristescu, S. Persijn, S. te Lintel Hekkert, F. Harren, "Laser-based systems for trace gas detection in life sciences", *Appl. Phys. B* 92 (2008), 343–349
- [6] D. Nelson, J. Shorter, J. McManus, M. Zahniser, "Sub-part-per-billion detection of nitric oxide in air using a thermoelectrically cooled mid-infrared quantum cascade laser spectrometer", *Appl. Phys. B: Lasers and Optics* 75 (2002), 343–350
- [7] M. B. Pushkarsky, I. G. Dunayevskiy, M. Prasanna, A. G. Tsekoun, R. Go, C. K. N. Patel, "High-sensitivity detection of TNT", *Proceedings of the National Academy of Sciences* 103 (2006), 19630–19634
- [8] M. W. Sigrist, *Air monitoring by spectroscopic techniques*, Wiley, New York (1994)
- [9] F. K. Tittel, D. Richter, A. Fried, "Mid-Infrared Laser Applications in Spectroscopy", in I. T. Sorokina, K. L. Vodopyanov, editors, "Solid-State Mid-Infrared Laser Sources", Springer Berlin Heidelberg, Berlin, Heidelberg, volume 89, pages 458–529 (2003)

- [10] S. P. Davis, M. C. Abrams, J. W. Brault, *Fourier transform spectrometry*, Academic Press, San Diego (2001)
- [11] R. J. Bell, *Introductory Fourier transform spectroscopy*, Academic Press, New York (1972)
- [12] O. Manzardo, H. P. Herzig, C. R. Marxer, N. F. de Rooij, "Miniaturized time-scanning Fourier transform spectrometer based on silicon technology", *Opt. Lett.* 24 (1999), 1705–1707
- [13] P. Werle, "A review of recent advances in semiconductor laser based gas monitors", *Spectrochimica Acta Part A: Molecular and Biomolecular Spectroscopy* 54 (1998), 197–236
- [14] M. B. Frish, M. C. Laderer, R. T. Wainner, A. O. Wright, A. H. Patel, J. Stafford-Evans, J. R. Morency, M. G. Allen, B. D. Green, "The next generation of TD-LAS analyzers", in "Next-Generation Spectroscopic Technologies", Boston, MA (2007), volume 6765, pages 676506–10
- [15] J. A. Gupta, P. J. Barrios, J. Lapointe, G. C. Aers, C. Storey, "Single-mode 2.4  $\mu\text{m}$  InGaAsSb/AlGaAsSb distributed feedback lasers for gas sensing", *Appl. Phys. Lett.* 95 (2009), 041104
- [16] P. Kluczynski, S. Lundqvist, S. Belahsene, Y. Rouillard, "Tunable-diode-laser spectroscopy of  $\text{C}_2\text{H}_2$  using a 3.03  $\mu\text{m}$  GaInAsSb/AlGaInAsSb distributed-feedback laser", *Opt. Lett.* 34 (2009), 3767
- [17] M. W. Sigrist, "Mid-infrared laser-spectroscopic sensing of chemical species", *J Adv Res* 6 (2015), 529–533
- [18] W. Demtröder, *Laser spectroscopy*, Springer, Berlin (2008)
- [19] K. Wörle, F. Seichter, A. Wilk, C. Armacost, T. Day, M. Godejohann, U. Wachter, J. Vogt, P. Radermacher, B. Mizaikoff, "Breath Analysis with Broadly Tunable Quantum Cascade Lasers", *Anal. Chem.* 85 (2013), 2697–2702
- [20] J. Faist, F. Capasso, D. L. Sivco, L. Hutchinson, C. Sirtori, S. N. G. Chu, A. Y. Cho, "Quantum cascade laser: temperature dependence of the performance characteristics and high  $T_0$  operation", *Appl. Phys. Lett.* 65 (1994), 2901–2903
- [21] R. A. Dweik, editor, *Journal of Breath Research Special issue on exhaled breath analysis: from sensors to devices and applications*, volume 5, IOP Publishing (2011)
- [22] H. Dahnke, D. Kleine, P. Hering, M. Mürtz, "Real-time monitoring of ethane in human breath using mid-infrared cavity leak-out spectroscopy", *Appl. Phys. B: Lasers and Optics* 72 (2001), 971–975
- [23] K. Skeldon, L. McMillan, C. Wyse, S. Monk, G. Gibson, C. Patterson, T. France, C. Longbottom, M. Padgett, "Application of laser spectroscopy for measurement of exhaled ethane in patients with lung cancer", *Respiratory Medicine* 100 (2006), 300–306

- 
- [24] M. R. McCurdy, Y. Bakhirkin, G. Wysocki, R. Lewicki, F. K. Tittel, "Recent advances of laser-spectroscopy-based techniques for applications in breath analysis", *Journal of Breath Research* 1 (2007), 014001
- [25] C. Wang, A. B. Surampudi, "An acetone breath analyzer using cavity ring-down spectroscopy: an initial test with human subjects under various situations", *Measurement Science and Technology* 19 (2008), 105604
- [26] R. Bartlome, M. W. Sigrist, "Laser-based human breath analysis: D/H isotope ratio increase following heavy water intake", *Opt. Lett.* 34 (2009), 866–868
- [27] K. M.-C. Hans, S. Müller, M. W. Sigrist, "Infrared attenuated total reflection (IR-ATR) spectroscopy for detecting drugs in human saliva", *Drug Test. Analysis* 4 (2012), 420–429
- [28] K. M.-C. Hans, M. Müller, T. Petrosyan, M. W. Sigrist, "Infrared detection of cocaine and street cocaine in saliva with a one-step extraction", *Anal. Methods* 6 (2014), 666–673
- [29] S. Blaser, D. Hofstetter, M. Beck, J. Faist, "Free-space optical data link using Peltier-cooled quantum cascade laser", *Electron. Lett.* 37 (2001), 778–780
- [30] R. Martini, C. Gmachl, J. Falciglia, F. Curti, C. Bethea, F. Capasso, E. Whittaker, R. Paiella, A. Tredicucci, A. Hutchinson, D. Sivco, A. Cho, "High-speed modulation and free-space optical audio/video transmission using quantum cascade lasers", *Electronics Letters* 37 (2001), 191–193
- [31] F. Capasso, "Quantum Cascade Lasers: past, present and future", *IQCLSW 2008* (2008), 1–49
- [32] C. Roller, K. Namjou, J. D. Jeffers, M. Camp, A. Mock, P. J. McCann, J. Grego, "Nitric oxide breath testing by tunable-diode laser absorption spectroscopy: application in monitoring respiratory inflammation", *Applied Optics* 41 (2002), 6018
- [33] M. Horstjann, Y. A. Bakhirkin, A. A. Kosterev, R. F. Curl, F. K. Tittel, C. M. Wong, C. J. Hill, R. Q. Yang, "Formaldehyde sensor using interband cascade laser based quartz-enhanced photoacoustic spectroscopy", *Appl. Phys. B* 79 (2004), 799–803
- [34] Y. A. Bakhirkin, A. A. Kosterev, C. Roller, R. F. Curl, F. K. Tittel, "Mid-infrared quantum cascade laser based off-axis integrated cavity output spectroscopy for biogenic nitric oxide detection", *Applied Optics* 43 (2004), 2257–2266
- [35] C. Bauer, P. Geiser, J. Burgmeier, G. Holl, W. Schade, "Pulsed laser surface fragmentation and mid-infrared laser spectroscopy for remote detection of explosives", *Appl. Phys. B* 85 (2006), 251–256
- [36] B. G. Lee, J. Kinsky, A. K. Goyal, C. Pflügl, L. Diehl, M. A. Belkin, A. Sanchez, F. Capasso, "Beam combining of quantum cascade laser arrays", *Opt. Express* 17 (2009), 16216
- [37] D. Weidmann, W. J. Reburn, K. M. Smith, "Retrieval of atmospheric ozone profiles from an infrared quantum cascade laser heterodyne radiometer: results and analysis", *Applied Optics* 46 (2007), 7162

- [38] R. N. Hall, G. E. Fenner, J. D. Kingsley, T. J. Soltys, R. O. Carlson, "Coherent light emission from GaAs junctions", *Phys. Rev. Lett.* 9 (1962), 366–368
- [39] M. I. Nathan, W. P. Dumke, G. Burns, F. H. D. Jr, G. Lasher, "Stimulated emission of radiation from GaAs p-n junctions", *Appl. Phys. Lett.* 1 (1962), 62–64
- [40] N. J. Holonyak, S. F. Bevacqua, "Coherent (visible) light emission from Ga(As<sub>1-x</sub>P<sub>x</sub>) junctions", *Appl. Phys. Lett.* 1 (1962), 82–83
- [41] L. A. Coldren, S. W. Corzine, M. L. Mashanovitch, *Diode Lasers and Photonic Integrated Circuits*, Wiley, New York, 2 edition (1995)
- [42] F. Bugge, G. Erbert, J. Fricke, S. Gramlich, R. Staske, H. Wenzel, U. Zeimer, M. Weyers, "12 W continuous-wave diode lasers at 1120 nm with InGaAs quantum wells", *Appl. Phys. Lett.* 79 (2001), 1965–1967
- [43] E. Wintner, E. P. Ippen, "Nonlinear carrier dynamics in Ga<sub>x</sub>In<sub>1-x</sub>As<sub>y</sub>P<sub>1-y</sub> compounds", *Appl. Phys. Lett.* 44 (1984), 999–1001
- [44] M. Takeshima, "Effect of Auger recombination on laser operation in Ga<sub>1-x</sub>Al<sub>x</sub>As", *J. Appl. Phys.* 58 (1985), 3846–3850
- [45] J. R. Meyer, C. L. Felix, W. W. Bewley, I. Vurgaftman, E. H. Aifer, L. J. Olafsen, J. R. Lindle, C. A. Hoffman, M.-J. Yang, B. R. Bennett, B. V. Shanabrook, H. Lee, C.-H. Lin, S. S. Pei, R. H. Miles, "Auger coefficients in type-II InAs/Ga<sub>1-x</sub>In<sub>x</sub>Sb quantum wells", *Appl. Phys. Lett.* 73 (1998), 2857–2859
- [46] J. Jewell, J. Harbison, A. Scherer, Y. Lee, L. Florez, "Vertical-cavity surface-emitting lasers: Design, growth, fabrication, characterization", *IEEE Journal of Quantum Electronics* 27 (1991), 1332–1346
- [47] W. W. Bewley, C. L. Canedy, C. S. Kim, M. Kim, C. D. Merritt, J. Abell, I. Vurgaftman, J. R. Meyer, "High-power room-temperature continuous-wave mid-infrared interband cascade lasers", *Opt. Express* 20 (2012), 20894–20901
- [48] L. Diehl, D. Bour, S. Corzine, J. Zhu, G. Höfler, M. Loncar, M. Troccoli, F. Capasso, "High-power quantum cascade lasers grown by low-pressure metal organic vapor-phase epitaxy operating in continuous wave above 400K", *Appl. Phys. Lett.* 88 (2006), 201115
- [49] J. Faist, F. Capasso, D. L. Sivco, C. Sirtori, A. L. Hutchinson, A. Y. Cho, "Quantum Cascade Laser", *Science* 264 (1994), 553–556
- [50] R. Kazarinov, R. Suris, "Possibility of the amplification of electromagnetic waves in a semiconductor with a superlattice", *Sov. Phys. Semicond.* 5 (1971), 707–709
- [51] A. Bismuto, M. Beck, J. Faist, "High power Sb-free quantum cascade laser emitting at 3.3  $\mu$ m above 350 K", *Appl. Phys. Lett.* 98 (2011), 191104–3
- [52] D. G. Revin, J. W. Cockburn, M. J. Steer, R. J. Airey, M. Hopkinson, A. B. Krysa, L. R. Wilson, S. Menzel, "InGaAs/AlAsSb/InP strain compensated quantum cascade lasers", *Appl. Phys. Lett.* 90 (2007), 151105

- 
- [53] N. Bandyopadhyay, Y. Bai, S. Tsao, S. Nida, S. Slivken, M. Razeghi, "Room temperature continuous wave operation of  $\lambda \approx 3 - 3.2 \mu\text{m}$  quantum cascade lasers", *Appl. Phys. Lett.* 101 (2012), 241110–4
  - [54] N. Bandyopadhyay, S. Slivken, Y. Bai, M. Razeghi, "High power, continuous wave, room temperature operation of  $\lambda \approx 3.4 \mu\text{m}$  and  $\lambda \approx 3.55 \mu\text{m}$  InP-based quantum cascade lasers", *Appl. Phys. Lett.* 100 (2012), 212104–4
  - [55] B. G. Lee, H. A. Zhang, C. Pfluegl, L. Diehl, M. A. Belkin, M. Fischer, A. Wittmann, J. Faist, F. Capasso, "Broadband Distributed-Feedback Quantum Cascade Laser Array Operating From 8.0 to 9.8  $\mu\text{m}$ ", *IEEE Photonic Tech L* 21 (2009), 914–916
  - [56] A. Wittmann, Y. Bonetti, M. Fischer, J. Faist, S. Blaser, E. Gini, "Distributed-Feedback Quantum-Cascade Lasers at 9  $\mu\text{m}$  Operating in Continuous Wave Up to 423 K", *IEEE Photonic Tech L* 21 (2009), 814–816
  - [57] J. Faist, C. F. Gmachl, F. Capasso, C. Sirtori, D. L. Sivco, J. N. Baillargeon, A. Y. Cho, "Distributed feedback quantum cascade lasers", *Appl. Phys. Lett.* 70 (1997), 2670–2672
  - [58] M. F. Witinski, R. Blanchard, C. Pfluegl, L. Diehl, B. Li, B. Pancy, D. Vakhshoori, F. Capasso, "Monolithic DFB QCL array aims at handheld IR spectral analysis", *LASER FOCUS WORLD* 51 (2015), 36–39
  - [59] G. Wysocki, R. F. Curl, F. K. Tittel, R. Maulini, J. M. Bulliard, J. Faist, "Widely tunable mode-hop free external cavity quantum cascade laser for high resolution spectroscopic applications", *Appl. Phys. B* 81 (2005), 769–777
  - [60] B. G. Lee, M. A. Belkin, R. Audet, J. MacArthur, L. Diehl, C. Pflügl, F. Capasso, D. C. Oakley, D. Chapman, A. Napoleone, D. Bour, S. Corzine, G. Höfler, J. Faist, "Widely tunable single-mode quantum cascade laser source for mid-infrared spectroscopy", *Appl. Phys. Lett.* 91 (2007), 231101–3
  - [61] E. Mujagić, C. Schwarzer, Y. Yao, J. Chen, C. F. Gmachl, G. Strasser, "Two-dimensional broadband distributed-feedback quantum cascade laser arrays", *Appl. Phys. Lett.* 98 (2011), 141101
  - [62] P. Jouy, C. Bonzon, J. Wolf, E. Gini, M. Beck, J. Faist, "Surface emitting multi-wavelength array of single frequency quantum cascade lasers", *Appl. Phys. Lett.* 106 (2015), 071104
  - [63] Y. Bidaux, A. Bismuto, C. Tardy, R. Terazzi, T. Gresch, S. Blaser, A. Muller, J. Faist, "Extended and quasi-continuous tuning of quantum cascade lasers using superstructure gratings and integrated heaters", *Appl. Phys. Lett.* 107 (2015), 221108
  - [64] V. Jayaraman, Z. M. Chuang, L. A. Coldren, "Theory, design, and performance of extended tuning range semiconductor lasers with sampled gratings", *IEEE Journal of Quantum Electronics* 29 (1993), 1824–1834
  - [65] S. Slivken, N. Bandyopadhyay, S. Tsao, S. Nida, Y. Bai, Q. Y. Lu, M. Razeghi, "Sampled grating, distributed feedback quantum cascade lasers with broad tunability and continuous operation at room temperature", *Appl. Phys. Lett.* 100 (2012), 261112

- [66] T. S. Mansuripur, S. Menzel, R. Blanchard, L. Diehl, C. Pflügl, Y. Huang, J.-H. Ryou, R. D. Dupuis, M. Loncar, F. Capasso, "Widely tunable mid-infrared quantum cascade lasers using sampled grating reflectors", *Optics Express* 20 (2012), 23339
- [67] S. Slivken, N. Bandyopadhyay, Y. Bai, Q. Y. Lu, M. Razeghi, "Extended electrical tuning of quantum cascade lasers with digital concatenated gratings", *Appl. Phys. Lett.* 103 (2013), 231110
- [68] S. Kalchmair, R. Blanchard, T. S. Mansuripur, G.-M. de Naurois, C. Pfluegl, M. F. Witinski, L. Diehl, F. Capasso, M. Loncar, "High tuning stability of sampled grating quantum cascade lasers", *Optics Express* 23 (2015), 15734
- [69] T. Udem, R. Holzwarth, T. W. Hänsch, "Optical frequency metrology", *Nature* 416 (2002), 233–237
- [70] I. Coddington, W. C. Swann, N. R. Newbury, "Coherent dual-comb spectroscopy at high signal-to-noise ratio", *Phys. Rev. A* 82 (2010), 043817
- [71] S. A. Diddams, D. J. Jones, J. Ye, S. T. Cundiff, J. L. Hall, J. K. Ranka, R. S. Windeler, R. Holzwarth, T. Udem, T. W. Hänsch, "Direct Link between Microwave and Optical Frequencies with a 300 THz Femtosecond Laser Comb", *Physical Review Letters* 84 (2000), 5102–5105
- [72] G. Villares, A. Hugi, S. Blaser, J. Faist, "Dual-comb spectroscopy based on quantum-cascade-laser frequency combs", *Nat. Commun.* 5 (2014), 5192
- [73] A. Hugi, R. Maulini, J. Faist, "External cavity quantum cascade laser", *Semicond. Sci. Technol.* 25 (2010), 083001
- [74] R. Maulini, A. Mohan, M. Giovannini, J. Faist, E. Gini, "External cavity quantum-cascade laser tunable from 8.2 to 10.4  $\mu\text{m}$  using a gain element with a heterogeneous cascade", *Appl. Phys. Lett.* 88 (2006), 201113
- [75] Y. Yao, T. Tsai, X. Wang, G. Wysocki, C. F. Gmachl, "Broadband Quantum Cascade Lasers Based on Strongly-coupled Transitions with an External Cavity Tuning Range over 340  $\text{cm}^{-1}$ ", in "CLEO:2011 - Laser Applications to Photonic Applications", Optical Society of America (2011), OSA Technical Digest (CD), page CMQ3
- [76] S. Riedi, A. Hugi, A. Bismuto, M. Beck, J. Faist, "Broadband external cavity tuning in the 3–4  $\mu\text{m}$  window", *Appl. Phys. Lett.* 103 (2013), 031108
- [77] M. G. Littman, "Single-mode operation of grazing-incidence pulsed dye laser", *Opt. Lett.* 3 (1978), 138
- [78] M. Fleming, A. Mooradian, "Spectral characteristics of external-cavity controlled semiconductor lasers", *IEEE Journal of Quantum Electronics* 17 (1981), 44–59
- [79] K. Liu, M. G. Littman, "Novel geometry for single-mode scanning of tunable lasers", *Opt. Lett.* 6 (1981), 117
- [80] K. C. Harvey, C. J. Myatt, "External-cavity diode laser using a grazing-incidence diffraction grating", *Opt. Lett.* 16 (1991), 910

- 
- [81] L. Ricci, M. Weidemüller, T. Esslinger, A. Hemmerich, C. Zimmermann, V. Vuletic, W. König, T. W. Hänsch, "A compact grating-stabilized diode laser system for atomic physics", *Optics Communications* 117 (1995), 541–549
  - [82] C. J. Hawthorn, K. P. Weber, R. E. Scholten, "Littrow configuration tunable external cavity diode laser with fixed direction output beam", *Review of Scientific Instruments* 72 (2001), 4477–4479
  - [83] Q.-V. Nguyen, T. Day, R. W. Dibble, "High-resolution oxygen absorption spectrum obtained with an external-cavity continuously tunable diode laser", *Opt. Lett.* 19 (1994), 2134
  - [84] G. P. Luo, C. Peng, H. Q. Le, S. S. Pei, W.-Y. Hwang, B. Ishaug, J. Um, J. N. Bailargeon, C.-H. Lin, "Grating-tuned external-cavity quantum-cascade semiconductor lasers", *Appl. Phys. Lett.* 78 (2001), 2834–2836
  - [85] R. Maulini, M. Beck, J. Faist, E. Gini, "Broadband tuning of external cavity bound-to-continuum quantum-cascade lasers", *Appl. Phys. Lett.* 84 (2004), 1659–1661
  - [86] R. Maulini, D. A. Yarekha, J.-M. Bulliard, M. Giovannini, J. Faist, E. Gini, "Continuous-wave operation of a broadly tunable thermoelectrically cooled external cavity quantum-cascade laser", *Opt. Lett.* 30 (2005), 2584–2586
  - [87] C. Peng, G. Luo, H. Q. Le, "Broadband, Continuous, and Fine-Tune Properties of External-Cavity Thermoelectric-Stabilized Mid-infrared Quantum-Cascade Lasers", *Applied Optics* 42 (2003), 4877
  - [88] J. W. Goodman, "Some fundamental properties of speckle\*", *J. Opt. Soc. Am., JOSA* 66 (1976), 1145–1150
  - [89] B. Dingel, S. Kawata, "Speckle-free image in a laser-diode microscope by using the optical feedback effect", *Opt. Lett., OL* 18 (1993), 549–551
  - [90] D. Childs, K. Kennedy, D. Revin, J. Cockburn, K. Groom, R. Hogg, I. Rehman, S. Matcher, "A rapid Swept-Source Mid-Infrared Laser", in "Proceedings of UK Semiconductors 2014 & UK Nitrides Consortium Summer Meeting", (2014)
  - [91] C. S. Colley, J. C. Hebden, D. T. Delpy, A. D. Cambrey, R. A. Brown, E. A. Zibik, W. H. Ng, L. R. Wilson, J. W. Cockburn, "Mid-infrared optical coherence tomography", *Rev. Sci. Instrum.* 78 (2007), 123108
  - [92] J. M. Schmitt, S. H. Xiang, K. M. Yung, "Speckle in optical coherence tomography", *J. Biomed. Opt* 4 (1999), 95–105
  - [93] J. M. Schmitt, "Optical coherence tomography (OCT): a review", *IEEE Journal of Selected Topics in Quantum Electronics* 5 (1999), 1205–1215
  - [94] M. J. Süess, P. M. Hundt, B. Tuzson, S. Riedi, J. M. Wolf, R. Peretti, M. Beck, H. Looser, L. Emmenegger, J. Faist, "Dual-Section DFB-QCLs for Multi-Species Trace Gas Analysis", *Photonics* 3 (2016), 24
  - [95] J. Faist, *Quantum Cascade Lasers*, Oxford University Press, Oxford, UK, 1 edition (2013)

- [96] A. Hugi, "Single-mode and Comb Operation of Broadband Quantum Cascade Lasers", Dissertation, ETH Zürich, Zürich, Switzerland (2013), diss. ETH No. 21138
- [97] L. Esaki, R. Tsu, "Superlattice and Negative Differential Conductivity in Semiconductors", IBM Journal of Research and Development 14 (1970), 61–65
- [98] A. Y. Cho, "Film Deposition by Molecular-Beam Techniques", Journal of Vacuum Science and Technology 8 (1971), S31–S38
- [99] A. Y. Cho, J. R. Arthur, "Molecular beam epitaxy", Progress in Solid State Chemistry 10 (1975), 157–191
- [100] M. Beck, D. Hofstetter, T. Aellen, J. Faist, U. Oesterle, M. Illegems, E. Gini, H. Melchior, "Continuous Wave Operation of a Mid-Infrared Semiconductor Laser at Room Temperature", Science 295 (2002), 301–305
- [101] R. Köhler, A. Tredicucci, F. Beltram, H. E. Beere, E. H. Linfield, A. G. Davies, D. A. Ritchie, R. C. Iotti, F. Rossi, "Terahertz semiconductor-heterostructure laser", Nature 417 (2002), 156–159
- [102] Q. Y. Lu, Y. Bai, N. Bandyopadhyay, S. Slivken, M. Razeghi, "2.4 W room temperature continuous wave operation of distributed feedback quantum cascade lasers", Appl. Phys. Lett. 98 (2011), 181106
- [103] Y. Bai, N. Bandyopadhyay, S. Tsao, S. Slivken, M. Razeghi, "Room temperature quantum cascade lasers with 27% wall plug efficiency", Appl. Phys. Lett. 98 (2011), 181102
- [104] J. M. Wolf, S. Riedi, M. J. Süess, M. Beck, J. Faist, "3.36  $\mu\text{m}$  single-mode quantum cascade laser with a dissipation below 250 mW", Optics Express 24 (2016), 662
- [105] A. Hugi, R. Terazzi, Y. Bonetti, A. Wittmann, M. Fischer, M. Beck, J. Faist, E. Gini, "External cavity quantum cascade laser tunable from 7.6 to 11.4  $\mu\text{m}$ ", Appl. Phys. Lett. 95 (2009), 061103–3
- [106] A. Hugi, G. Villares, S. Blaser, H. C. Liu, J. Faist, "Mid-infrared frequency comb based on a quantum cascade laser", Nature 492 (2012), 229–233
- [107] M. Rösch, G. Scalari, M. Beck, J. Faist, "Octave-spanning semiconductor laser", Nat. Photon. 9 (2015), 42–47
- [108] J. Faist, M. Beck, T. Aellen, E. Gini, "Quantum-cascade lasers based on a bound-to-continuum transition", Appl. Phys. Lett. 78 (2001), 147–149
- [109] D. Hofstetter, M. Beck, T. Aellen, J. Faist, U. Oesterle, M. Illegems, E. Gini, H. Melchior, "Continuous wave operation of a 9.3  $\mu\text{m}$  quantum cascade laser on a Peltier cooler", Appl. Phys. Lett. 78 (2001), 1964–1966
- [110] J. Faist, D. Hofstetter, M. Beck, T. Aellen, M. Rochat, S. Blaser, "Bound-to-continuum and two-phonon resonance, quantum-cascade lasers for high duty cycle, high-temperature operation", Appl. Phys. Lett. 38 (2002), 533–546



- 
- [111] A. Lyakh, C. Pflügl, L. Diehl, Q. J. Wang, F. Capasso, X. J. Wang, J. Y. Fan, T. Tanbun-Ek, R. Maulini, A. Tsekoun, R. Go, C. K. N. Patel, "1.6 W high wall plug efficiency, continuous-wave room temperature quantum cascade laser emitting at  $4.6\ \mu\text{m}$ ", *Appl. Phys. Lett.* 92 (2008), 111110–3
  - [112] A. Lyakh, R. Maulini, A. Tsekoun, R. Go, C. Pflügl, L. Diehl, Q. J. Wang, F. Capasso, C. K. N. Patel, "3 W continuous-wave room temperature single-facet emission from quantum cascade lasers based on nonresonant extraction design approach", *Appl. Phys. Lett.* 95 (2009), 141113–3
  - [113] A. Lyakh, R. Maulini, A. G. Tsekoun, C. K. N. Patel, "Progress in high-performance quantum cascade lasers", *Optical Engineering* 49 (2010), 111105
  - [114] A. Lyakh, R. Maulini, A. Tsekoun, R. Go, C. K. N. Patel, "Multiwatt long wavelength quantum cascade lasers based on high strain composition with 70% injection efficiency", *Opt. Express* 20 (2012), 24272–24279
  - [115] R. Maulini, A. Lyakh, A. Tsekoun, C. K. N. Patel, " $\lambda \sim 7.1\ \mu\text{m}$  quantum cascade lasers with 19% wall-plug efficiency at room temperature", *Optics Express* 19 (2011), 17203–17211
  - [116] A. Tredicucci, F. Capasso, C. F. Gmachl, D. L. Sivco, A. L. Hutchinson, A. Y. Cho, "High performance interminiband quantum cascade lasers with graded superlattices", *Appl. Phys. Lett.* 73 (1998), 2101–2103
  - [117] A. Wittmann, Y. Bonetti, J. Faist, E. Gini, M. Giovannini, "Intersubband linewidths in quantum cascade laser designs", *Appl. Phys. Lett.* 93 (2008), 141103–3
  - [118] C. F. Gmachl, H. Y. Hwang, R. Paiella, D. L. Sivco, J. N. Baillargeon, F. Capasso, A. Y. Cho, "Quantum cascade lasers with low-loss chalcogenide lateral waveguides", *IEEE Photonic Tech L* 13 (2001), 182–184
  - [119] C. F. Gmachl, D. L. Sivco, R. Colombelli, F. Capasso, A. Y. Cho, "Ultra-broadband semiconductor laser", *Nature* 415 (2002), 883–887
  - [120] M. Beck, J. Faist, U. Oesterle, M. Illegems, E. Gini, H. Melchior, "Buried heterostructure quantum cascade lasers with a large optical cavity waveguide", *IEEE Photonics Technology Letters* 12 (2000), 1450–1452
  - [121] M. B. Panish, "Molecular Beam Epitaxy", *Science* 208 (1980), 916–922
  - [122] D. Garbuzov, H. Lee, V. Khalfin, R. Martinelli, J. Connolly, G. Belenky, "2.3 – 2.7  $\mu\text{m}$  room temperature CW operation of InGaAsSb-AlGaAsSb broad waveguide SCH-QW diode lasers", *IEEE Photonics Technology Letters* 11 (1999), 794–796
  - [123] A. Bismuto, "Mid-Infrared quantum cascade lasers: active medium and waveguide engineering", Dissertation, ETH Zürich, Zürich, Switzerland (2011), diss. ETH No. 19924
  - [124] E. Palik, *Handbook of Optical Constants of Solids*, Volume 1, v. 1, Elsevier Science (2012)

- [125] E. Palik, *Handbook of Optical Constants of Solids*, Volume 2, v. 2, Elsevier Science (2012)
- [126] J. Connolly, B. diBenedetto, R. Donadio, "Specifications Of Raytran Material", in "Contemporary Optical Systems and Components Specifications", (1979), volume 0181, pages 141–144
- [127] B. Tatian, "Fitting refractive-index data with the Sellmeier dispersion formula", *Appl. Opt.*, AO 23 (1984), 4477–4485
- [128] G. Hass, C. D. Salzberg, "Optical Properties of Silicon Monoxide in the Wavelength Region from 0.24 to 14.0 Microns", *J. Opt. Soc. Am.*, JOSA 44 (1954), 181–187
- [129] J. Kischkat, S. Peters, B. Gruska, M. Semtsiv, M. Chashnikova, M. Klinkmüller, O. Fedosenko, S. Machulik, A. Aleksandrova, G. Monastyrskyi, Y. Flores, W. T. Masselink, "Mid-infrared optical properties of thin films of aluminum oxide, titanium dioxide, silicon dioxide, aluminum nitride, and silicon nitride", *Appl. Opt.*, AO 51 (2012), 6789–6798
- [130] P. Yeh, *Optical Waves in Layered Media*, Wiley Series in Pure and Applied Optics, John Wiley & Sons, Inc., Hoboken, New Jersey, USA, 10 edition (2005)
- [131] C. K. Carniglia, J. H. Apfel, "Maximum reflectance of multilayer dielectric mirrors in the presence of slight absorption", *Journal of the Optical Society of America* 70 (1980), 523
- [132] S. A. Diddams, "The evolving optical frequency comb", *Journal of the Optical Society of America B* 27 (2010), B51–B62
- [133] G. Scalari, M. Rösch, M. Beck, J. Faist, "Octave-spanning semiconductor laser for frequency comb applications", *SPIE Newsroom* (2015)
- [134] G. Villares, J. Faist, "Quantum cascade laser combs: effects of modulation and dispersion", *Optics Express* 23 (2015), 1651
- [135] F. Cappelli, G. Villares, S. Riedi, J. Faist, "Intrinsic linewidth of quantum cascade laser frequency combs", *Optica* 2 (2015), 836
- [136] P. Friedli, H. Sigg, B. Hinkov, A. Hugi, S. Riedi, M. Beck, J. Faist, "Four-wave mixing in a quantum cascade laser amplifier", *Appl. Phys. Lett.* 102 (2013), 222104
- [137] G. Villares, S. Riedi, J. Wolf, D. Kazakov, M. J. Süess, M. Beck, J. Faist, "Dispersion engineering of Quantum Cascade Lasers frequency combs", *arXiv:1509.08856 [physics]* (2015), arXiv: 1509.08856
- [138] R. Szpöcs, A. Köhzi-Kis, S. Lakó, P. Apai, A. P. Kovács, G. DeBell, L. Mott, A. W. Louderback, A. V. Tikhonravov, M. K. Trubetskov, "Negative dispersion mirrors for dispersion control in femtosecond lasers: chirped dielectric mirrors and multi-cavity Gires-Tournois interferometers", *Appl. Phys. B* 70 (2000), S51–S57
- [139] D. Burghoff, T.-Y. Kao, N. Han, C. W. I. Chan, X. Cai, Y. Yang, D. J. Hayton, J.-R. Gao, J. L. Reno, Q. Hu, "Terahertz laser frequency combs", *Nature Photonics* 8 (2014), 462–467

- 
- [140] G. Totschnig, F. Winter, V. Pustogov, J. Faist, A. Müller, "Mid-infrared external-cavity quantum-cascade laser", *Opt. Lett.* 27 (2002), 1788–1790
  - [141] G. Luo, C. Peng, H. Le, S.-S. Pei, H. Lee, W.-Y. Hwang, B. Ishaug, J. Zheng, "Broadly wavelength-tunable external cavity, mid-infrared quantum cascade lasers", *IEEE Journal of Quantum Electronics* 38 (2002), 486–494
  - [142] R. Maulini, I. Dunayevskiy, A. Lyakh, A. Tsekoun, C. Patel, L. Diehl, C. Pflugl, F. Capasso, "Widely tunable high-power external cavity quantum cascade laser operating in continuous-wave at room temperature", *Electronics Letters* 45 (2009), 107–108
  - [143] A. Wittmann, A. Hugi, E. Gini, N. Hoyler, J. Faist, "Heterogeneous High-Performance Quantum-Cascade Laser Sources for Broad-Band Tuning", *IEEE Journal of Quantum Electronics* 44 (2008), 1083–1088
  - [144] T. Dougakiuchi, K. Fujita, N. Akikusa, A. Sugiyama, T. Edamura, M. Yamanishi, "Broadband Tuning of External Cavity Dual-Upper-State Quantum-Cascade Lasers in Continuous Wave Operation", *Appl. Phys. Express* 4 (2011), 102101
  - [145] R. Ostendorf, L. Butschek, A. Merten, J. Grahmann, J. Jarvis, S. Hugger, F. Fuchs, J. Wagner, "Real-time spectroscopic sensing using a widely tunable external cavity-QCL with MOEMS diffraction grating", in "Quantum Sensing and Nano Electronics and Photonics XIII", (2016), volume 9755, pages 975507–8
  - [146] T. Tsai, G. Wysocki, "External-cavity quantum cascade lasers with fast wavelength scanning", *Appl. Phys. B* 100 (2010), 243–251
  - [147] S. Hugger, F. Fuchs, J. Jarvis, M. Kinzer, Q. K. Yang, R. Driad, R. Aidam, J. Wagner, "Broadband-tunable external-cavity quantum cascade lasers for the spectroscopic detection of hazardous substances", in "Quantum Sensing and Nanophotonic Devices X", (2013), volume 8631, pages 86312I–13
  - [148] A. Lyakh, R. Barron-Jimenez, I. Dunayevskiy, R. Go, C. K. N. Patel, "External cavity quantum cascade lasers with ultra rapid acousto-optic tuning", *Appl. Phys. Lett.* 106 (2015), 141101
  - [149] R. Ostendorf, L. Butschek, S. Hugger, F. Fuchs, Q. Yang, J. Jarvis, C. Schilling, M. Rattunde, A. Merten, J. Grahmann, D. Boskovic, T. Tybussek, K. Rieblinger, J. Wagner, "Recent Advances and Applications of External Cavity-QCLs towards Hyperspectral Imaging for Standoff Detection and Real-Time Spectroscopic Sensing of Chemicals", *Photonics* 3 (2016), 28
  - [150] J. Grahmann, A. Merten, R. Ostendorf, M. Fontenot, D. Bleh, H. Schenk, H.-J. Wagner, "Tunable External Cavity Quantum Cascade Lasers (EC-QCL): an application field for MOEMS based scanning gratings", in "MOEMS and Miniaturized Systems XIII", (2014), volume 8977, pages 897708–11
  - [151] P. Zorabedian, "Tunable External-Cavity Semiconductor Lasers", in F. Duarte, editor, "Tunable Lasers Handbook", Academic Press, San Diego, Optics and Photonics, pages 349 – 442 (1995)

- [152] R. Maulini, "Broadly tunable mid-infrared quantum cascade lasers for spectroscopic applications", Ph.D. thesis, Université de Neuchâtel (2006)
- [153] I. Vurgaftman, C. L. Canedy, C. S. Kim, M. Kim, W. W. Bewley, J. R. Lindle, J. Abell, J. R. Meyer, "Mid-infrared interband cascade lasers operating at ambient temperatures", *New J. Phys.* 11 (2009), 125015
- [154] J. M. Wolf, A. Bismuto, M. Beck, J. Faist, "Distributed-feedback quantum cascade laser emitting at  $3.2\ \mu\text{m}$ ", *Optics Express* 22 (2014), 2111
- [155] J. P. Commin, D. G. Revin, S. Y. Zhang, A. B. Krysa, K. Kennedy, J. W. Cockburn, "High peak power  $\lambda \sim 3.3$  and  $3.5\ \mu\text{m}$  InGaAs/AlAs(Sb) quantum cascade lasers operating up to 400 K", *Appl. Phys. Lett.* 97 (2010), 031108
- [156] C. Vandewalle, "Band lineups and deformation potentials in the model-solid theory", *Phys. Rev. B* 39 (1989), 1871–1883
- [157] I. Vurgaftman, J. R. Meyer, L. R. Ram-Mohan, "Band parameters for III-V compound semiconductors and their alloys", *J. Appl. Phys.* 89 (2001), 5815–5875
- [158] M. P. Semtsiv, M. Wienold, S. Dressler, W. T. Masselink, "Short-wavelength ( $\lambda \approx 3.3\ \mu\text{m}$ ) InP-based strain-compensated quantum-cascade laser", *Appl. Phys. Lett.* 89 (2006), 211124
- [159] M. P. Semtsiv, M. Wienold, S. Dressler, W. T. Masselink, "Short-wavelength ( $\lambda \approx 3.05\ \mu\text{m}$ ) InP-based strain-compensated quantum-cascade laser", *Appl. Phys. Lett.* 90 (2007), 051111
- [160] A. Bismuto, R. Terazzi, B. Hinkov, M. Beck, J. Faist, "Fully automatized quantum cascade laser design by genetic optimization", *Appl. Phys. Lett.* 101 (2012), 021103–4
- [161] A. Bismuto, R. Terazzi, M. Beck, J. Faist, "Influence of the growth temperature on the performances of strain-balanced quantum cascade lasers", *Appl. Phys. Lett.* 98 (2011), 091105–3
- [162] A. Bismuto, S. Riedi, B. Hinkov, M. Beck, J. Faist, "Sb-free quantum cascade lasers in the  $3 - 4\ \mu\text{m}$  spectral range", *Semicond. Sci. Technol.* 27 (2012), 045013
- [163] G. Wysocki, R. Lewicki, R. F. Curl, F. K. Tittel, L. Diehl, F. Capasso, M. Troccoli, G. Hofler, D. Bour, S. Corzine, R. Maulini, M. Giovannini, J. Faist, "Widely tunable mode-hop free external cavity quantum cascade lasers for high resolution spectroscopy and chemical sensing", *Appl. Phys.* B 92 (2008), 305–311
- [164] T. Kruczek, K. A. Fedorova, G. S. Sokolovskii, R. Teissier, A. N. Baranov, E. U. Rafailov, "InAs/AlSb widely tunable external cavity quantum cascade laser around  $3.2\ \mu\text{m}$ ", *Appl. Phys. Lett.* 102 (2013), 011124–3
- [165] B. M. Oliver, "Sparkling spots and random diffraction", *Proceedings of the IEEE* 51 (1963), 220–221

- 
- [166] L. Allen, D. G. C. Jones, "An analysis of the granularity of scattered optical maser light", *Physics Letters* 7 (1963), 321–323
  - [167] K. Böhm, P. Marten, K. Petermann, E. Weidel, R. Ulrich, "Low-drift fibre gyro using a superluminescent diode", *Electronics Letters* 17 (1981), 352–353
  - [168] A. Kueng, P. A. Robert, "Measuring integrated optical circuits using a low-coherence light source", *Opt. Eng* 34 (1995), 2049–2054
  - [169] J. G. Fujimoto, C. Pitris, S. A. Boppart, M. E. Brezinski, "Optical Coherence Tomography: An Emerging Technology for Biomedical Imaging and Optical Biopsy", *Neoplasia* 2 (2000), 9–25
  - [170] A. B. Seddon, "Mid-infrared (IR) A hot topic: The potential for using mid-IR light for non-invasive early detection of skin cancer in vivo", *Phys. Status Solidi B* 250 (2013), 1020–1027
  - [171] R. Su, M. Kirillin, E. W. Chang, E. Sergeeva, S. H. Yun, L. Mattsson, "Perspectives of mid-infrared optical coherence tomography for inspection and micrometrology of industrial ceramics", *Opt. Express, OE* 22 (2014), 15804–15819
  - [172] E. A. Zibik, W. H. Ng, D. G. Revin, L. R. Wilson, J. W. Cockburn, K. M. Groom, M. Hopkinson, "Broadband 6  $\mu\text{m}$  – 8  $\mu\text{m}$  superluminescent quantum cascade light-emitting diodes", *Appl. Phys. Lett.* 88 (2006), 121109
  - [173] N. L. Aung, Z. Yu, Y. Yu, P. Q. Liu, X. Wang, J.-Y. Fan, M. Troccoli, C. F. Gmachl, "High peak power (10 mW) quantum cascade superluminescent emitter", *Appl. Phys. Lett.* 105 (2014), 221111
  - [174] M. C. Zheng, N. L. Aung, A. Basak, P. Q. Liu, X. Wang, J.-Y. Fan, M. Troccoli, C. F. Gmachl, "High power spiral cavity quantum cascade superluminescent emitter", *Opt. Express* 23 (2015), 2713
  - [175] B. W. Hakki, T. L. Paoli, "CW degradation at 300 K of GaAs double heterostructure junction lasers. II. Electronic gain", *J. Appl. Phys.* 44 (1973), 4113–4119
  - [176] D. Hofstetter, J. Faist, "Measurement of semiconductor laser gain and dispersion curves utilizing Fourier transforms of the emission spectra", *IEEE Photon. Technol. Lett.* 11 (1999), 1372 –1374
  - [177] R. Terazzi, J. Faist, "A density matrix model of transport and radiation in quantum cascade lasers", *New J. Phys.* 12 (2010), 033045
  - [178] R. Terazzi, "Transport in quantum cascade lasers", Dissertation, ETH Zürich, Zürich, Switzerland (2012), diss. ETH No. 20036
  - [179] Y. Bidaux, R. Terazzi, A. Bismuto, T. Gresch, S. Blaser, A. Müller, J. Faist, "Measurements and simulations of the optical gain and anti-reflection coating modal reflectivity in quantum cascade lasers with multiple active region stacks", *J. Appl. Phys.* 118 (2015), 093101
  - [180] S. Riedi, F. Cappelli, S. Blaser, P.-Y. Baroni, A. Müller, J. Faist, "Broadband superluminescence, 5.9  $\mu\text{m}$  to 7.2  $\mu\text{m}$ , of a quantum cascade gain device", *Optics Express* 23 (2015), 7184

- [181] A. R. Johnson, Y. Okawachi, M. R. E. Lamont, J. S. Levy, M. Lipson, A. L. Gaeta, "Microresonator-based comb generation without an external laser source", *Optics Express* 22 (2014), 1394
- [182] Y. Okawachi, K. Saha, J. S. Levy, Y. H. Wen, M. Lipson, A. L. Gaeta, "Octave-spanning frequency comb generation in a silicon nitride chip", *Opt. Lett.* 36 (2011), 3398–3400
- [183] M. A. Foster, J. S. Levy, O. Kuzucu, K. Saha, M. Lipson, A. L. Gaeta, "Silicon-based monolithic optical frequency comb source", *Optics Express* 19 (2011), 14233–14239